Polymer-Particle Nanocomposites: Size and Dispersion Effects

Joseph Moll

Submitted in partial fulfillment of

the requirements for the degree of

Doctor of Philosophy

in the Graduate School of Arts and Sciences

COLUMBIA UNIVERSITY

2012

ABSTRACT

Polymer-Particle Nanocomposites: Size and Dispersion Effects

Joseph Moll

Polymer-particle nanocomposites are used in industrial processes to enhance a broad range of material properties (e.g. mechanical, optical, electrical and gas permeability properties). This dissertation will focus on explanation and quantification of mechanical property improvements upon the addition of nanoparticles to polymeric materials. Nanoparticles, as enhancers of mechanical properties, are ubiquitous in synthetic and natural materials (e.g. automobile tires, packaging, bone), however, to date, there is no thorough understanding of the mechanism of their action. In this dissertation, silica (SiO_2) nanoparticles, both bare and grafted with polystyrene (PS), are studied in polymeric matrices. Several variables of interest are considered, including particle dispersion state, particle size, length and density of grafted polymer chains, and volume fraction of SiO_2.

Polymer grafted nanoparticles behave akin to block copolymers, and this is critically leveraged to systematically vary nanoparticle dispersion and examine its role on the mechanical reinforcement in polymer based nanocomposites in the melt state. Rheology unequivocally shows that reinforcement is maximized by the formation of a transient, but long-lived, percolating polymer-particle network with the particles serving as the network junctions. The effects of dispersion and weight fraction of filler on nanocomposite mechanical properties are also studied in a bare particle system. Due to the interest in directional properties for many different materials, different means of inducing directional ordering of particle structures are also studied. Using a combination of electron microscopy and x-ray scattering, it is shown that shearing anisotropic NP assemblies (sheets or strings) causes them to orient, one in front of the other, into macroscopic two-dimensional structures along the flow direction. In contrast, no such flow-induced ordering occurs for well dispersed NPs or spherical NP aggregates! This work also

addresses the interfacial, rigid polymer layer, or 'bound layer' which has long been of interest in polymer nanocomposites and polymer thin films. The divergent properties of the 'bound layer' as compared to the bulk material can have very important effects on properties, including mechanical properties. This is especially true in polymer nanocomposites, where at high weight fractions, 'bound layer' polymer can easily make up 20% or more of total material! Here we quantify this layer of bound polymer as a function of particle size, polymer molecular weight and other variables, primarily using thermogravimetric analysis but also dynamic light scattering and differential scanning calorimetry. We find that as nanoparticles become smaller, the 'bound layer' systematically decreases in thickness. This result is quite relevant to explanations of many polymer nanocomposite properties that depend on size, including mechanical and barrier properties.

Many additional important and new results are reported herein. These include the importance of dispersion state in the resulting mechanical properties of polymer-particle nanocomposites, where a systematic study showed an optimal dispersion state of a connected particle network. An additional and unexpected finding in this system was the critical dependence of composite properties on grafted chain length of particles. As the grafted chain length is increased, the strain which leads to yielding in a steady shear experiment is increased in a linear relationship. At very high rates, this yielding process completely switches mechanisms, from yielding of the particle network to yielding of the entangled polymer network! A surprising correlation between the amount of bound polymer in solution and in the bulk was also found and is interpreted herein. Self-assembly was further explored in a range of different systems and it was found that grafted particles and there mimics have vast potential in the creation of a wide array of particle superstructures.

In concert, these experiments provide a comprehensive picture of mechanical reinforcement in polymer-particle nanocomposites. Not only is the dispersion state of the particles

crucial, but the presence of grafted chains is also so for proper reinforcement. Here many routes to ideal dispersion are detailed and the important role of grafted chains is also resolved.

Table of Contents

1. Introduction 1

1.1 Experimental Techniques 2

1.1.1 Rheology 2

1.1.2 Transmission Electron Microscopy 9

1.1.3 Thermogravimetric Analysis 10

1.1.4 Differential Scanning Calorimetry 10

1.1.5 X-ray Photon Correlation Spectroscopy 11

1.2 Background and Rheology of Linear Polymers 13

1.3 Synthesis of Grafted Particles 15

1.4 Self-Assembly of PS Grafted Particles in PS Matrix 15

1.5 Dispersion Effects on Nanocomposite Properties 18

1.6 Polymer Bound Layer 19

2. Grafted Particles: Mechanical Behavior as a Function of Dispersion 21

2.1 Sample Preparation 21

2.2 Linear Rheology 22

2.2.1 Small Amplitude Oscillatory Shear 22

2.2.2 The Nanoparticle Network 26

2.2.3 Stress Relaxation 28

2.2.4 Long Time Response 30

2.3 Non-linear Rheology 34

2.3.1 Start-up of Steady Shear 36

2.3.2 A Maximum in the Morphology Diagram 38

2.3.3 Graft Length and Overshoot Strain 39

3. Alignment of Grafted Particle Structures in Response to Flow 42

3.1 The Peclet Number and Zeta 44

3.2 Experiment Design 45

3.2.1 Composite Preparation and Transition Electron Microscopy 45

3.2.2 Rheology 47

3.2.3 Image Analysis 48

3.3 Flow Response for 'Connected' Sheets 48

3.4 Flow Response for 'Isolated Aggregates' 53

3.5 Dispersion Effects on Degree of Aggregation with Shear 56

3.6 Large Amplitude Oscillatory Shear as a Route to Alignment 58

3.7 Extensional Rheology 59

3.7.1 Alignment 60

3.7.2 Strain Hardening 61

3.8 Conclusions 63

4. Entanglement of Grafts 65

4.1 The Cone-Partitioned-Plate Setup and High Shear Rates 66

4.2 High Shear Rate Experiments 68

4.3 Stress Relaxation after Steady Shear 74

5. The Polymer Bound Layer in Bare Particles 78

5.1 Bound Polymer Thickness in Attractive Polymer Particle Systems: Differential Scanning Calorimetry 78

5.2 Various Silica Particle Sizes in Poly (2-vinyl pyridine) 81

5.3 Thermogravimetric Analysis Experiment Design 82

5.4 Nanocomposite Characterization 87

5.4.1 Nanoparticle Dispersion 87

5.4.2 Nanoparticle Size 90

5.5 Bound Layer Dependence on Particle Loading 91

5.6 Bound Layer Dependence on Annealing 92

5.7 Bound Layer Dependence on Particle Size 93

5.8 Bound Layer Dependence on Molecular Weight 95

5.9 Conclusions 96

6. Rheology and X-ray Photon Correlation Spectroscopy on Bare Particle Systems: Dispersion and Weight Fraction 97

6.1 Rheology and X-ray Photon Correlation Spectroscopy at Different Weight Fractions 97

6.2 Effect of Solvent Choice on Miscibility of P2VP and Silica 102

6.3 Mechanical Properties as a Function of Dispersion for Bare Particle System 106

7. Other Avenues to Varying Particle Dispersion State 110

7.1 Self-Assembly of Grafted Particles in Poly (2-vinyl Pyridine) 110

7.2 Grafted Particle Mimics Using Block Copolymers 116

8. Conclusions 121

8.1 Dispersion Effects 121

8.2 Structure Alignment 122

8.3 Polymer Bound Layer 122

8.4 Grafted Particles vs. Bare Particles 123

8.5 Future Work 124

Bibliography 126

List of Figures

1.1 Monomeric subunits of PS and P2VP 13

1.2 TEMs of bare and grafted SiO_2 in PS. 14

1.3 PS grafted particles in PS: "morphology diagram". 16

2.1 PS grafted particles in PS : SAOS 23

2.2 Electron micrographs for Figure 2.1. 25

2.3 PS grafted particles in PS: nanoparticle network. 26

2.4 PS grafted particles in PS : stress relaxation. 29

2.5 PS grafted particles in PS : long time response. 31

2.6 Steady shear strain independent of rate. 35

2.7 PS grafted particles in PS : start-up of steady shear data. 36

2.8 Mechanical reinforcement 'morphology diagram'. 38

2.9 Overshoot strain vs. graft length. 39

3.1 Steady shear dispersion evolution for a 'connected sheet' dispersion state. 47

3.2 Tomographical data of the sample with a connected nanocomposite structure from Figure 3.1. 48

3.3 Ultra-small angle x-ray scattering on the 'connected' nanocomposite structure. 48

3.4 Radially averaged autocorrelation function on the 'connected' nancomposite structure. 51

3.5 Steady shear dispersion evolution fo an 'aggregate' dispersion state. 52

3.6 Radially averaged autocorrelation function on the 'aggregate' nanocomposite structure. 53

3.7 Shear aggregation as a function of initial dispersion state. 54

3.8 TEMs before and after steady shear. 55

3.9 Alignment in steady shear vs. LAOS. 57

3.10 Preparation procedure for microtomy of extensional samples 58

3.11 Electron micrographs of extensional samples. 58

3.12 Quiescent and strained geometry of quenched extensional samples..... 59

3.13 Extensional viscosity at different dispersion states and loadings..... 62

4.1 High shear rate viscosity for 129kg/mol homopolymer. 67

4.2 High shear rate viscosity for 'aggregate' dispersion state..... 68

4.3 High shear rate viscosity for 'connected' dispersion state..... 68

4.4 High shear rate viscosity for 'string' dispersion state..... 70

4.5 Reinforcement metric and strain of overshoot at different shear rates..... 71

4.6 Stress relaxation after steady shear..... 72

4.7 Storage modulus recovery after steady shear..... 73

4.8 Normalized stress recovery after steady shear for different dispersion states..... 74

4.9 High graft density dispersion state has less 'structure' than homopolymer at high rates..... 75

5.1 DSC as a function of 14nm SiO_2 particle loading for P2VP, PMMA, and PEMA.. 79

5.2 Bound layer thickness from DSC. 78

5.3 TEMs confirming excellent dispersion for four different sizes of particles at 30 weight %. 80

5.4 Particle size distribution. 83

5.5 Pellet formation. 83

5.6 Effect of washing on bound layer. 83

5.7 Different weight fractions and particle sizes all show good dispersion. 88

5.8 Dispersion quality comparison of computer and micrograph generated images. 89

5.9 Bound layer thickness as a function of annealing time. 90

5.10 Bound layer thickness as a function of particle diameter. 93

5.11 Dispersion state achieved for 4nm and 10 nm diameter particles. 94

5.12 Bound layer dependence on P2VP molecular weight in the bulk..... 93

5.13 Bound layer dependence on P2VP molecular weight in solution..... 94

6.1 Diffusion coefficient as a function of time annealing. 96

6.2 G’ and G'' for 14nm diameter bare SiO_2 particles in 97 kg/mol P2VP. 97

6.3 Normalized low frequency slope of G' for bare particles 98

6.4 TEM micrographs at high weight percent..... 101

6.5 Dispersion quality as a function of pyridine concentration..... 101

6.6 Dispersion state as a function of preparation solvent..... 103

6.7 G' and G'' at low frequency and different dispersion states: 5% by weight..... 105

6.8 G' and G'' at low frequency and different dispersion states: 10% by weight..... 106

7.1 Extremes of dispersion state..... 109

7.2 Three of the representative morphologies in a PS grafted particle in P2VP system..... 112

7.3 A ‘morphology diagram’ for PS grafted particles in P2VP modeled after Figure 1.3..... 113

7.4 A new ‘morphology diagram’ for PS grafted particles in P2VP..... 114

7.5 Self assembled structures using different matrix MW and concentrations of PMMA-b-PS. 119

7.6 Dispersion states for SiO_2 particles with PMMA-b-PS chains in different solvents..... 118

Acknowledgements

During my time at Columbia I have had the opportunity to work with many wonderful people, and their insight, advice, mentoring, help and kindness have made my work both possible and enjoyable. I would like to take this opportunity to thank each of them. First, I would like to offer my utmost gratitude to the professors who have principally advised me along the way. Professor Sanat Kumar provided most of the ideas for this work and certainly is owed a large debt of gratitude. At the beginning of my Ph.D. he knew little about me. He took a big chance by bringing me into his lab after I had been orphaned by the chemistry department. This was not unusual for him; he is always eager to invest in people; I think he understands when those investments are successful the returns are large. Sanat judges his students on merit. Discrimination is not practiced in his lab. I firmly believe in the benefit I have received by working in a lab with people of such diverse backgrounds. Sanat is a great scientist and his encyclopedic knowledge of the scientific literature has pushed my work forward, past many obstacles. I very much appreciate the freedom he has afforded me in the pursuit of the answers to all our questions about polymer-particle nanocomposites.

I had the additional benefit of being co-advised at Columbia by a wonderful professor in the chemistry department, Nicholas Turro. Professor Turro had minimal involvement in the day to day aspects of my research, but from the beginning of my Ph.D. career, he was directly involved in my personal and professional development. Having Professor Turro as my co-adviser helped me to step back and look at everything I was learning and needed to learn during my Ph.D. that was beyond the realm of silica-polymer nanocomposites. His mentoring helped me to understand the bigger picture, to understand what science is supposed to be, how it can be done well, and what purpose it serves in

civilization. In addition, Professor Turro has great personal qualities, including kindness, loyalty, and of course professionalism.

Through Sanat I was introduced to many other outstanding professors who have helped me along the way. In particular, I was able to spend a summer in the lab of Ralph Colby at Pennsylvania State University as well as two months in the lab of Dimitris Vlassoupolous at FORTH in Crete. Dr. Colby immediately took an unexplainable interest in me and has always considered me as one of his students. As such, it is safe to say that I have three advisers. His mentoring has proven invaluable, and he is often the first person I go to for advice and help in research. His peerless dedication to science is a joy to watch. Dr. Colby sees answers that other people gloss over. A discussion with him about science is often filled with long pauses as he fully and carefully considers every problem (or maybe just wonders how I could possibly say some of the foolish things I've sometimes said). These pauses never make the conversation boring, because the best part is observing him while the motor in his brain is vigorously turning. He always pushes his students, and I've accomplished much more in my Ph.D. than I would have without him.

Dimitris is absolutely wonderful. I will fondly remember the numerous fine Cretan restaurants he took me to, all of which were amazing and at which he took special and unnecessary care to accommodate me as a vegetarian. To give an idea of the magnitude of his hospitality, I will mention that I only stayed in Crete for a total of two months over two visits. During that short time, I went to eat with Dimitris and his lab well over a dozen times. For Dimitris, being a good host is a primary responsibility and even though I was just a student, I was treated with a level of hospitality to be expected by someone much more established and with far more connections. Dimitris lent me his son's bicycle and didn't say a word when I barely used it. He gave me useful advice about where to visit in Athens and he afforded me a quite generous allowance for living expenses in the middle of a major

Greek economic crisis, when many lab budgets were being slashed. However, I do not wish to give the impression that my time in Crete was spent only eating and sightseeing. On the contrary, during the three weeks of my first visit to Crete I learned more than at any other period in my graduate career, and during both visits, my productivity was at its peak. In Dimitris lab, continuous learning is valued highly and Dimitris hospitality was a huge motivator behind my hard work while there.

I additionally would like to thank the two remaining members of my committee, Professor Laura Kaufman and Professor Luis Campos. Professor Campos very generously offered to serve on my committee despite a summer filled with travel. Professor Kaufman, in particular, has been a part of my graduate education from the beginning. She has always been willing to discuss research with me and has always been at hand with helpful advice.

I would also like to thank Professor Norton and Gonzalez in the chemistry department, for helping me find my way to Sanat's lab at the beginning, when everything looked a bit hopeless. I would like to further thank Professor Gonzalez, and all of the other professors who taught my classes in graduate school, especially Professor Reichman, who is one of the best teachers I have ever had.

I would additionally like to thank Professor Brian Benicewicz and his lab, especially Atri Rungta, for providing the particles without which much of this work wouldn't have been possible. Also, these acknowledgements would never be complete without thanking Clare Castro and William Karney, my undergraduate research advisers. They helped me apply to graduate school and without their help and excellent mentorship I would not have even gotten into Columbia, let alone every graduate school I applied to.

I of course would like to thank all the post-docs and senior graduate students who helped me along toward the completion of my Ph.D. In particular, Damien Maillard was always available to help me with new experimental techniques, and would put aside his own tasks in order to explain things to

me. He was just about the best post-doc a young graduate student could hope to have as a mentor. I would also like to thank Pinar Akcora for her guidance at the beginning and for the use in this text of some of her electron micrographs, Sumit Sharma for his friendship and mentoring, and Erica Saltzman who always gave valuable input during my group meeting presentations, and valuable advice outside of them. She is a highly valued friend. I have only known Nicolas Jouault briefly, but he is incredibly helpful and because of my experience with him and Damien, if I ever get a lab of my own, it will include at least one French post-doc. Yuping has been very fun to get to know over the last few years and was always willing to help with any problems I had. Also, from the Kumar lab, I would like to thank Manish Agarwal, Dong Meng, Behnaz Bozorgui Jagannathan Thimmarajampet Kalathi, Jesse and Josh. In the Turro lab, Jeffrey Lancaster is an immense repository of formatting and software knowledge and was not afraid to share it. Ellane Park helped me fund the Turro cake fund, and Judy Chen helped me buy my first pair of running shoes (cake baking and running being incredibly relaxing diversions while working toward the Ph.D. Dustin Janes, from Professor Durning's lab, was also amazing. It was not uncommon that we would spend over an hour discussing research, and even though he usually knew much more than me about the topics at hand, he never made me feel ignorant or stupid. I would also like to thank Shane Harton, who although our times in the Kumar lab only overlapped briefly, was always helpful through e-mail. Furthermore his research was a major foundation for many of my papers. I would like to thank Suresh Narayanan and Alec Sandy, who helped me immeasurably with X-ray Photon Correlation Spectroscopy. Frank Snijkers and Rossana Pasquino treated me very well in Crete, and taught me a lot about rheology and I'm glad I was able to return the favor by teaching them new words in English (e.g crux).

I had the pleasure to mentor many undergraduate students and high school students while I was at Columbia including Stacy Ramcharan, Claire Kearney, Rebecca Frauzem, Adiba Ahmad, Huili Zhu, Lisa Mack, Ed Hu, Jifeng Wei, Julianna Lee, Nisha Hollingsworth, and Kendra Windsor. I would especially like

to thank Stacy Ramcharan, who is the hardest working student I have ever seen and will have lots of success at graduate school, and Claire Kearney, who was a joy to work with. It's also been immense fun to mentor Dan Zhao during our short period of overlap in the Kumar lab. I can already tell he will really excel in his Ph.D.

Amongst my more direct peers in graduate school, there are also many to thank, including Jesse and Flora from the Kumar lab. Mithun Radhakrishna, Michael Clark, and Shyno Mathew provided the camaraderie necessary for me to enjoy my days in the office. Michael Clark was full of tons of useful advice at group meetings and probably paid more attention to my presentations than everyone else combined. Mithun was a lot of fun. Halfway through my Ph.D., he moved across our basement office in the engineering building to sit next to me by the window. This increased the number of distractions in the day ten-fold, but it was awesome to have someone nearby to laugh with, and I enjoyed our weekend bicycling excursions in Central Park immensely. Thanks to Mithun, I am also a converted dosa enthusiast. Shyno was always up for a very early morning (i.e. 6:15 am) tennis game or an evening Broadway show. I was very disappointed when she switched labs but am glad our friendship has continued.

Ben Dach and Xin Xin Zhu served roles of camaraderie in the Turro lab, and were always good friends. At FORTH in Crete, Helen Lentzikis proved a wonderful peer, and she was also the one who showed me how to use the extensional rheology set-up. I will never forget the 5-hour, raki fueled hike we took through the mountainous Cretan countryside. At Penn State University, my lab buddies were Greg Tudryn, U Hyeok Choi and Adam Larson. Greg was a wealth of information, Choi and I had a lot of fun playing tennis, and Adam taught me most of what I know about State College. Shushan Gong was the closest thing to a teammate I've had in Graduate school; it's been a lot of fun working with her. She is a great colleague and friend!

Others who have been incredibly helpful include Mary Ko who helped me out of many tight reimbursement binds, Theresa Collaizo who was always answered any question I had, and Sandy Turro who truly worked to ensure the Turro group was a cohesive social community, and always made me feel welcome, even though my office was far away from the rest of the group.

I would also like to thank my graduate student friends at Columbia, who include many of the people already mentioned above as well as three people in particular from the chemistry department. Richard Darst, who's weekly dinner making sessions with me were therapeutic, to say the least. At the beginning of graduate school, I was a bit nervous about making friends with Richard but it was one of the best decisions I made. Lizz Thrall, who studied the electron microscope with me and who's weightlifting mentorship will allow me to leave graduate school a much stronger Ph.D. than the student who came in. And also, Manasi Bhate, who even though she was incredibly busy, always took the time to nurture our friendship and whose facial expressions are truly priceless (not to mention distracting when we went to plays and musicals together). Additionally, with my help, Manasi chose a really great fiancé.

I would like to thank the many friends outside of graduate school I made in New York City, and especially Schuyler Hooke, who taught me most of what I know about how to have fun in New York, and who introduced me to theater, Carcassone, and gay culture. Other friends I must mention are Giselle Schuetz and Carl Smith, who were always willing participants at my dinner parties.

I'd like to thank all my undergraduate friends who stuck with me through all the years apart and whose support was invaluable, including Taruna Chhabra, Shoaib Mahmood, Zach Maxey, Valerie Salonga, Melissa Poulsen, Tran Phan, and Mavis Ngo. They're all great and it was wonderful to have so many out-of-town visitors to keep me company. I'd also like to thank my undergraduate research peers, Gertrude, Miles, and Ryan P. Pemberton, our summers at USF were awesome. I feel truly blessed to

have made the lifelong friends I did at the University of San Francisco, and the values I learned there will stick with me for life.

I'd also like to thank my cat, Frankie; Even though I didn't find him until toward the end of my graduate career, his unconditional adoration of me has been quite a confidence booster. My boyfriend, Kabir Duggal has provided a lot of support through the writing of this thesis, and I would like to thank him as well. He made sure I always had a healthy meal break, he was more than generous with his shoulder rubs, and he has sent me many e-mails of encouragement throughout these days. I wish I had met him earlier in my academic career.

Finally, I would like to thank my family. As anybody who has traveled the path knows, graduate school is filled with highs and lows, and I would never have made it through some of the worst times if not for the frequent conversations with my kin, and especially my mother, to help me through the despair. I really love you mom! I also want to thank my father for instilling in me the love of learning that inspired me to pursue a Ph.D. in the first place. I want to thank my sister Michelina and her family (Dave, Gabe, Nate and Joel) for always opening their door with welcome arms as my only relatives on the East coast. I thank Tom and Abby for hosting me in Portland during visits home (and Tom for making the vest that I wore to defend), and Phil for the awesome bicycles he gave me and for being a great big brother, and Dave and Tim and Matt and Mary. I especially appreciate Mary for agreeing to go with me on my Ph.D. victory vacation in Hawaii and Matt for coming out to see my defense. I'd like to thank Tim for riding out the hurricane with me and Dave for coming to stay with me at my only Thanksgiving in New York, which was a lot of fun. I would also like to thank Jack for the love he gave me while he was here; I still miss him very much. I love all of you.

Dedicated to my mother,

Dorothy Nicotera Moll

1. Introduction

It has been more than 8 decades since nanoparticles (NPs) have been added to synthetic materials to improve properties as variant as mechanical properties[1-4], electrical properties[2, 5], and gas permeability[6, 7]. A wide range of nanoparticles (clay, silica, gold, C_{60}, carbon nanotubes) are now added into materials ranging from car tires to gas filtration systems. Nanoparticles are typically of size order less than 100nm and can have a wide variety of different shapes (rods, discs, spheres). Nanoparticle size [8, 9] and dispersion [10, 11] are critical in determining their effect on material properties. The various effects of particle size are most commonly understood by invoking the increased surface area to volume ratio of the particles as compared to micron sized particles or larger. Particle dispersion state affects the percolation threshold of nanocomposites, among other things. Yet, to date, much about the mechanism of property improvements for nanocomposites and especially their improvements in mechanical properties is not well understood.

This work focuses on the mechanical properties of linear polymers filled with inorganic nanoparticles. As much as possible, the results are generalized to all filled polymer systems. Specifically, spherical particles ranging from ~100 down to less than 10 nm have been studied. Both bare silica (SiO_2), which has a surface chemistry dominated by silanol groups, and SiO_2 grafted with polystyrene (PS) have been used. These systems have been studied with two linear polymers of widely varying molecular weight. Namely, poly (2-vinyl)pyridine (P2VP) and PS. These polymers have both been widely studied, and especially in the case of PS, the behavior of linear PS (i.e. in the absence of branching) is well understood and documented. P2VP was chosen as a polymer analogous to PS, but with a pyridine group replacing the phenyl group along the polymer backbone (thus allowing for a favorable interaction between the polymer and SiO_2 surface). Both PS and P2VP are semi-flexible polymers with low entanglement molecular weights (M_e).

In order to study the full phase space of these systems, a wide range of variables are used, including particle size, volume fraction of SiO_2, particle dispersion state, free polymer (or matrix polymer) molecular weight and in the case of grafted particles, graft density and grafted chain length.

1.1 Experimental Techniques

A wide range of techniques from material chemistry were employed in order to study the various experimental systems in this thesis. Rheological measurements play an extremely important part in the narrative of the mechanical properties of polymer nanocomposites. Transmission electron microscopy (TEM) was used to characterize almost all of the samples studied and to quantify both the particle size and the particle dispersion state in the composites; Small Angle X-ray Scattering (SAXS) and Ultra-Small Angle X-ray Scattering (USAXS) were done by collaborators at Argonne National Laboratory to compliment the TEM measurements. Thermogravimetric analysis (TGA), differential scanning calorimetry (DSC), and dynamic light scattering (DLS) were used to quantify the bound polymer in these nanocomposite systems. X-ray Photon Correlation Spectroscopy (XPCS) was used to study the diffusion of nanoparticles in polymer matrices and provide a view of microscopic mechanical reinforcement, as opposed to the macroscopic mechanical reinforcement that rheology probes. Many other experimental techniques were also employed, and these are outlined in the appropriate chapters, as needed.

1.1.1 Rheology

Rheology is an important tool for understanding the viscoelastic properties of complex materials. Here it is used as the primary measurement of nanocomposite mechanical properties. A wide range of rheological experiments have been employed, including small amplitude oscillatory shear (SAOS), stress relaxation, creep, start-up of steady shear, large amplitude oscillatory shear (LAOS) and extensional rheological experiments at a constant extension rate. All of these measurements work in tandem toward understanding a material's rheological response. SAOS can give information about the

build-up of structure with time and help determine whether a material is a viscoelastic liquid or solid. It can also give the yield strain of a material. Stress relaxation and Creep experiments are important for measuring the long time material response, and can also tell whether the material is a liquid, solid, or critical gel. Start-up of steady shear gives the yield stress and extensional rheology can tell the degree of strain hardening, among other things.

There are two variables of primary importance in rheology. The first is the strain, represented as the Greek letter γ, a dimensionless measure of the deformation of a material, the exact definition of which is dependent on the initial material geometry (i.e. shape). The second is the stress, represented as the Greek letter σ, which has units of pressure and is a measure of a materials response to an imposed strain. Stress is the deforming force divided by the area over which it is applied.

SAOS is the rheological experiment "that has been most widely used to determine the linear viscoelastic properties of polymeric liquids."[12] In SAOS, a sinusoidal strain (γ) or deformation is imposed on a sample. The resulting stress (σ) is also sinusoidal, and has the same frequency as the strain, but is phase shifted. The phase shift of the stress (along with the ratio $\sigma_{max}/ \gamma_{max}$) are only dependent on the frequency of the oscillations in γ, not on γ_{max}, as long as γ_{max} is not too large (this experimental regime is termed as the linear regime and this is where the word small comes from in SAOS). The phase shift of the frequency is given as the Greek letter δ and is very important. For a purely elastic sample, the relationship between stress and strain can be seen in Equation 1.1:

Equation 1.1

$$\sigma = G\gamma$$

This equation is Hooke's law for an elastic solid, where G is the elastic modulus, a material constant analogous to the spring constant. Thus the stress is proportional to strain. Alternatively, for a Newtonian liquid, the relationship between stress and strain is shown in Equation 1.2 :

Equation 1.2

$$\sigma = \eta \dot{\gamma}$$

This equation is Newton's Law of Viscosity, where η is a material constant, the viscosity, and $\dot{\gamma}$ is the shear rate, or rate of deformation. Thus the stress is proportional to the time derivative of the strain. Consider that an elastic solid has a well-defined shape and if a strain is imposed to displace it from that shape, a restoring force attempts to return it. Alternatively, a Newtonian liquid takes the shape of its container, thus its resistance to deformation is only manifested while the deformation takes place. In this sense, a SAOS experiment is particularly clever. The strain has a sinusoidal oscillation, and the component of the stress which oscillates in phase with the strain can be related to the elastic nature of a viscoelastic material. There is also a component of the stress which oscillates 90 degrees out of phase with the strain (according to a cosine function). This stress oscillates in phase with the rate of strain, and can be related to the viscous nature of a viscoelastic material. This can be seen in the definition of the storage and loss moduli (G' and G'' respectively) in Equation 1.3 and Equation 1.4:

Equation 1.3

$$G' = \frac{\sigma_{\max}}{\gamma_{\max}} \cos\delta$$

Equation 1.4

$$G'' = \frac{\sigma_{\max}}{\gamma_{\max}} \sin\delta$$

Storage and loss in this context refers to energy. These two variables are of primary interest in SAOS. G' is a measure of the solid like response of a material (stored energy) and G'' is a measure of the liquid like response (dissipated energy).

Step strain (also called Stress Relaxation) and Creep give very similar information to SAOS, but are less often used (although more conceptually simple). In stress relaxation, an instantaneous strain is imposed on a fully relaxed material at time t=0. The stress is monitored as a function of time. Here again, it is useful to consider the response of an elastic solid and a Newtonian liquid. In the former case, there is no mechanism by which the stress can relax. Thus whatever initial stress exists, which will be proportional to the total deformation or strain, will persist for eternity. In the latter case the stress will be quite high as the strain is taking place, but will fall to zero as soon as it stops. In a viscoelastic material, the stress will neither fall to zero instantaneously nor persist indefinitely, but gradually relax to zero (e.g. in polymer melts), or to some constant value (e.g. in elastomers). The speed with which this happens depends on the time constants of the stress relaxing mechanisms within the material. At very short times, there is often no mechanism by which decay can occur, and the stress will appear constant (as in an elastic solid). This 'glassy' behavior is typically much too short for rheological measurements. If there is a large amount of time in between relaxation processes, the stress will remain constant, or plateau. Often, in entangled polymer melts, the entanglements will relax last, and there will be a gap of some amount of time between their relaxation and that of proceeding relaxation processes. The resulting plateau can be used to calculate the density of entanglements[13]. In analogy with Hooke's Law above, the ratio of time dependent stress and applied strain give the time-dependent stress relaxation modulus, G(t), defined in Equation 1.5:

Equation 1.5

$$G(t) = \frac{\sigma(t)}{\gamma_0}$$

The stress relaxation modulus is a material property that is independent of strain, as long as the measurement is in the linear regime (i.e. the strain is low).

A creep experiment is the conjugate of a step strain experiment. Instead of imposing a constant strain and monitoring the stress, a constant stress is imposed and the strain is monitored. This experiment is particularly useful for long time measurements, because the torque (and thus the sensitivity of the measurement) does not decay with time. One caveat is that the measurement may start in the linear regime, but end outside of it as the strain begins to climb (in stress relaxation, if the beginning of the experiment is in the linear regime the sample will remain in the linear regime throughout, because the strain is constant and the stress only decreases with elapsed time).

In a creep experiment, an elastic solid will deform a certain amount in response to the constant stress, but no further. A Newtonian liquid will continue deforming indefinitely, assuming the stress is high enough to begin deformation. Here again, a new variable is defined which relates stress to strain for this experiment and this is called the shear creep compliance, represented as J(t) Equation 1.6:

Equation 1.6

$$J(t) = \frac{\gamma(t)}{\sigma}$$

If the creep experiment is in the linear regime, the behavior of J(t) will be independent of the stress.

All of the above experiments are primarily used to measure the linear viscoelastic response of materials. These linear measurements are useful because they do not perturb the material in a permanent way (i.e. there is no hysteresis). However, it is sometimes necessary to quite drastically perturb a system to fully understand it, and thus non-linear measurements perform an important role. In start-up of steady shear, a constant rate of strain is imposed and the stress is measured as a function of time. Here a viscosity is also used, which while it is not the same as the viscosity for a Newtonian liquid (since it is not a material constant), is defined in Equation 1.7 in a similar way:

Equation 1.7

$$\eta = \frac{\sigma}{\gamma}$$

Other variables of interest are the first and second normal stress differences (N_1 and N_2).

LAOS is the non-linear analogue of SAOS. Here, a sinusoidal oscillating strain is still imposed, the amplitude of which is outside the linear regime. Thus it is no longer the case that the stress also oscillates as a sine function(higher harmonics will be present)[12]. In this work, LAOS is not utilized to study rheological variables, which can be quite complicated, but rather to use flow fields to align materials. Alignment with LAOS has been achieved on many other systems, including di-block copolymers[14, 15], colloidal crystals[16], and other nanocomposite systems[17-19], to name a few.

The final rheological experiment used herein is extensional rheology. According to Dealy and Wissbrun[12], "the simplest definition of an extensional flow is that it is a deformation that involves stretching along streamlines." Extensional flow is different than typical shear flow, because the geometry changes with time. Extensional flow is of a great deal of importance to industry. In this work, extensional flow is used primarily to look for particle alignment, but also to quantify strain hardening. Strain hardening is an important industrial property by which the "stress increases more rapidly than would be expected by the linear theory" upon deformation[12]. In polymeric materials, including polymer nanocomposites, it arises from polymer entanglements and it is an important area of study[20, 21]. Homopolymers only show strain hardening at elongation rates above the inverse Rouse stretch time($1/\tau_R$). At these high rates the individual chains are stretched, which leads to hardening. The Rouse stretch time is roughly defined in Equation 1.8:

Equation 1.8

$$\tau_R = \frac{\tau_D}{3Z}$$

with τ_R the Rouse stretch time, τ_D the reptation time (or terminal relaxation time) and Z the number of entanglements. This formula assumes pure reputation and no contour length fluctuations and is, as such, only a rough approximation. In light of this discussion, strain hardening at low elongation rates can be an important signature of reinforcement of polymer melts by nanoparticles (monodisperse, linear polymer melts show no strain hardening in extension at low rates).

As a final tool to understanding the rheological experiments in this text, it is important to mention a bit about rheological geometry. Ideally, geometry will not have a large effect on measurements. While this is often the case for linear shear, it is not always so. Most of the shear measurements taken herein were performed in a parallel plate geometry (a disc shaped geometry), the major disadvantage of which is that the strain is non-uniform, and specifically increases as the radial distance from the disc center is increased. Also, in a parallel plate geometry, the bulk of the material is relatively close to the edge of the sample, and thus edge fracture is a major concern. In addition, wall slip may occur while shearing melts. In order to remove any doubt that the phenomena discussed herein were an artifact of the geometry, in some instances an 8mm cone and plate geometry with a cone angle of 0.1 radians was used. This geometry (with an accompanying addition to the ARES oven design) was custom built [22], based on a system first proposed by Meissner[23-26]. In this geometry, the cone is used as a replacement to the lower plate and was 25 mm in diameter. On top, an 8mm plate is attached to a ring partition and the ring partition is not connected to the force-rebalance transducer. Therefore, the diameter of the measured sample was only a fraction of the diameter of the sheared sample, because in this set-up, the edge of the sample is no longer measured. Thus the results of any edge

fracture are significantly delayed (until such time as the edge defects expand inward to the measured portion of the sample).

This altered geometry allows more accurate characterization of strain in the sample. Furthermore, because any so-called 'edge effects' will be immediately visible in the rheological data (e.g. in the form of an uneven stress plateau), these too can be ruled out. In all experiments within this work, the geometry is defined at the outset.

1.1.2 Transmission Electron Microscopy

TEM was used to characterize the dispersion state of the nanoparticles in their polymer matrices. Although TEM has some limitations (e.g. small sample size, requirement for contrast between components of a material) for homogenously dispersed nanocomposites, it can quickly confirm the dispersion state and provide a visual image much easier to understand than a scattering plot.

TEM uses electrons to probe a material and one of the primary limitations is that unlike many other particles (e.g. x-rays and particularly neutrons), electrons are not very penetrating. Thus, any sample has to be very thin to be studied. It is typically not possible to get a quality image at thicknesses much greater than 100nm (with a thickness of 200nm the upper limit of the best TEMs).

The electrons in a TEM beam produce an image by interacting with the electrons in a sample. Since the electron density is proportional to the material density, materials with a higher density appear darker in a TEM image (less electrons make it through to produce the image). TEM is ideally suited for SiO_2-polymer nanocomposites, because the density of the SiO_2 particles (1.9 g/cm^3) [27] is about twice as large of the density of the polymers used ~1g/cm^3 for both PS and poly(2-vinyl pyridine) (P2VP). Note that the SiO_2 particle density is slightly less than the density of bulk SiO_2 (2.2 g/cm^3).

1.1.3 Thermogravimetric Analysis

TGA is a conceptually simple experiment that was used primarily for calculations of the total amount of bound polymer. In a TGA experiment, a sample is placed in a crucible, and the temperature is ramped as the mass is simultaneously measured. Assuming a sample with multiple component parts, which burn at different, well defined temperatures, the drop in mass at a given temperature can be used to quantify the mass percentage of the various constituents in the sample.

Most of the TGA measurements that will be talked about in this work were taken on centrifugation pellets. These were made after polymer nanocomposites were re-dissolved in a solution. Such a solution will have three constituent elements, SiO_2 particles, free polymer chains, and polymer bound to the SiO_2 surface. Upon the choice of an appropriate number of revolutions per minute, the particles will travel to the bottom of the tube (the pellet) the free polymer will stay in solution (the supernatant), and any bound polymer will enter the pellet as a traveling companion to the particle. It is this pellet that can then be burned in a TGA to quantify the total amount of bound polymer.

1.1.4 Differential Scanning Calorimetry

Differential scanning calorimetry (DSC) is similar to TGA in design; a sample is heated over the course of time. Here the sample heat capacity is measured. In polymers DSC is widely used. The glass transition temperature of polymers can be measured by observing an abrupt shift in the behavior of the heat capacity. It is also quite useful for separating out constituent elements of mixtures, if the response of the pure materials are known. It is in such a context in which DSC is primarily used in this work as well as to show the shift in the glass transition temperature (T_g) of polymer nanocomposites relative to the T_g of pure polymers.

1.1.5 X-ray Photon Correlation Spectroscopy

Scattering can be broadly defined as the deviation of radiation from its path as it passes through a medium and is caused by non-uniformities in a sample. Many different particles will scatter, including neutrons, electrons, and photons. A scattering event can be elastic (i.e. outgoing radiation has the same energy as incident radiation), inelastic (i.e. outgoing radiation has a different energy than incident radiation), coherent (i.e. radiation has a constant phase relationship, e.g. either always in phase or always out of phase) or incoherent (radiation does not have a constant phase relationship). In X-ray Photon Correlation Spectroscopy (XPCS), a beam of x-rays is passed through a sample of interest and the changes in the scattering pattern over time are used to give information about the motion of the constituents in the sample.

The x-rays in an XPCS experiment are a form of synchrotron radiation (radiation from charged particles traveling at relativistic speeds). X-rays interact with the electromagnetic field of the electrons in matter (and thus interact more strongly with heavier elements). X-rays can be, for example, adsorbed, scattered elastically, scattered inelastically, etc., and each scattering event will have a different probability. Adsorbed x-rays can produce secondary electrons, which are primarily responsible for radiation damage in samples. To minimize the potential for this damage, x-ray experiments are typically short.

In order to better understand x-rays, it is useful to compare them to other common scatterers, such as neutrons and electrons. While electrons provide information about small areas of samples, and are not amenable to statistical averaging, and neutrons provide statistical averages rather than real space pictures, x-rays can be used to do both (although in XPCS, a statistical average of the sample is created). In contrast to neutrons, but similar to electrons, x-rays interact with the electrons in a sample. X-rays are very penetrating (which is why they can be used to image human bones), but are not as

penetrating as neutrons (neutrons interact with the nucleus of samples, a rather small target, and thus tend to pass long distances through materials). Electrons are not very penetrating at all, which is why samples used for experiments with electrons must be very thin (discussed in Section 1.1.2).

In the US, the three largest shared user facilities which provide synchrotron radiation are: The National Scattering and Light Source at Brookhaven National Laboratories, the Advanced Photon Source at Argonne National Laboratories, and the Advanced Light Source at Lawrence-Berkeley National Laboratories. All x-ray experiments presented in this work were performed at Argonne National Laboratories.

XPCS is the x-ray analogue of dynamic light scattering (with an additional benefit that x-rays, unlike visible light, can travel through opaque materials) and compliments rheological experiments. Rheology informs one about the macroscopic mechanical behavior of a system. XPCS focuses on the microscopic mechanical behavior. In XPCS, a beam of x-rays is passed through a sample and the changes in the scattering function over time are used to calculate the diffusion constant as well as signatures of gel-like behavior.

As discussed, the scattering image created by the beam of x-rays is dependent on non-uniformities in the sample, and in the case of polymer nanocomposites, these are primarily caused by the presence of the particles. The exact position of the particles is important, and if their positions do not change, the scattering pattern will also remain the same. However, at elevated temperatures, the particles are mobile, thus the scattering image changes with time. These changes can be used to understand the motions of the particles, or the microscopic dynamics (by creating an autocorrelation function of the scattered intensity with time). As a matter of simplification, XPCS is usually used to look at samples with a constant average structure, but a changing local structure.

In an XPCS experiment, the autocorrelation function of the intensity with time is fit to a stretched exponential as seen in Equation 1.9:

Equation 1.9

$$f(Q,t) = A + Be^{(\frac{-t}{\tau})^{\beta}}$$

where A is the baseline (equal to 1), B is the contrast (which depends on the coherence of the beam), τ is the relaxation time, which can be related to the diffusion coefficient, and β Is the stretching exponent, which can be related to the gel-like behavior of the material.

1.2 Background and Rheology of Linear Polymers

PS is ubiquitous in modern research and life. Its discovery dates back almost two centuries. The entanglement molar mass of PS is 17,000 g/mol at 140° C and the glass transition temperature (T_g) is 373K[13]. P2VP is analogous to PS but the monomeric unit has a nitrogen at the 2 position of the phenyl ring. Figure 1.1 shows a monomeric subunit of both PS and P2VP. The T_g of P2VP is the same as PS, 373 K[28] and both PS and P2VP have a density of ~1.1g/cm^3[29]. For comparison, the density of bulk SiO_2 is 2.2 g/cm^3 and the density of the SiO_2 particles is 1.9 g/cm^3 and the smaller density of the nanoparticles has been explained by voids primarily near the particle surface[27]. The entanglement molar mass of P2VP is slightly higher than that of PS, at 27,000 g/mol[30]. P2VP and PS are immiscible and the miscibility of P2VP partially depends on its ability to form hydrogen bonds with the component of interest[31]. The surfaces of SiO_2 particles are covered with hydroxyl groups, and the resulting hydrogen bonds between P2VP and SiO_2 favor miscibility. This is the opposite of PS: bare SiO_2 particles form large agglomerates when mixed with PS[32]. TEMs showing bare SiO_2 in both PS and P2VP are displayed in Figure 1.2. Despite these

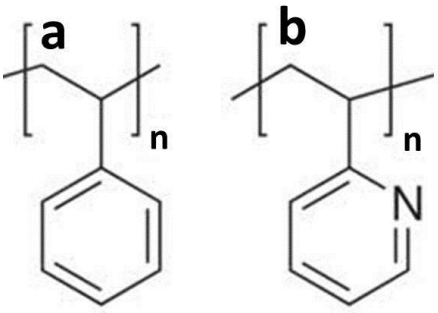

Figure 1.1 *Monomeric subunits of PS(a) and P2VP(b)*

differences, many physical properties of the two polymers are very similar, allowing for concentration on the primary variable of interest in much of this work, the hydrophobic/hydrophilic nature of these polymers, and thus their miscibility with SiO_2 (P2VP is much more hydrophilic). For all TGA experiments, P2VP is the polymer used and under nitrogen it burns at ~400° C[31].

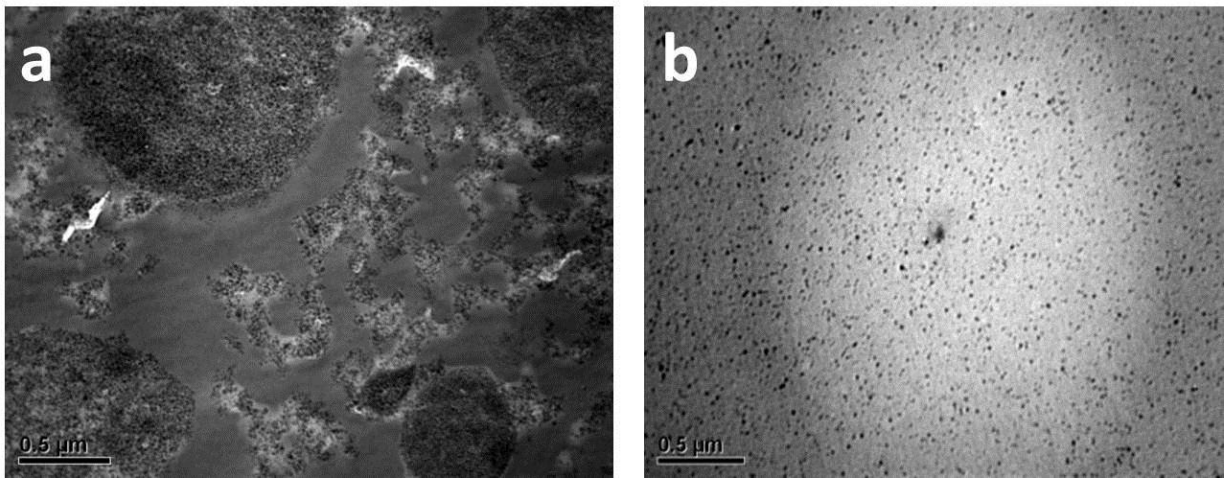

Figure 1.2 *In general, bare silica particles are immiscible with PS (a) and miscible with P2VP (b).*

In order to provide some background for the large amount of rheology of polymer nanocomposites discussed herein, it is important to fully understand the rheology of linear (i.e. non-branching) polymers. All of the samples used in this work were made with very monodisperse polymers (typically with P.D.I. of ~1.2 or less) and so we focus on the rheology of monodisperse PS and P2VP. As many of the rheological experiments discussed in Section 1.1 give essentially the same information about a material, here the discussion will be confined to SAOS, the most broadly used rheological experiment. In general, linear polymers behave very differently rheologically depending on whether they are above or below their entanglement molecular weight. For instance, in an unentangled melt, G'' is always greater than G'[12]. If we consider the storage modulus of a linear polymer, in every case it will have a very high frequency glassy modulus plateau, which typically is not measureable. If there are entanglements, there will be a secondary, entanglement plateau. This occurs at lower frequencies,

corresponding to the long lived nature of the entanglements (small values in the frequency domain correspond to large values in the time domain). G'' will pass through a minimum in the region of the elastic plateau in G' "reflecting the fact that little dissipation occurs in the region of rubbery behavior"[12]. (At these frequencies, the material is acting more like a solid). Beyond this entanglement regime, these polymers enter into terminal relaxation. If one plots G' and G'' vs. frequency on a log-log plot, the relationship in this regime is linear (indicative of power law behavior), with slopes of 2 and 1 respectively.

1.3 Synthesis of Grafted Particles

Grafted particles are created through one of two broadly defined synthetic routes. The first is a grafting-to synthesis, where the polymer is first synthesized separately from the particle and then attached via a chemical reaction. The second is a grafting-from synthesis, where the polymer is grown out from the particle surface. In this work, PS grafted SiO_2 nanoparticles were synthesized according to a RAFT (reversible addition-fragmentation chain transfer) synthesis [33, 34]. RAFT is a versatile, straightforward "controlled radical polymerization technique" [24]. Recently, RAFT has been increasing in prominence [35, 36]. As it is compatible with a grafting-from synthesis, RAFT has the advantage of being able to achieve much higher graft densities.

RAFT is a free radical polymerization and follows the series of conventional steps for such reactions. First is radical generation, then chain transfer agent activation, which is followed by a propagation step (core-RAFT equilibrium) and finally termination[37].

1.4 Self-Assembly of PS Grafted Particles in PS Matrix

Self-assembly is the "autonomous organization of components into patterns or structures without human intervention" and is relevant in many scientific processes[38]. Its importance in polymer and particle systems has long been a topic of interest. For example, the well-studied phase diagram for di-

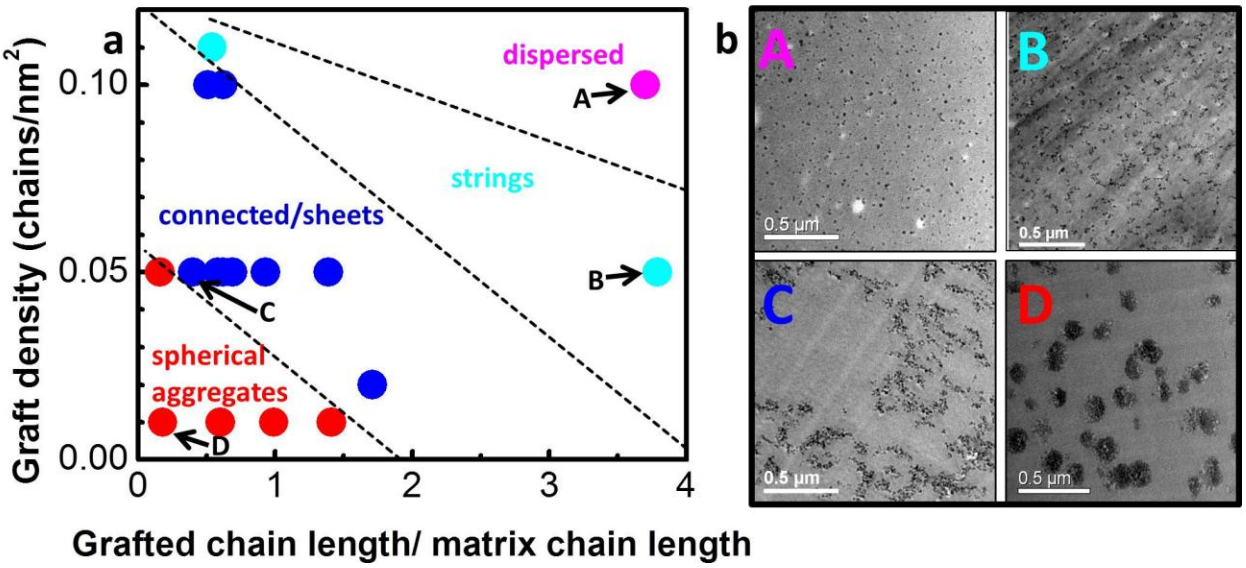

Figure 1.3 *Experimental "morphology diagram" of polymer tethered particles mixed with matrix polymers(a). The red region represents spherical aggregates, the blue region represents sheets and interconnected structures, the cyan region represents short strings and the magenta region represents dispersed particles. The lines that separate different regions are merely guides to the eye. b.) Transmission electron microscopy micrographs corresponding to the delineated samples in 1.3a which constitute member nanocomposites from each of the four broadly defined regions in the morphology diagram.*

block copolymers shows a broad range of potential morphologies, primarily depending on the relative lengths and the miscibility of the blocks[39] and this has a great deal of practical relevance, including in the next generation of 'ultra-high density storage media'[40]. Self-assembly is a defining property of amphiphyllic materials, including di-block copolymers, Janus particles[41], peptides[42], and many other systems.

Previous work in the Kumar lab has well established that SiO_2 nanoparticles uniformly grafted with PS chains will self-assemble, forming a wide array of nanoparticle structures[43]. In this work the particles are 14nm in diameter, which has been confirmed many times experimentally [10, 44, 45]. They are grafted with PS chains using a RAFT polymerization method [33, 34, 46, 47] which is discussed in more detail in Section 1.3. These particles are isotropic, and whereas with anisotropic particles it is not difficult to explain the formation of complex, anisotropic structures (as the anisotropy of the particle encodes the resulting geometry)[48], here the formation of anisotropic structures is less intuitive.

Essentially, the SiO_2 core and the PS grafts and matrix are immiscible, because the SiO_2 is hydrophilic and the PS is hydrophobic[32]. However, because the grafted polymers are chemically bound to the SiO_2 particles, dispersion of the SiO_2 is possible, and the extent to which this takes place depends on grafted chain length and graft density, thus allowing for a wide range of dispersion states, from spherical aggregates to well dispersed particles. Thus these composites self-assemble into an array of anisotropic structures by virtue of the inherent dislike between the SiO_2 and the PS[33, 34, 43, 46, 47]. This assembly process is akin to that seen in block copolymers, and, as with block copolymers, one can plot this assembly in a phase diagram. In this phase diagram, the critical variables are the graft density and the ratio of the grafted chain length to the matrix chain length. This is done in Figure 1.3. The x-axis in this figure, the ratio of graft to matrix chain length, α, is a measure of the solvent quality experienced by the grafted polymer brush in the matrix polymer. In the large α limit, the brushes are in good solvent and the only unfavorable interaction is between the particle cores and the polymers. In the opposite limit, where the α value tends to 0, the matrix chains dewet the brush autophobically [49]. There is now a dislike between the polymers and the core, but also a dislike between the brush and matrix chains. Many previous experiments have conclusively demonstrated that this crossover from wet to non-wet brush behavior occurs when α ~1 [50-54]. The y-axis is the density of graft chains on the nanoparticle surface, σ. In the limit of large α and σ the nanoparticles are well dispersed due to steric stabilization. In the opposite limit of small α and σ the nanoparticles macroscopically phase separate from the matrix. Decreasing the values of α and σ progressively leads to strings, sheets and interconnected structures of nanoparticles. At a fixed brush-matrix wettability, as the graft density increases, the particle dispersion changes from spherical aggregates to connected structures to a well dispersed state. It is important to note that the dashed lines separating different regions in the phase diagram are not abrupt transitions and are merely meant as guides to the eye. Chevigny et al.[11] went to slightly higher graft densities and other authors have gone to much higher graft densities [32, 55] with results consistent with the

phase diagram presented, however Sunday et al. [56] found that some adjustments need to be made when both σ and α are very large. As these high values are not studied here, this caveat is ignored for the purposes of this dissertation. Due to the large variability in dispersion states achieved, a system of PS grafted particles in a PS matrix can be used to better fundamentally understand the effect of dispersion on various nanoparticle properties.

1.5 Dispersion Effects on Nanocomposite Properties

The addition of filler has been found to dramatically enhance the mechanical properties of polymeric materials[1]. The mechanism of reinforcement, however, remains in debate, but there is broad agreement that particle dispersion state plays a critical role. There are three scenarios that have been proposed. At one extreme, mechanical reinforcement is suggested to be due to the agglomeration of particles; when these agglomerates percolate through the system there is a direct pathway for the propagation of stress and hence mechanical reinforcement[1-4]. In contrast to this "particle-only" scenario, others involve both the particles and polymer chains. Long et al.[57] used the fact that chain immobilization occurs around nanoparticles[58]—they suggested that mechanical reinforcement is found when particles with a "bound" glassy layer percolate[59-62]. A final scenario considered by Arunguren[63] and Goritz[64], and elaborated upon by Wang[65] and Sternstein[66], is that the particles form a network, with the polymer chains forming "bridges" between particles. Crucial to resolving this argument is the ability to control the nanofiller dispersion state. Particularly relevant is that the Kumar group previously showed that SiO_2 nanoparticles uniformly grafted with PS behaved akin to block copolymers because of the dislike between the SiO_2 core and the PS corona (discussed in Section 1.4). These grafted particles thus self-assembled into a variety of anisotropic structures when they were placed in a PS matrix (Figure 1.3)[43].

1.6 Polymer Bound Layer

When polymeric materials are exposed to a surface, they form an adsorbed layer[67]. This layer of polymer can have drastically different properties than the bulk material. For instance, glass transition temperature (T_g) changes have long been studied in these confined systems, beginning with the benchmark works of McKenna[68, 69] and Keddie et al.[70, 71] These changes are related to the surface-polymer interaction: attractive interactions increase T_g while repulsive interactions decrease T_g[28, 72, 73]. However, significant T_g changes in bound polymer are controversial. Indeed, in previous work by the Kumar group the T_g of poly(2-vinyl) pyridine (P2VP) loaded with SiO_2 particles (14nm in diameter) was investigated and minimal changes in T_g(less than 10 K) were observed[74]. Many other groups have also seen negligible changes in T_g for both thin film and polymer nanocomposite systems[75-77].

Nanoparticle size has a dramatic effect on the resulting particle-polymer nanocomposite properties[8], and the improvement in properties when going from micron to nano sized filler particles can be large. This phenomenon is most easily understood by invoking the substantial increase in the surface area to volume ratio as the nanoparticle size is reduced. For spherical NPs, this ratio goes as the inverse of the radius. This is especially important for material properties that depend on inter-particle interactions (such as mechanical and electrical properties), as all interactions should be mediated through the surface. Furthermore, at constant volume fraction as nanoparticle size decreases the inter-particle separation will also decrease, increasing interactions between particles.

In all of this, the polymer-particle interaction is paramount, and this is related to the size ratio of nanoparticles to the polymer chains. For instance, nanoparticle miscibility is determined by this ratio; it has been found that nanoparticles of smaller size than the polymer radius of gyration (R_g) are miscible and if the reverse is true immiscibility results[78]. Relative size can often be more important than the

enthalpic interaction between nanoparticles and polymer. Another area of considerable study is the confinement effect the presence of the nanoparticles has on the polymer.

There have been many attempts to quantify the total amount of polymer on the nanoparticle surface, but no systematic study of particle size effects. The few attempts to quantify the magnitude of the bound layer of polymer on nanoparticles relative to a flat surface have produced results ranging from the finding of Brown et al. of a 'bound polymer' layer that has no dependence on particle size[9], to a complete absence of bound polymer[79]. In the first case, only repulsive interactions between the nanoparticles and the polymer were considered, limiting the applicability of the results; In the second case the error was of size order of the measurements[74]. Work in the Kumar group on highly attractive polymer particle pairs has definitively shown a reduction in the 'bound layer' for nanoparticles: whereas a flat surface has a 'bound layer' of order ~5nm, for 14nm diameter, this drops to only ~1nm [74, 80]. The attractive interactions in these systems were in contrast to the work of Brown et al.[9], potentially explaining the deviation in results. Indeed, Cohen-Addad and Ebengou[81] found that attractive interactions lead to a thicker bound layer that also adsorbs much more quickly. Other groups have also attempted to quantify the bound layer around particles. Sargsyan et al.[75] found a ~2.5nm bound layer for poly(methyl methacrylate) (PMMA) adsorbed to 15nm diameter SiO_2 particles. . In their work, the particle dispersion state was agglomerated, potentially clouding the results. Fragiadakis et al. found a 2-3nm bound layer for composites of 10nm diameter SiO_2 in both natural rubber[82] and poly(dimethyl siloxane)[83]. Finally, Ciprari et al. studied alumina and magnetite nanoparticles with diameters of 39 and 90nm respectively. Both PMMA and PS were used as the adsorbed polymer and they calculated bound layer thicknesses of ~5nm for the alumina nanoparticles and ~10nm for the larger magnetite nanoparticles, irrespective of polymer (both of which were found to have to have 'limited interaction' with both sets of particles). They postulated that a thicker bound layer could be due to weaker interactions between the nanoparticles and the polymer[84].

2. Grafted Particles: Mechanical Behavior as a Function of Dispersion

Dispersion of nanoparticles plays a critical role in many material properties, however proper control of dispersion is a long standing problem in polymer nanocomposites. Different techniques have been used to improve dispersion, including reducing the particle size to below the radius of gyration (R_g) to improve miscibility [78], functionalization of the nanoparticle surface[85], and sonication [86], among other techniques. In this chapter, PS grafted SiO_2 nanoparticles are used to control dispersion, as discussed in Section 1.4. The mechanical properties of the resulting composites are systematically tested using melt rheology (at temperatures 80K above the T_g of PS).

2.1 Sample Preparation

All grafted particles are prepared in the lab of Professor Brian Benicewicz at the University of South Carolina. PS chains are grown from the surfaces of spherical SiO_2 nanoparticles (diameter = 14 nm, Nissan Chemicals) using reversible addition-fragmentation chain transfer (RAFT) polymerization as discussed in Section 1.3 [33, 34, 46, 47]. The chain length of the grafts and the graft densities are varied systematically to vary the dispersion state (Section 1.4) and the samples used in the experiments in this chapter are indicated in tables in the individual sections in which the samples are discussed. The grafted particles are dissolved in solvent, either benzene or tetrahydrofuran (THF), and mixed with a monodisperse PS matrix dissolved in the same solvent. This solution is sonicated (2 s sonication, 1 s rest) for 3min, poured into a 60mm diameter Petri dish, dried overnight in a vacuum oven, and then annealed for 5 days at 10^{-4} Torr at 150 $^{\circ}$C. All the composites have 5 weight % of the SiO_2 core unless otherwise noted. The samples are analyzed by transmission electron microscopy (TEM), USAXS (not reported here), and rheology. TEM samples are microtomed (thickness ~60 nm) and transferred to a Formvar-coated copper TEM grid. Rheological samples are dried for 5 days at 80 $^{\circ}$C to remove any solvent and molded into cylindrical discs 1-2 mm in thickness and 8 mm in diameter. Samples for the start-up of

steady shear at various rates are carefully treated in precisely the same fashion for annealing, molding, and loading into the rheometer to facilitate comparison. All rheological measurements are made at 180 °C.

2.2 Linear Rheology

Linear rheology, including linear oscillatory shear, step strain, and creep, is fundamental to the understanding of mechanical properties. Here, SAOS is focused on, but linear creep and stress relaxation are also considered. The latter two were performed to probe the mechanical properties at long times. The results of all rheological experiments showed a strong dependence on the matrix polymer, but for linear experiments this dependence was especially pronounced. Therefore, in this section, most figures compare samples with matrices of the same molecular weight.

2.2.1 Small Amplitude Oscillatory Shear

In order to compare samples from throughout the morphology diagram in Figure 1.3, small amplitude oscillatory shear was performed on many composites, with a focus on comparisons between samples that were all prepared in the same matrix, as the matrix molecular weight has a large effect on rheological behavior. In Figure 2.1, seven composites are considered. At 5 % by weight of SiO_2 the particles do not significantly change the loss modulus (G'') from G'' of the homopolymer. The storage modulus (G'), in contrast, does have significant differences from G' of the homopolymer, all of which occur at low frequency. In Figure 2.1a and Figure 2.1b samples at three different graft densities are considered, as compared to the 129 kg/mole PS(orange data points). The relevant details of these samples are listed in Table 2.1. Here, two grafted chain lengths are compared: ~28 kg/mol in Figure 2.1a and ~75 kg/mol in Figure 2.1b. Thus when the graft density is increased, the dispersion in Figure 2.1a moves from spherical aggregates at low graft density up to an interconnected network structure at higher graft densities and in Figure 2.1b it moves from aggregates to an interconnected structure to

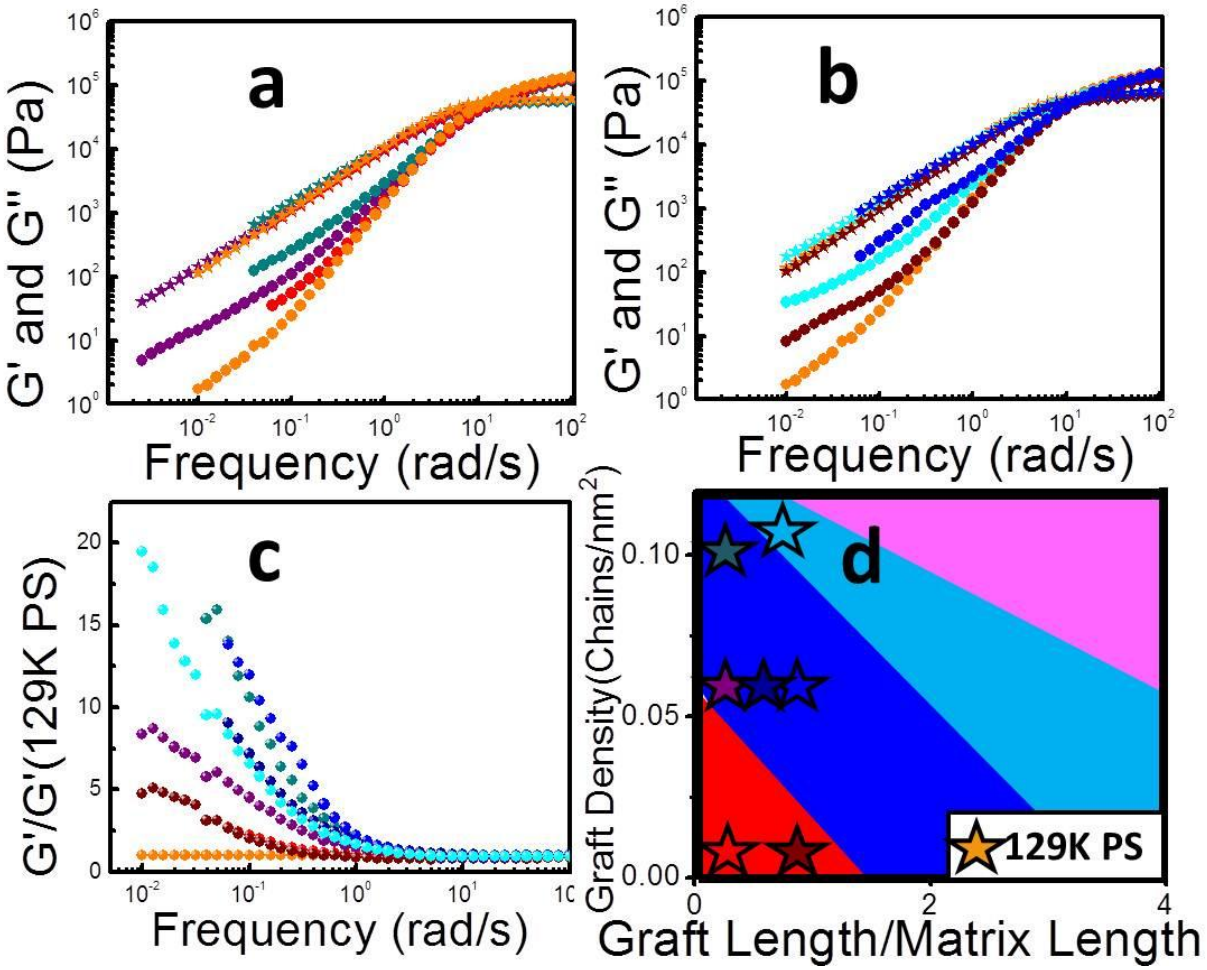

Figure 2.1 *Absolute and normalized storage moduli (circles) and loss moduli (stars) for various nanocomposite dispersion states. Graft length is held constant at ~28 kg/mol (a) and ~75 kg/mol (b) as the graft density is steadily increased, from 0.01 ch/nm^2 to ~0.1ch/nm^2. The normalized storage modulus for a range of samples (c) as well of the location of all samples in the morphology diagram are displayed. Three out of the four broadly defined regions in the morphology diagram are represented: Aggregates (red and dark red data points), connected/sheet structures (purple, royal blue, blue, and teal) and particle strings (cyan). The 129 kg/mol homopolymer data points are gold. The low frequency storage modulus is highest in the connected sheet region of the morphology diagram, indicating optimal mechanical properties in this morphological regime.*

strings. In both plots, having a particle dispersion state corresponding to an interconnected network structure maximizes the low frequency storage modulus. If a true nanoparticle network forms, this will also manifest itself in the storage modulus. In such a case, one would expect a low frequency plateau in G' (analogous to the entanglement plateau of a pure polymer discussed in Section 1.2). In all studied composites at 5 weight percent SiO_2 no such plateau was observed. On the other hand, even going to

the lowest frequency possible in the ARES rheometer (0.001 rad/s), in no composite was terminal relaxation reached. Therefore, one cannot rule out the possibility that a very low frequency plateau exists, corresponding to a true network of nanoparticles. In any case, the small amplitude oscillatory shear experiments presented here clearly show an improvement in material properties at dispersion states in the 'connected/sheet' region of the morphology diagram, and apparently this improvement is maximized at intermediate graft density. This can be seen in Figure 2.1c, where the normalized storage moduli for all 7 composites is plotted (i.e. the composite storage modulus divided by the matrix storage modulus). In Figure 2.1d the location of the samples in the morphology diagram from Figure 1.3 is displayed. The two aggregate samples (red) have a particularly low storage modulus compared to the other samples. These also have a large variance in dispersion from the other samples, as can be qualitatively seen in the TEMs of the seven samples listed in Table 2.1 (Figure 2.2). Of note is the sequestration of all of the samples on the left side of the diagram. This highlights a limitation of the small amplitude oscillatory shear experiments. In order to probe the full width of the morphology diagram, it is necessary to use matrices of different molecular weight (because of the limited range of the graft length of the polymer on the nanoparticles). However, a comparison of the storage and loss moduli for composites with different matrices is complicated by the fundamental contribution of the matrix polymer to the relaxation processes occurring in G' and G'' at a given frequency. Even the normalization of the storage moduli by their respective matrices does not facilitate comparison, because the entanglement plateau and terminal relaxation happen at different frequencies depending on the matrix. Thus in order to compare samples throughout the morphology diagram, it is necessary to devise a different, more suitable metric than that of normalized storage modulus, and this will be addressed in Section 2.3.2.

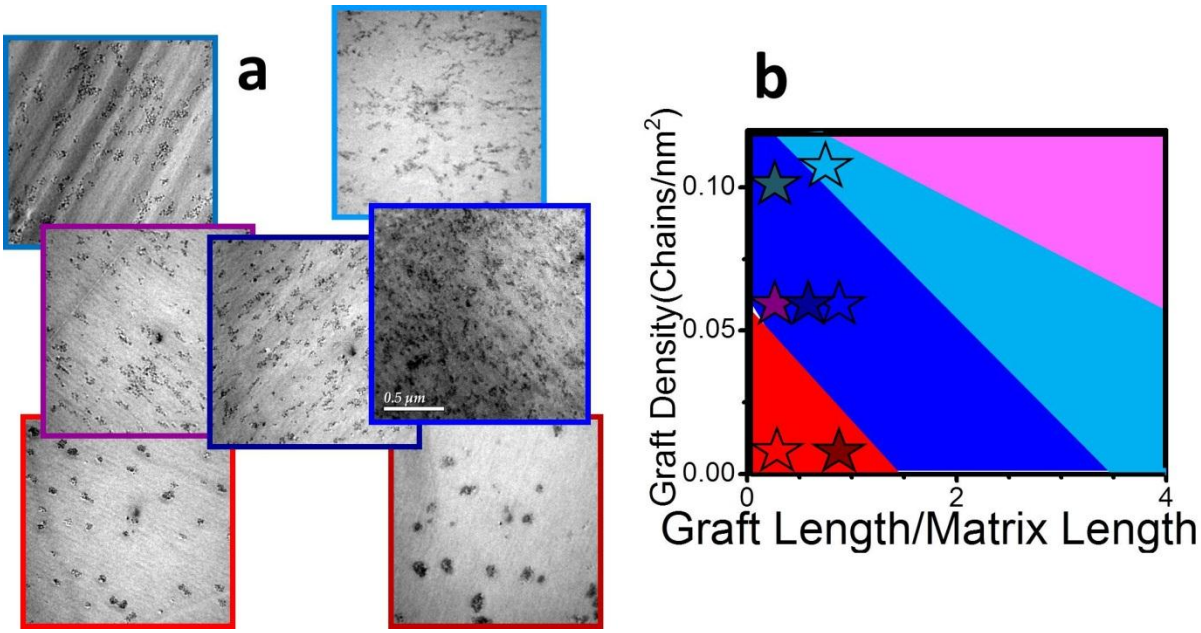

Figure 2.2 *TEMs of the seven samples studied (a) and there location in the morphology diagram (b) first presented in Figure 2.1.*

Table 2.1 *Brush and matrix number-average molecular weights (M_n), polydispersities (PDI), brush graft densities, matrix solvent quality, and morphologies for SAOS samples.*

Graft density (chains/nm^2)	Graft M_n (kg/mol)	Graft PDI	Matrix M_n (kg/mol)	Matrix PDI	Matrix Solvent Quality (α)	Morphology
0.01	30	1.3	129.2	1.03	0.23	aggregates
0.01	78	1.3	129.2	1.03	0.60	aggregates
0.05	32	1.07	129.2	1.03	0.25	connected
0.05	52	1.07	129.2	1.03	0.40	connected
0.05	75	1.06	129.2	1.03	0.58	connected
0.1	25	1.15	129.2	1.03	0.19	connected
0.11	70	1.1	129.2	1.03	0.54	strings

2.2.2 The Nanoparticle Network

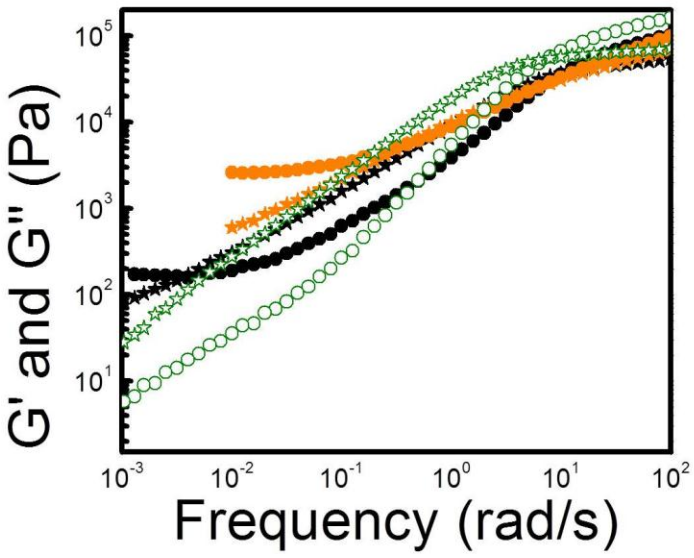

Figure 2.3 *180°C storage moduli(circles) and loss moduli (stars) at different loadings: 5% (open green), 8% (black), and 15% (gold) by weight. The graft molecular weights are 52, 114 and 150 kg/mol respectively. The matrix molecular weight is 129 kg/mol for the 5% and 8% particle loadings and 150 kg/mol for the 15% loading of silica.*

In order to more quantitatively represent the mechanical reinforcement as a function of dispersion state, an attempt is made to understand the existence of a nanoparticle network in the context of rubber elasticity theory. In Figure 2.3, composites with 5, 8, and 15 wt % of SiO_2 nanoparticles are considered, from the region of the morphology diagram (Figure 1.3) with the largest low frequency storage modulus, i.e., percolating particles at an intermediate graft density of 0.05 chains/nm^2. The relevant experimental details of these samples are listed in the figure caption. At the higher loadings, a plateau in the storage modulus is observed at experimentally accessible frequencies. If one extrapolates the low-frequency plateau in G' (the equilibrium modulus of the nanoparticle network G_{eq}) down to a modulus of zero by plotting $G_{eq}^{1/3}$ versus the weight percent of SiO_2, the onset of gelation is predicted to be ~3.2 percent by weight and the modulus expected for the 5 wt % sample is 8 Pa (near the border of our lowest measurements). Of course, with only two data points this extrapolation is far from quantitative. According to the phantom network model[87], the number density of elastically effective network strands ν in excess of the number density of elastically effective junction points μ is given by Equation 2.1:

Equation 2.1

$$\nu - \mu = \frac{G_{eq}}{k_B T}$$

We assume every particle acts as a network junction point, making $\mu = 5.2 \times 10^{16}$ particles/cm^3 for the 15 wt % and $\mu = 2.6 \times 10^{16}$ particles/cm^3 for the 8 wt %. Using the measured G_{eq} of 2610 and 172 Pa for the 15% and 8% composites, respectively, yields ν-μ = 4.17×10^{17} strands/cm^3 (9 graft-graft entanglements per particle) for the 15 wt % and 2.75×10^{16} strands/cm^3 (2 graft-graft entanglements per particle) for the 8 wt % nanocomposite. These data therefore support the picture that the mechanical reinforcement is driven primarily by the formation of a nanoparticle network, with the particles as the junction points and graft-graft entanglements as the elastically effective strands. In this context, it appears that a glassy adsorbed polymer layer is not necessary to explain the observed reinforcement in this system (recall such a layer was discussed in Section 1.6). Indeed, this mechanism for reinforcement is ruled out not only by the large distances between the particles, but potentially also by the high temperature, T_g + 80 K (although it is not clear to exactly which temperature the bound layer will persist). According to previous work in the Kumar group, well dispersed particles at 15 wt % SiO_2 display an elastic modulus plateau[10], suggesting reinforcement. In this well-dispersed system, the inter-particle distance is ∼44 nm. Previous experimental work has suggested that the SiO_2-PS system is characterized by a bound (presumably glassy) layer of thickness ∼1 nm, or perhaps slightly greater thickness, as was discussed in Section 1.6 [74]. Given the particle size of 14 nm and the large inter-particle spacing, a bridging of glassy layers cannot explain these findings.

Jouault et al.[88] studied bare SiO_2 particles in PS at very low percent SiO_2. They discovered evidence of reinforcement in the existence of high temperature G_0 plateaus. These authors also rule out an overlap of glassy layers and suggest that the PS matrix may be bridging particles, allowing interparticle interactions far below the volume fractions at which all of the nanoparticles contact each

other. While the differences in the two systems make it difficult to directly compare, it is not unreasonable to suppose that in cases such as these their adsorbed polymers are acting analogously to the chemically grafted polymers studied here.

Furthermore, it is important to emphasize that the tests presented herein were performed well above T_g and on a system of non-contacting nanoparticles, and thus other mechanisms of reinforcement may exist in different nanocomposite systems. Indeed, a very different system will be discussed in Chapters 5 and 6. However, this experimental system was chosen because of its relevance to industrial problems and specifically the optimal dispersion state of nanoparticles in automobile tires. By studying well above T_g and without cross-links, the nanoparticle network is isolated, and it is the mechanism of reinforcement in this network that is addressed. The ability to systematically vary the nanoparticle morphology allows the critical examination of the factors that have been proposed to underlie mechanical reinforcement in polymer nanocomposites far above T_g. The percolation of nanoparticles is necessary for stress propagation across the system—however, entanglement of graft chains on different particles allows this percolation at much lower particle loadings. Thus, these results unequivocally show that mechanical reinforcement in this system results from the formation of a network where the nanoparticles are the network junctions [64, 66, 89-91] connected by graft-graft entanglements as the elastically effective network strands.

2.2.3 Stress Relaxation

In order to validate the small amplitude oscillatory shear data and probe frequencies that are low enough to potentially show a clear effect of the nanoparticle network even at 5 percent by weight loading (i.e. a low frequency plateau in the storage modulus), stress relaxation was studied for the same seven composites discussed in Section 2.2.1, listed in Table 2.1 and displayed in Figure 2.2. In stress relaxation, as discussed in Section 1.1.1, a step strain is imposed on the sample and the relaxation of the stress is charted in time. A stress relaxation experiment occurs in the time domain, instead of the

frequency domain, and thus it is much easier to take the samples to long times (the equivalent of low frequencies). The ARES rheometer has a lower frequency limit of 0.001 rad/s, however there is no upper limit to time, and after only 1000s the equivalent timescales of the 0.001 rad/s SAOS measurement have already been probed (in SAOS, measuring out to these low frequencies would take almost 24 hours). In Figure 2.4 the stress relaxation data for all seven composites are considered (the corresponding location in the morphology diagram is indicated in the inset). Notably, the ordering of the composites is the same as can be seen in Figure 2.1c. Here, only the composite with the structure most centrally in the 'connected/sheet' region of the morphology diagram shows evidence of a low frequency plateau. The other samples do potentially show plateaus, but they are below the torque range of the rheometer and thus their validity is subject to question. In fact, this is a primary limitation of stress relaxation experiments: the data become unreliable when the torque falls too low. The torque can be increased by increasing the step strain, however, the strain must be linear (and hence small). Indeed even if a larger strain is chosen, a general rule of thumb on an ARES rheometer is that one should not trust the moduli once it drops four orders of magnitude below its initial value. Thus while all of the curves in Figure 2.4 are taken out to very long times, insufficient torque resulted in very noisy data at the longest

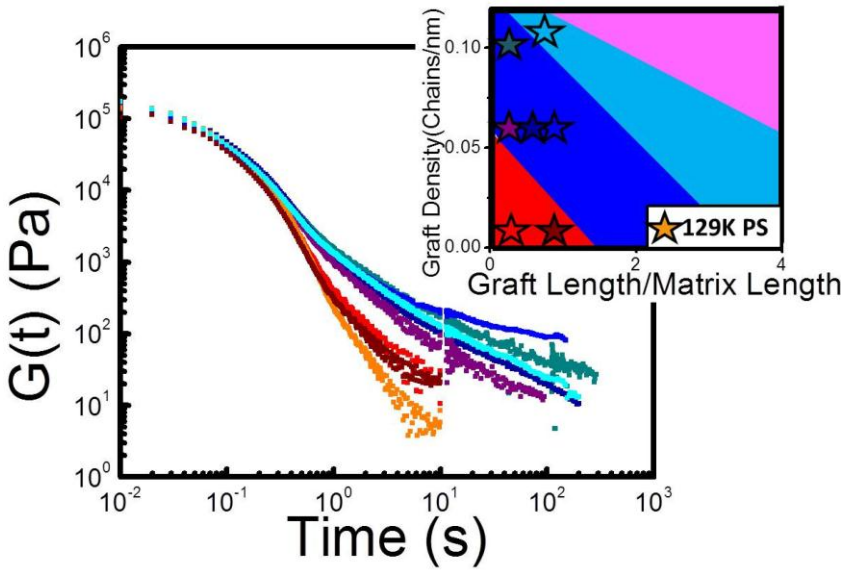

Figure 2.4 *Stress relaxation measurements for seven nanocomposites and a 129 kg/mol homopolymer. The relaxation modulus is plotted as a function of time, and persists out to the longest times for the blue samples, located in the connected/sheet region of the morphology diagram (shown in inset).*

measurement times. Creep experiments, which as opposed to stress relaxation apply a constant stress instead of a constant strain, are also ideally suited for long time measurements, and torque does not change as creep progresses. In Section 2.2.4 creep on these samples will be discussed, as well as stress relaxation experiments that were taken with an Anton Paar Physica rheometer, which has a wider torque range than the ARES.

2.2.4 Long Time Response

As stated previously, the particle network behavior (and specifically any particle plateau) manifests itself at very low frequencies or long times. The experiment of choice studying long time behavior is creep. In creep one can probe very long timescales and the decrease in torque that would be experienced in stress relaxation or small amplitude oscillatory shear is not a concern. This is because creep is a constant stress experiment, and thus the torque is also constant throughout the experiment. This is discussed in more detail in Section 1.1.1. All creep experiments were done on an Anton-Paar Physica rheometer, which is a stress controlled rheometer (as opposed to ARES, which is strain controlled). The Anton-Paar Physica has a feedback mechanism that allows it to also perform strain controlled experiments (e.g. stress relaxation and small amplitude oscillatory shear) and because of some difficulties that were encountered with Creep, several stress relaxation experiments were also done using this rheometer. The Physica has a lower torque resolution than the ARES, which facilitates stress relaxation at long times.

Several problems were experienced with creep, the primary problem being difficulty finding a linear stress regime. In this regime, the creep compliance (J(t)) should overlay at different values of stress. For many of the studied samples this overlay was not possible even as the stress approached the lower limit of the rheometer and thus these results are not shown.

In Figure 2.5 the long time behavior for four different samples plus that of the 129 kg/mol homopolymer are presented. Because of the problems with creep outlined above, the results in Figure 2.5 are from either creep (green) or stress relaxation experiments (red), and in both cases have been converted into SAOS data. The data conversions are then compared to

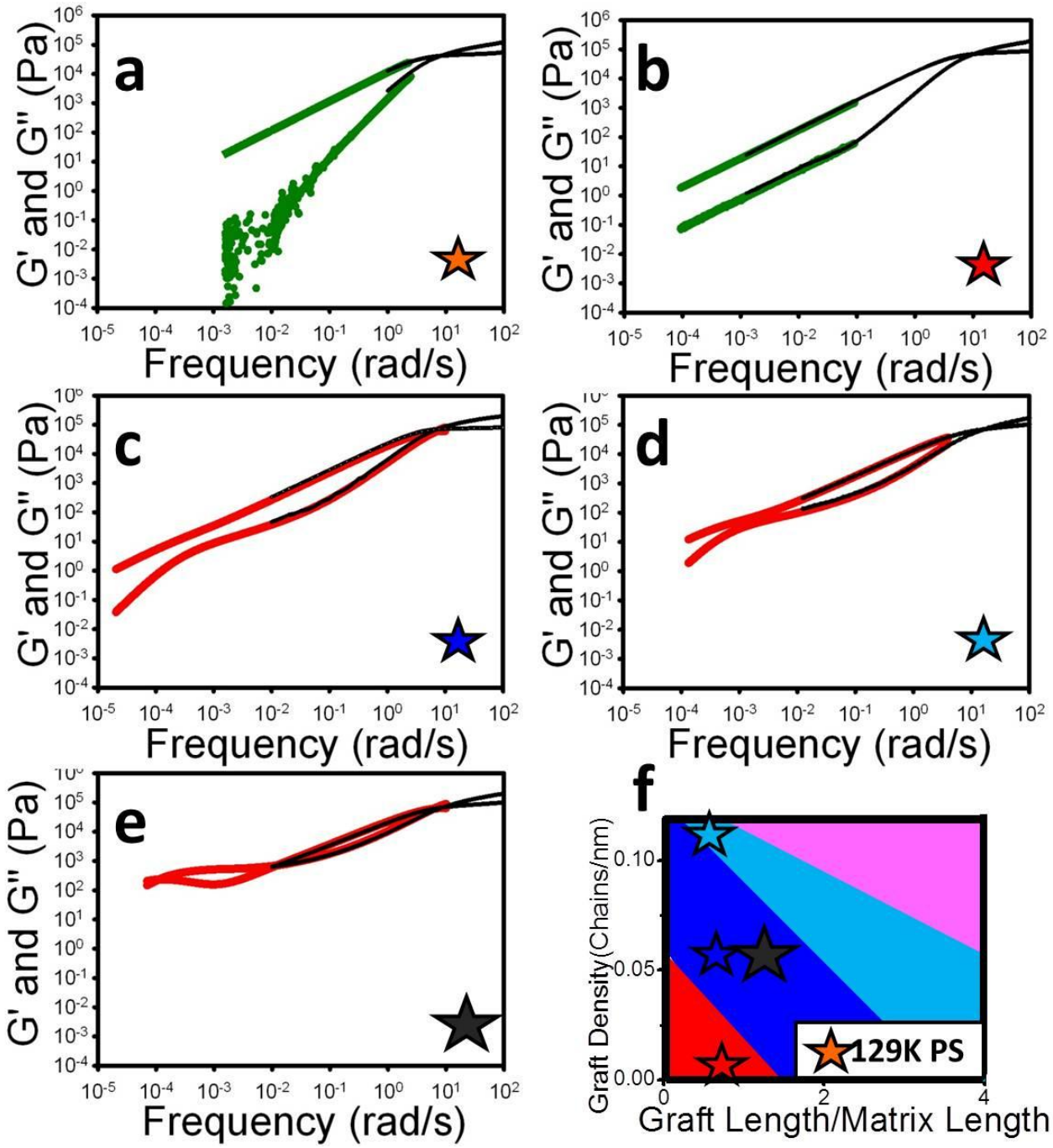

Figure 2.5 *Low frequency/long time linear rheological data for the four composites and corresponding homopolymer from Table 2.2. SAOS (black lines) probes the high frequency regime and converted creep (green points) and stress relaxation (red lines) are used to extend the SAOS to much lower frequencies. Data are presented for the 129 kg/mol homopolymer (a), aggregate (b), connected (c) and string (d) composites at 5 weight % SiO_2 content, and a connected composite at 8 weight % SiO_2 content. The stars in the plots correspond to the location of the samples in the morphology diagram (f). All of the samples have a storage modulus higher than the loss modulus at high frequencies and then these variables quickly cross over. Only for the 8% composite does the storage modulus eventually cross back above the loss modulus and form a plateau, although the connected and string samples come close.*

SAOS data from the Physica taken on the same sample, to ensure that overlap between the two occurs. Table 2.2 gives experimental details of the composites studied, which were all in a 129.2 kg/mol matrix. For the homopolymer and the aggregate composite, the creep conversion to SAOS matched the high frequency SAOS data (green and black curves respectively in Figure 2.5a and 2.5b), however, for the remaining composites, no linear regime was found for creep. The Anton Paar stress relaxation data for these samples was in the linear regime. The conversion of this data overlaid perfectly with the high frequency SAOS (red and black curves respectively in Figure 2.5c and 2.5d) and since the creep experiments were non-linear in these composites, the stress relaxation conversion was used.

For the 8% composite (Figure 2.5e), a second stress relaxation experiment (not shown) had a longer terminal relaxation time than the first (red curve in Figure 2.5e), suggesting a buildup of structure. Thus apparently, an equilibrium structure had not been reached even after five days annealing. Considering that at 5 weight %, some structures continue to evolve after five days annealing, and that the 8% composite was effectively annealing for the entirety of the first stress relaxation experiment (>100,000s), this result is not unreasonable.

Table 2.2 *Brush number-average molecular weights (M_n), polydispersities (PDI), graft densities, matrix solvent quality, and morphologies for SAOS samples.*

Graft density (chains/nm^2)	Graft M_n (kg/mol)	Graft PDI	Matrix Solvent Quality (α)	Morphology	Presence of plateau?	Onset of Terminal Relaxation(s)
0.01	78	1.3	0.60	aggregates	No	too long to measure
0.05	79.9	1.41	0.61	connected	ambiguous	~10,000
0.05, 8 wt %	114	1.15	0.88	connected	Yes (~400 Pa)	10,000-100,000
0.11	70	1.1	0.54	strings	ambiguous	~400

The response of the homopolymer is consistent with what is expected for a linear polymer above the entanglement molecular weight. Meanwhile, an aggregate dispersion state often leads to a rheological response similar to that of the homopolymer, as will be seen again and again in this text, however these results show there is a clear deviation at low frequencies/long times. The storage and loss moduli, when plotted on a log-log plot, are parallel to each other. This suggests this composite is behaving as a critical gel at these timescales[92].

All of the samples show an initial crossover between G' and G'' with G' higher at high frequencies and then quickly falling below G''. Only the 8% composite shows a second crossover in the two moduli, however, both the connected and string structures come close.

From the data, it is clear that the 8% sample has the strongest rheological response. This sample takes a very long time to reach the terminal relaxation regime and the length of time seems to increase with annealing.

2.3 Non-linear Rheology

While the picture derived from linear rheology clearly indicates the necessity of the percolation of a particle network for maximum reinforcement, the role of the polymer is not resolved. If it does play a role, then does the scenario of Long et al. or the Goritz picture (as discussed in Section 1.5) have more relevance? Recall that Long suggested that particle percolation is mediated by the overlap of adsorbed, glassy layers of polymer on the particle surface whereas Goritz postulated it was the bridging of polymers between particles. In order to fully probe the polymer network, non-linear rheology is necessary. The primary experiment used is start-up of steady shear, and from the results that will be presented it will become clear that these steady shear experiments have the ability to break-up particle networks, either temporarily or permanently depending on the composite. Throughout the course of my Ph.D., many

Table 2.3 *Brush and matrix number-average molecular weights (M_n), polydispersities (PDI), brush graft densities, matrix solvent quality, morphologies, and reinforcement metric for studied samples.*

Graft density (chains/nm^2)	Graft M_n (kg/mol)	Graft PDI	Matrix M_n (kg/mol)	Matrix PDI	Matrix Solvent Quality (α)	Morphology	Overshoot/plateau
0.01	25	1.2	142	1.04	0.18	aggregates	1.08
0.01	158	1.5	142	1.04	1.11	sheets	1.07
0.01	158	1.5	42.2	1.04	3.76	connected	1.40
0.05	17	1.05	142	1.04	0.12	connected	1.48
0.05	17	1.05	42.2	1.04	0.40	connected	1.82
0.05	100	1.2	131.4	1.01	0.76	connected	1.83
0.05	17	1.05	42.2	1.04	0.81	connected	1.82
0.05	160	1.21	142	1.04	1.13	connected	1.36
0.05	160	1.21	42.2	1.04	3.79	strings	1.23
0.1	24	1.04	142	1.04	0.17	sheets	1.17
0.1	45	1.06	142	1.04	0.32	connected	1.38
0.1	24	1.04	42.2	1.04	0.57	connected	1.35
0.1	154	1.25	42.2	1.04	3.65	dispersed	no overshoot

different steady shear experiments were performed. In this chapter, I focus on results from 13 nanocomosites that represent the full range of the morphology phase diagram (Figure 1.3). Relevant experimental details on these samples are listed in Table 2.3.

2.3.1 Start-up of Steady Shear

Start-up of steady shear experiments at a variety of strain rates (0.01-0.5 s^{-1}) show the same qualitative behavior—e.g., a stress maximum as a function of time with the strain value at the stress maximum decreasing slightly with decreasing strain rate (Figure 2.6). Similar results have been previously reported[93], in agreement with the notion that this stress maximum, which is a manifestation of the transient elastic (or solid-like)behavior of the reinforced samples, must disappear in the limit of zero strain rate. Thus at these low rates, the characteristic overshoot occurs at the same strain, independent of rate. Flow reversal experiments were performed to determine whether the overshoot is recoverable; samples that had been sheared past the stress maximum at a shear rate of 0.2 s^{-1} were reannealed for 1 week at 150 ° C. These samples displayed an overshoot, albeit weakened suggesting whatever structural breakdown occurs is at least partially recoverable.

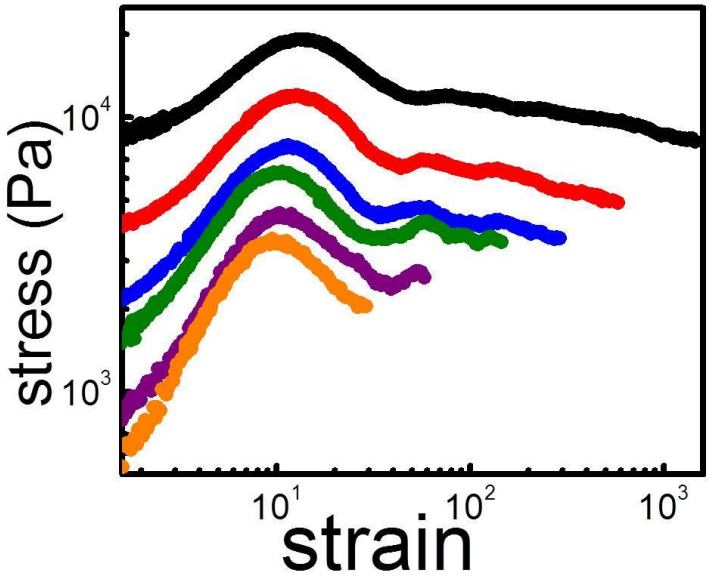

Figure 2.6 *Strain of the shear stress overshoot is roughly independent of shear rate (at these low rates) in the start-up of steady shear at 180 °C. The sample was sheared at six different rates: 0.5 (black), 0.2 (red), 0.1 (blue), 0.05 (green), 0.02 (purple), and 0.01 (orange) (s^{-1}). The grafted chain length is 100 kg/mol, the graft density is 0.05 chains/nm^2, and the matrix chain length is 132.9 kg/mol. Electron micrographs confirm a connected nanoparticle structure.*

Of the 13 nanocomposites studied and listed in Table 2.3 only the sample with well dispersed nanoparticles showed no overshoot. Past work in the Kumar lab has shown that the well-dispersed sample will also show solid like behavior, but at higher particle concentration (~15 wt % SiO_2)[10]. In Figure 2.7, three nanocomposites from Table 2.3 are considered. The grafted chain length to matrix chain length ratio was held roughly constant, and the graft density was varied in the range 0.01-0.1 chains/nm^2. Start-up of steady shear experiments (Figure 2.7a) display a stress overshoot in each case, although the peak is small in the nanocomposite with small particle agglomerates. A maximum in stress overshoot is seen for the intermediate graft density. These results are corroborated by linear oscillatory

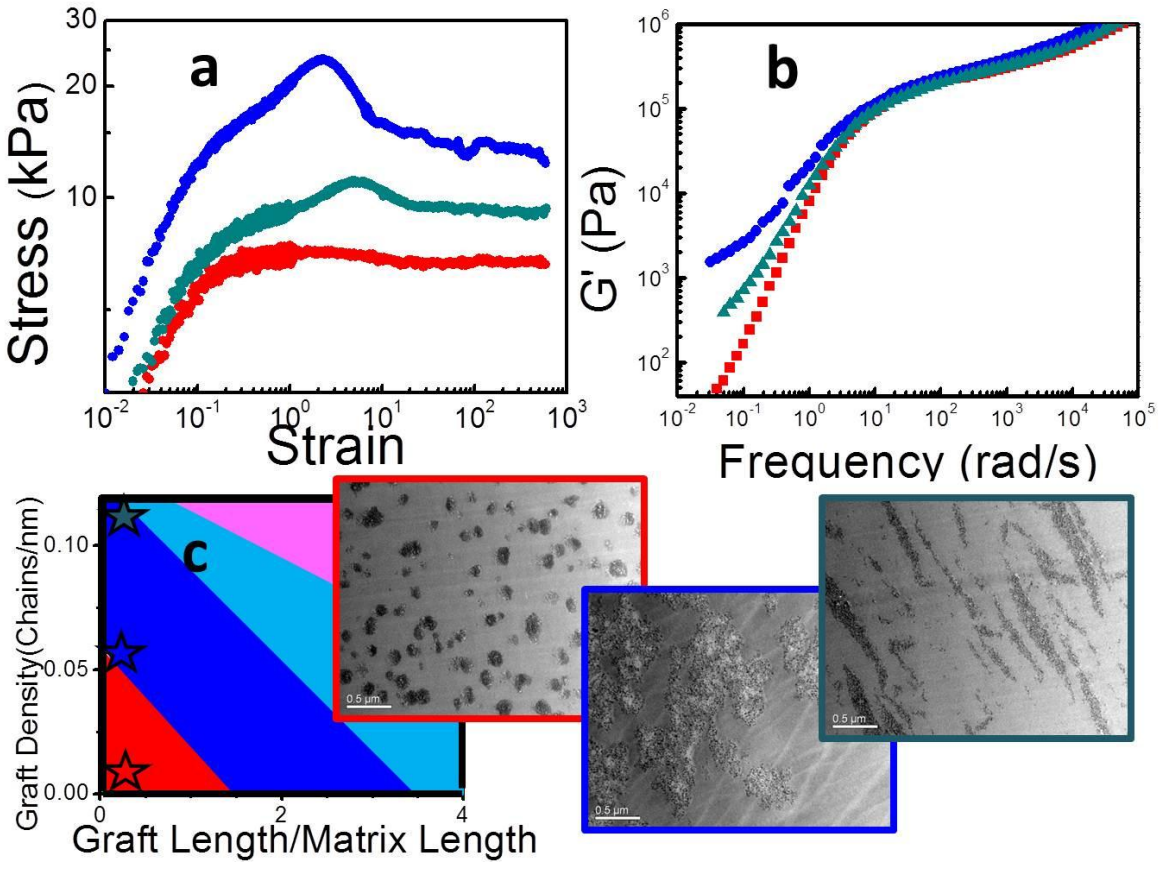

Figure 2.7 *Start-up of steady shear data at 180 °C at a shear rate of 0.2 s^{-1} (a) and storage modulus data(also taken at 180 °C) for three nanocomposites with three distinct graft densities from the 'morphology diagram' representing spherical aggregates (red), a particle network (blue), and sheets of particles (teal). TEMs and the relative positions in the morphology diagram are also shown (c). All three samples have a 142 kg/mol matrix. For the aggregate sample, the graft molecular weight is 25 kg/mol and the graft density is 0.01 chains/nm^2. For the particle network and the sheets of particles these values are 17 kg/mol and 0.05 chains/nm^2 and 24 kg/mol and 0.1 chains/nm^2 respectively.*

shear experiments, which show that this intermediate graft density also has the most reinforcement (in line with the discussion from Section 2.2.1), as evidenced by the height of the low-frequency modulus in Figure 2.7b. The location in the experimental 'morphology diagram' as well as TEM micrographs are both shown for the three distinct dispersion states (agglomerated clusters, a connected nanoparticle network, and sheets) in Figure 2.7c. The dimensionality of these structures was determined by comparing consecutive microtomed slices of sample[43]. Thus, both steady shear and SAOS suggest that the reinforcement is strongly correlated to the nanoparticle morphology, with an apparent maximum being obtained when the particle structures percolate. This is in line with the expectations of Payne, Gusev, and many other past works, including from the Kumar group [93-95].

2.3.2 A Maximum in the Morphology Diagram

To critically resolve the role of the polymer matrix, it is important to consider samples spanning the whole morphology diagram (Figure 1.3). A difficulty is that the matrix polymer molecular weight has to be varied to achieve the desired broad range of the ratio of the graft length to matrix length. Since there is a strong dependence of the absolute values of the modulus on the matrix molecular weight, a measure of mechanical reinforcement is needed that normalizes out this variable. The stress value at the peak of the overshoot scaled by the stress plateau value at large strain (long time) is particularly appropriate, as utilized previously[93, 96]. This analysis (Figure 2.8) shows that, as expected, the largest reinforcement occurs in the regions corresponding to networks of particles. Perhaps more interesting is the trend seen for various percolated samples, all with similar morphologies, but with widely varying graft densities—apparently, the reinforcement goes through a maximum at an intermediate graft density (0.05 chains/nm2). This result offers a crucial insight—the graft chains play a central role in reinforcement. Were a particle-only scenario operative, then the maximum reinforcement would be in the limit of very low graft densities, where the particle cores can contact other cores. This point is elaborated on in Section 2.3.3.

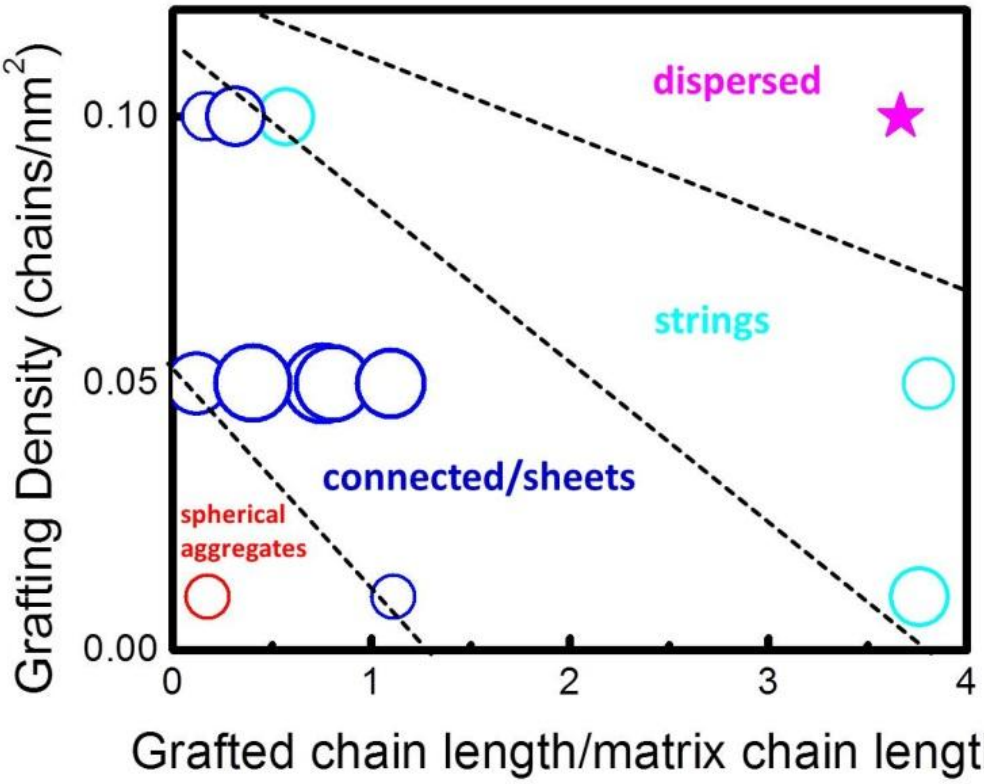

Figure 2.8 *In this 'morphology diagram' symbols are plotted whose size scale with the degree of reinforcement as characterized by the ratio stress overshoot maximum value/plateau value. Other measures give qualitatively similar results (i.e. the connected sheet regime, at intermediate graft density, provides the best reinforcement). Only the well-dispersed sample yielded no stress maximum.*

2.3.3 Graft Length and Overshoot Strain

More insight into the mechanism of reinforcement, specifically, the role of graft chains, results when we plot the strain value at both the shear stress (σ)maximum and the primary normal stress (N1) maximum as a function of grafted chain length (Figure 2.9). N1 is plotted along with σ because it displays a maximum in all filled samples, even in cases where the dispersion state does not allow for a nanoparticle network to span the material (and thus no shear stress maximum exists). The observed strong linear correlation in this figure implies that the stress maximum is driven by the existence of a particle network, where the network "connectivity" is transmitted by the graft chains. Thus, while the dispersion state of the filler is primarily responsible for the magnitude of reinforcement, the presence of

the graft chains enhances this effect. Apparently, this increases the strain to "break" the particle network, which it is conjectured is the origin of the stress maximum. The next pertinent question is why the stress maximum is optimized only at an intermediate graft density and why both lower and higher graft densities show lower reinforcement. For extremely low graft densities, there are very few graft chains—since it appears that the "interaction" of graft chains is crucial, it then follows that low graft densities do not offer substantial reinforcement. The reduction of reinforcement at high graft densities is attributed to the particular shape of the morphology diagram (Figure 1.3)—as one increases the graft density, the x-axis values have to get smaller to maintain a given morphology (in this case particle morphologies which percolate). Consider a fixed matrix molecular weight—this implies that the grafted chain length must decrease as graft chain density increases to maintain the same morphology. Since the extent of the interaction between graft chains is expected to decrease with decreasing graft length, then it follows that the stress reinforcement must eventually decrease with increasing graft density for a given particle morphology. For 14 nm SiO_2 at 5 weight percent, the typical spacing between particles is ~50 nm. The longest grafts with Mn ≈ 160 kg/mol have size of ~20 nm, but at 0.01 chains/nm^2 there are only 6 graft chains on each particle so they barely entangle, while at 0.05 chains/nm^2 there are 30 graft chains on each particle and they entangle significantly. For graft density 0.1 chains/nm^2 shorter grafts with Mn <

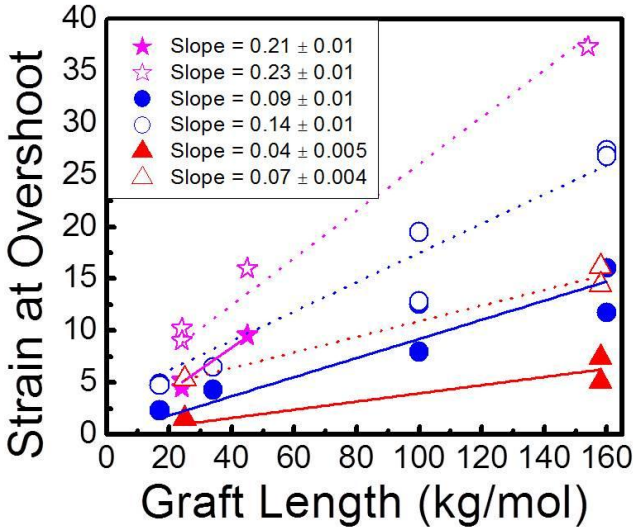

Figure 2.9 *Deformation necessary for the shear stress overshoot increases linearly as a function of the grafted chain length. We consider three graft densities: 0.1 chains/nm^2 (pink stars), 0.05 chains/nm^2 (blue circles), and 0.01 chains/nm^2 (red triangles). Both N_1 overshoot (open symbols) and σ overshoot strains (closed symbols) are displayed. The lines are simply guides to the eye.*

50 kg/mol are used, and these have size smaller than 15 nm and cannot reach the grafts on other particles so they cannot form graft-graft entanglements. In combination, all these results argue for the crucial role of graft chains in mechanical reinforcement in this system.

3. Alignment of Grafted Particle Structures in Response to Flow

In this chapter the use of shear flow fields to orient and order polymer grafted SiO_2 nanoparticle self-assembled structures and potentially affect the growth of these domains is examined. This is important to create materials with directionally dependent properties. In contrast to large particles, of characteristic size R, where hydrodynamics controls flow-alignment and assembly, the nanoparticles at hand are much smaller. Thus alignment will not operate under these mechanisms.

Three flavors of experiments are conducted – SAOS, start-up of steady shear, and LAOS – on a variety of the morphologies from the experimental morphology diagram (Figure 1.3). Both a parallel plate and a specialized cone-partitioned-plate set-up were used, and yielded qualitatively similar results implying that the geometry does not affect the experiment's answer. All sets of rheology experiments were conducted at 180^0C, 80^0C above the glass transition temperature (T_g) of PS. The start-up of steady shear results showed important differences in stress/strain curves for the different NP dispersion states (this was discussed in detail in Section 2.3). Specifically, a smooth increase of stress to steady-state was observed, without any occurrence of overshoot (or occasionally a very small overshoot), when the initial nanocomposite dispersion state was small spherical aggregates, or well dispersed nanoparticles. Every intermediate dispersion studied, ranging from strings to fractal networks of particles or sheets, demonstrated a stress overshoot. Note that, in linear oscillatory shear, for all composites, the low-frequency (<10rad/s) storage modulus decreases at a slower rate (with decreasing frequency) from what was observed with the homopolymer. Whereas for an aggregate dispersion state this change is small, the effect is much larger for interconnected or string structures (see Figure 2.1).

To determine the structural origins of these qualitatively different stress responses, TEM was performed (conclusions were verified using ultra small angle x-ray scattering[97] (USAXS) using a unified fit model[98]). A series of eight start-up of steady shear experiments were performed on two different initial dispersion states, one in which the nanoparticles are arranged into small aggregates, and one in

which the particles form sheets. The strains chosen were 0, 1, 3, 8, 14, 59, 400, and 1200. These values were selected using the stress overshoot in the self-assembled sheets sample as a reference, since the maximum deformation and alignment was expected and achieved there. Strains on both sides of the stress maximum were studied. Sections 3.3 and 3.4 will discuss in detail representative micrographs for selected strains for the two different dispersion states, a connected network of sheets and spherical aggregates respectively. All the samples discussed in this chapter are listed in Table 3.1.

Table 3.1 *Brush and matrix number-average molecular weights (M_n), polydispersities (PDI), brush graft densities, matrix solvent quality, morphologies and effect of shear on aggregation state for studied samples.*

Graft density (chains/nm^2)	Graft M_n (kg/mol)	Graft PDI	Matrix M_n (kg/mol)	Matrix PDI	Matrix Solvent Quality (α)	Morph-ology	Coarsen with shear ?
0.01	78	1.3	129	1.03	0.60	aggregates	no
0.01	128	1.35	129	1.03	0.99	aggregates	no
0.01	128	1.35	91	1.02	1.41	aggregates	no
0.02	156	1.22	91	1.02	1.71	sheets	yes
0.05	15	1.1	91	1.02	0.16	aggregates	very slight
0.05	52	1.07	129	1.03	0.40	connected	yes
0.05	75	1.06	129	1.03	0.58	connected	yes
0.05	79.9	1.41	129	1.03	0.62	connected	yes
0.05	88.7	1.68	129	1.03	0.69	connected	yes
0.05	120	1.18	129	1.03	0.93	sheets	yes
0.05	120	1.18	91	1.02	1.32	sheets	yes
0.1	66.4	1.2	129	1.03	0.51	connected	yes
0.1	56	1.15	91	1.02	0.62	connected	yes
0.1	154	1.25	42	1.04	3.67	dispersed	no
0.11	70	1.1	129	1.03	0.54	strings	yes

3.1 The Peclet Number and Zeta

The Peclet number is a dimensionless number that can be used to compare the relative importance of the shear flow to movement caused by Brownian diffusion. The Peclet number is defined as in Equation 3.1:

Equation 3.1

$$Pe = \frac{(\dot{g}R)R}{\left[kT \big/ 6pRh\right]} = \frac{6p\dot{g}hR^3}{kT}$$

Here $\dot{\gamma}$ is the shear rate and η is the viscosity. In the case where shear dominates the movement of particles, the Peclet number will be much larger than one and in the diffusion dominated regime it will be smaller than one. In contrast to large particles, of characteristic size R, where hydrodynamics controls flow alignment and assembly and *Pe* is of order 10^3 or larger [99-102] the nanoparticles at hand are much smaller, $Pe \sim O(1)$. Hence, thermal energy induced fluctuations are comparable to flow induced effects. In addition to the Peclet number, a second pertinent dimensionless number in this context is zeta (ζ), which is defined in Equation 3.2 :

Equation 3.2

$$\zeta = \frac{U}{k_b T}$$

ζ emphasizes the relative importance of the interparticle attractions, U, to the thermal energy. Estimations of ζ values in these cases are difficult since we do not know the exact chemistry of the SiO_2 particles of interest. Using a bare (unretarded) London-dispersion formula for SiO_2 spheres at a separation of 1nm yields ζ~2. On the other hand, fits of an analytical model to the Kumar lab's previous quiescent self-assembly experiments suggest ζ~10. Despite this uncertainty, *ζ* unambiguously exceeds *1* at short distances (~1 nm), whereas it becomes negligible at larger separations. Given the fact that the

ratio $Pe/\zeta < 1$, we do not expect flow-effected NP-structure formation. Consistent with this surprising conclusion, it appears that self-assembled anisotropic nanoparticle structures can be oriented into the flow direction with the structures lining up one-behind-the-other so as to minimize drag. However, no flow induced growth of these structures occurs. No such orientational ordering is found in the case of spherical structures, e.g., individual NPs or spherical NP clusters! In contrast to conventional wisdom, these results therefore show that flow can only be used to orient anisotropic nanoparticle structures along streamlines, but that flow itself does not induce any domain growth. These results are highly relevant for the creation of materials with controlled transport behavior such as in gas membranes, organic photovoltaics and batteries.

3.2 Experiment Design

The rheological properties of nanocomposites was investigated, where the spatial dispersion of the nanoparticles were varied systematically[43] from well-dispersed (i.e., NPs miscible in the matrix) to agglomerated into small spheres (presumably due to macroscopic phase separation) as discussed in Section 1.4. Several intermediate states, i.e., strings, sheets and networks, created by particle self-assembly, were also focused on (Figure 1.3).

3.2.1 Composite Preparation and Transition Electron Microscopy

RAFT polymerization is used to grow PS chains of various lengths and densities from 14nm SiO_2 particles. The grafted particles are dissolved in tetrahydrofuran (THF) and monodisperse PS added to this mixture. One hour of mixing using a vortex, followed by pulsed sonication (3 minutes: 2s sonication, 1s rest) are used to thoroughly mix the solution which is then solvent cast into a 60mm Petri dish, dried overnight in a vacuum, and annealed for 5 days at 150°C (10^{-4} torr). The composites are prepared to each be 5% of the SiO_2 core by weight. TEM (including image analysis), SAXS, USAXS and rheology are used to analyze the samples. For TEM, 60nm, microtomed sections are transferred to a copper grid

which has been pre-coated with Formvar. Since orientation is extremely important when looking at nanocomposite response to flow, great care is taken to record the orientation with respect to flow of the sections. To prepare for rheology, the samples are first vacuum dried for several days at 80°C to remove excess solvent. These are then annealed for 5 days at 150°C. Custom molding apparatuses are then used to mold the samples into 8, 10 or 25mm diameter discs depending on the geometry desired for experimentation. The apparatuses are steel cylinders with a hollowed out center. This hollowed out region is also cylindrical in shape, with a diameter that matches the diameter of the resulting sample and a steel plunger is fitted to slide smoothly but tightly up and down the length of this hollowed out region. The plunger should be slightly longer than the encasing steel cylinder. Three screw holes are positioned equidistant from each other around the upper edge of the encasing cylinder and these are used to secure a steel lid in place of the same diameter as the encasing cylinder. The encasing steel cylinder is also fitted with a small hole in which a thermocouple is inserted (such that the tip of the thermocouple will reach very near to the sample within, but not actually contact it). Just above this hole, a large tube extends outward to which a vacuum can be attached to slow sample degradation. Once the lid is screwed in place and the plunger is inserted, a small disc shaped region is available (with one edge of the disc the top edge of the plunger and the other edge of the disc the bottom edge of the lid). This is where the sample is molded and the thickness of the resulting mold will depend on the total amount of sample added into this region. The sample is typically added with the plunger partially inserted and the lid not yet attached. In order to prevent the sample from sticking to the steel, Teflon coated Kapton is cut to fit the top edge of the plunger exactly and a second piece of Kapton, slightly larger than the circular hole, is cut to fit between the sample lid and the encasing steel. Once the sample is in place, the whole apparatus can be fitted with a band heater, a thermocouple and a vacuum. Thus high molding temperatures can be reached in a controlled fashion, under vacuum. The samples are typically molded at 150° C and if the temperature is too much higher the sample will enter into the

spaces between the plunger and the encasing cylinder. All rheology measurements are conducted at 180°C.

In each of the eight experiments, the samples were taken to a different final strain and then quickly quenched to room temperature (the quench time was limited to 5 minutes; upon investigation no further evolution of dispersion state was observed even with much larger quench times in line with behavior seen in similar experiments[103]. The quenched samples were observed using transmission electron microscopy and image analysis was performed, using the average from 100 micrographs.

Images for electron tomography were taken on a JEOL EM-2010 microscope operating at 200 kV. Images were taken from -68 to 68 degrees tilt every 2 degrees (total of 69 images). Inelastically scattered electrons were removed from the images using a Gatan energy filter operating at 0 eV energy loss. Alignment and reconstructions of images were done using IMOD[104]. Visualization of the 3D volume was done using Avizo.

3.2.2 Rheology

In all cases, the microtomed sections were taken 1mm into the 8mm diameter disc. As this is relatively close to the edge of the sample, edge fracture effects were a major concern. Furthermore, in a parallel plate geometry the strain is non-uniform and specifically increases as the radial distance from the disc center is increased. In addition, wall slip may occur while shearing melts. In order to remove any doubt that the dispersion state changes observed were an artifact of the geometry, an 8mm cone and plate geometry with a cone angle of 0.1 radians was used. This was attached to a ring partition, such that diameter of the measured sample was only a fraction of the diameter of the actual sample (discussed in detail in Section 1.1.1). In this set-up, the edge of the sample is no longer measured, and thus the results of any edge effects are significantly delayed (until such time as the edge defects expand inward to the measured portion of the sample[22, 26]).

This altered geometry allowed us to more accurately characterize strain in the sample. Furthermore, because any so-called 'edge effects' will be immediately visible in the rheological data (in the form of an uneven stress plateau), these too can be ruled out. When TEMs of samples sheared in this geometry were taken, the trend of increasing aggregation with increasing strain was unchanged.

3.2.3 Image Analysis

In an attempt to quantify these images, Image J software was used to perform image analysis. To determine aggregation state, a radially averaged autocorrelation function calculation was performed on a series of 100 micrographs taken from the microtomed sections of the quenched samples.

3.3 Flow Response for 'Connected' Sheets

First a sample with self-assembled, but non-percolating particle sheets is considered (Figure 3.1). Here the dispersion shows very large changes with strain. With increasing strain in the regime below stress maximum, $\sigma < \sigma_{max}$, it is clear from the TEM micrographs that the domains initially order along the flow direction (which is parallel to the strain axis). The sheets position themselves one behind the other, leading to macroscopically large, but not connected structures, as observed with TEM tomography (Figure 3.2). This is apparently to reduce drag, which is much larger with sheets than individual particles. We conjecture that, due to strong interparticle attractions, the flow is too weak to reduce drag by breaking the sheets, and hence orients them along the flow direction. This shear-induced domain ordering is maximized in the vicinity of the stress maximum, at which point the domains grow to macroscopic size in one dimension. It is suggested that here there is an analogy with the work on large colloidal particles[100, 105], albeit weak, since hydrodynamics are much less important in our case, Pe~O(1), than in the colloid case where Pe~O(10^3). Under the influence of shear (even weak rate exerts large torque in anisotropic objects), the sheets of particles orient in flow. They eventually

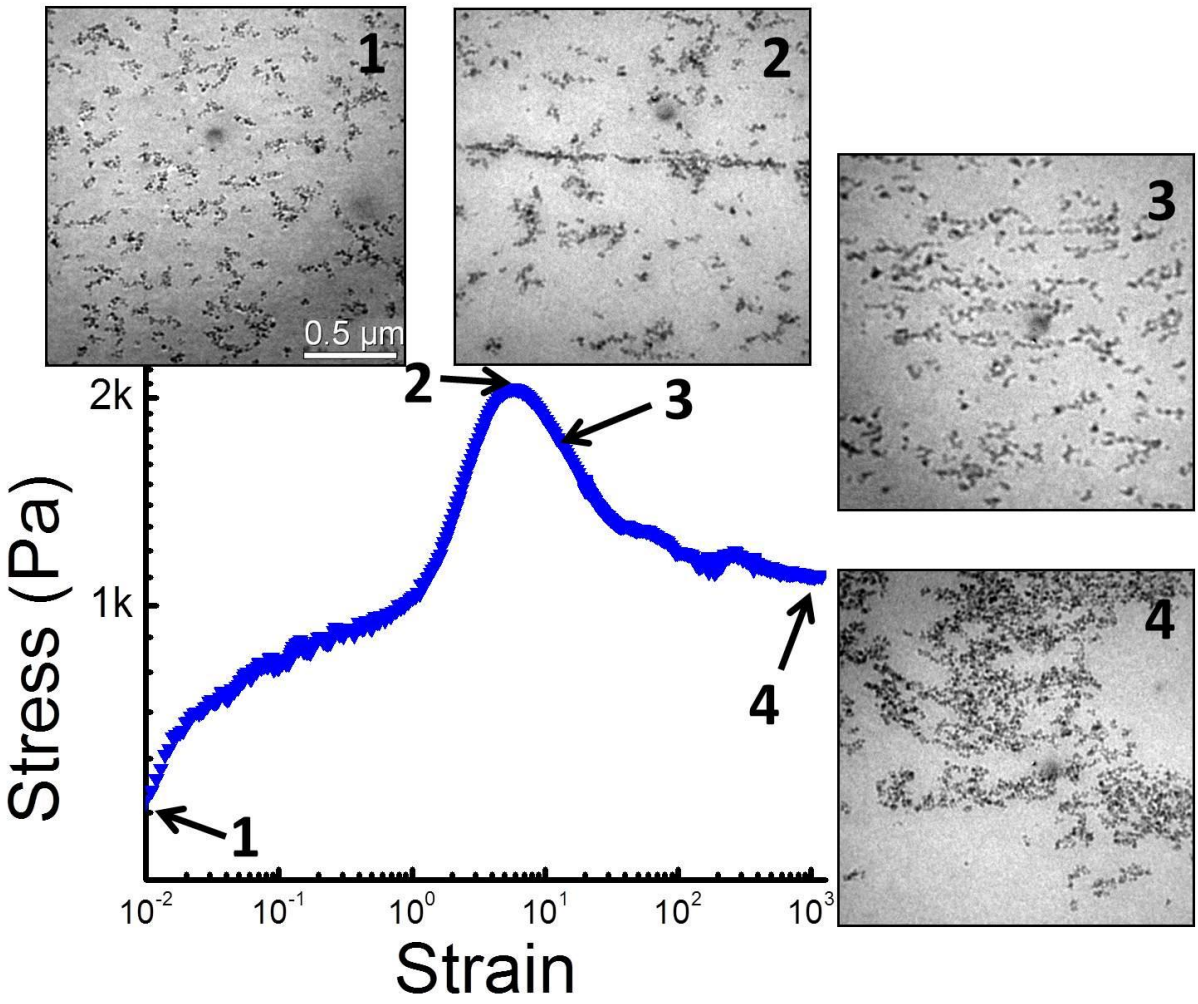

Figure 3.1 *The stress vs. strain relationship during a steady-shear experiment for an interconnected initial dispersion state. The four TEM images show the evolution of morphology in this sample at strains of 0 (1), 8 (2), 14 (3), and 1200 (4). All images are oriented such that the flow and vorticity directions correspond to the horizontal and vertical directions, respectively.*

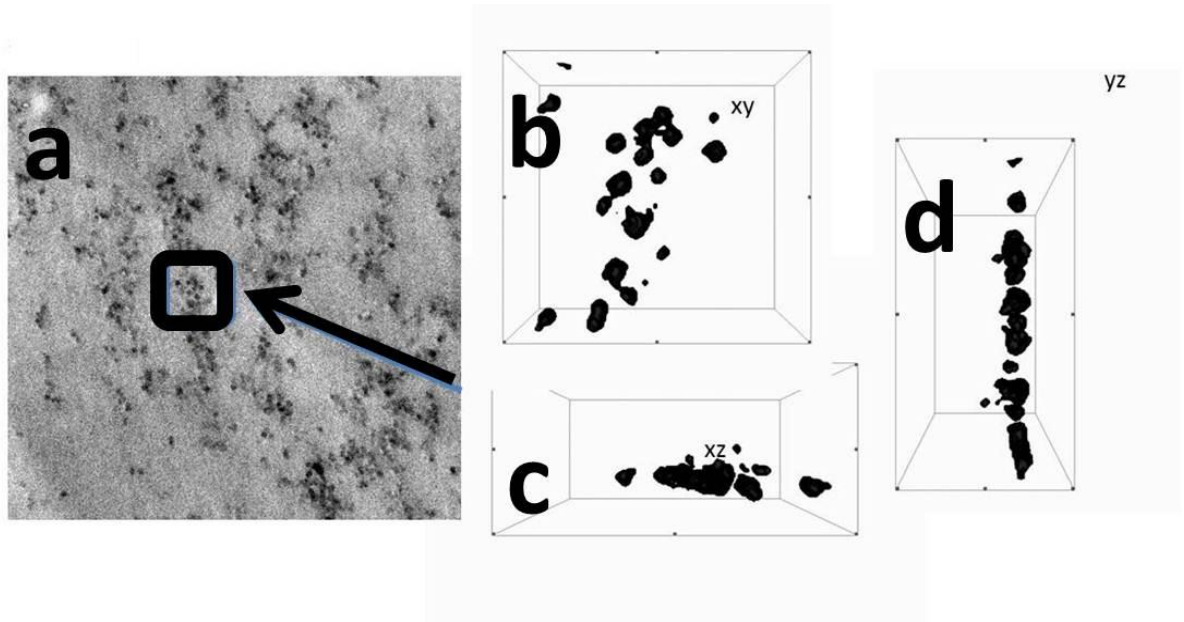

Figure 3.2 *Tomographical data of the sample with a connected nanocomposite structure from* ***Figure 3.1****, strain = 8 (where maximum alignment is seen). (a) A traditional TEM of the sample. (b)-(d) Projections o the 3D reconstruction of the composite in the xy, xz, and yz planes respectively where x is the transverse, y is the flow direction, and z is the vorticity direction.*

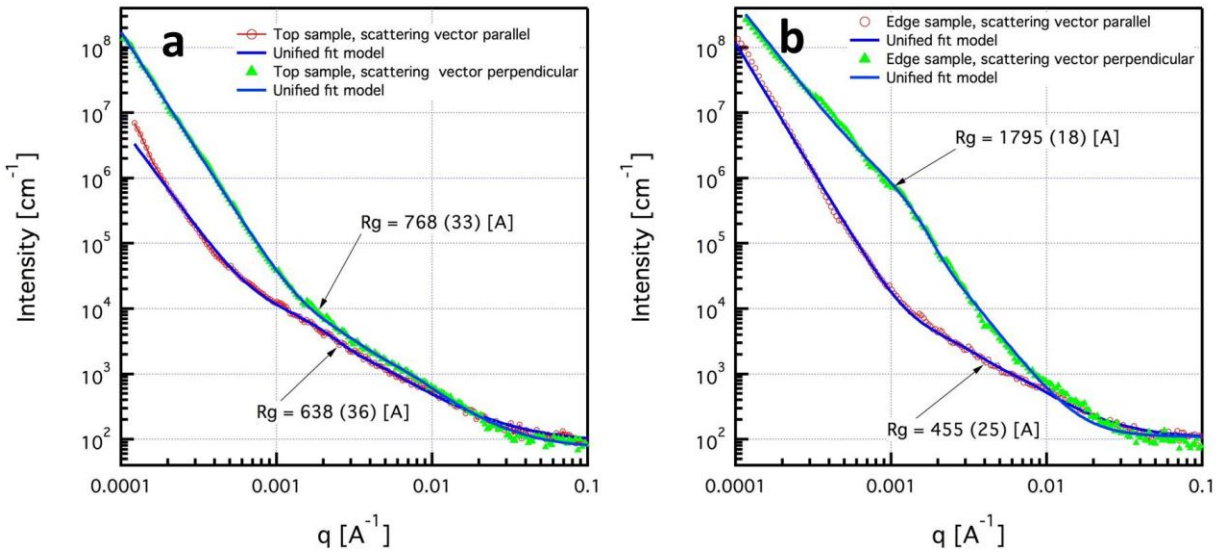

Figure 3.3 *Ultra-small angle x-ray scattering on the 'connected' nanocomposite structure at maximum alignment from* ***Figure 3.1****. Here we look at the sample (disc shaped from the parallel plate geometry) in two distinct directions. (a) Looking through the plane of the disc (top view) and (b) looking down the diameter of the disc (edge view). In each case, we look at scattering in two orthogonal directions. All lines correspond to a unified fit. In the edge on view, we see significantly higher intensity at the intermediate q values for the samples perpendicular to the flow. In the top view, the differences between the perpendicular and parallel samples are negligible. This is consistent with particle sheets that orient themselves one behind the other to reduce drag as was seen in the tomography (****Figure 3.2****).*

align fully in the direction of flow and under the influence of the weak thinning in the elastic matrix they associate forming super-sheets. Hobbie et al. [106] investigated semi-dilute dispersions of carbon nanotubes in a polybutadiene matrix and in a similar flow regime, also saw alignment in the direction of flow.

This alignment with flow is further confirmed with USAXS (Figure 3.3). In this figure, the same quenched rheological sample as in Figure 3.1 is investigated. The USAXS shows an anisotropy which indicates an alignment of the particles in the flow direction (as also visualized in TEM). In Figure 3.3a, the sample is viewed from the top, looking through the plane of the disc from the parallel plate geometry. There is minimal difference in the scattering observed in the two orthogonal directions here. The characteristic length scale in each case is ~70nm. This is consistent with TEMs that were also taken in this orientation, which showed no difference in alignment when the sample is viewed from the top. In contrast, the USAXS clearly shows alignment when the sample is viewed from an edge on view (Figure 3.3b). Here the scattering is clearly anisotropic, with a characteristic length scale that nearly quadruples (from ~45 to ~180nm). Thus the degree of alignment observed in both USAXS and TEM depends on the orientation of the sample. This is consistent with sheets of particles, which orient in the direction of flow, such that when a cross section is viewed from the edge they appear as aligned strings, but when viewed from the top they appear as small clusters of particles with minimal alignment.

Beyond the strain at which maximum alignment is obtained, the domains tend to break-up and coarsen. Similar coarsening with flow has been observed in colloidal gels and other systems[103, 107, 108] and specifically, we find precedent for this in the studies of Rajaram and Mohraz[109, 110]. However, a direct comparison is precluded as their colloid-polymer mixture consists of large particles, has much lower viscosity and the interparticle forces are very strong compared to van der Waals, due to depletion. In the present anisotropic nanoparticle assemblies, the domains break when the integrated

applied shear “energy” is larger than the “bonding” energy. The latter is determined by the vdW attraction of the cores and the star-like engagement of the grafts (i.e. ζ~10). Coarsening of the broken pieces under shear suggests that flow-induced diffusion operates. There are similarities with the work of Mohraz[107], who investigated the flow-alignment of colloidal gels. These systems formed strings aligning 45^0 to the flow in contrast to our case. Note that 45^0 is the most probable direction, that of maximum extension, also observed with rod-like polymers[111]. Finally, no tumbling is observed in this system, presumably due to the large drag and absence of enough momentum to overcome it. This is expected given the strong viscoelastic nature of the matrix [105, 112]. The above points are also well illustrated in the calculated radially averaged correlation function as well as its components along the flow and vorticity direction (Figure 3.4). We see an aggregation, or coarsening of the dispersion state, that begins after the maximum in stress. When we analyze the aggregation in the flow and vorticity directions, we see no change in aggregation in the vorticity direction until after the stress maximum, but a steady change in aggregation in the flow direction. It is thus apparent that the orientation and ordering of domains is maximized close to the stress maximum. This result establishes a deep connection between the nanoparticle morphology in the system and the rheological behavior of the material. Hence, as in typical thixotropic materials, the flow history controls sample morphology.

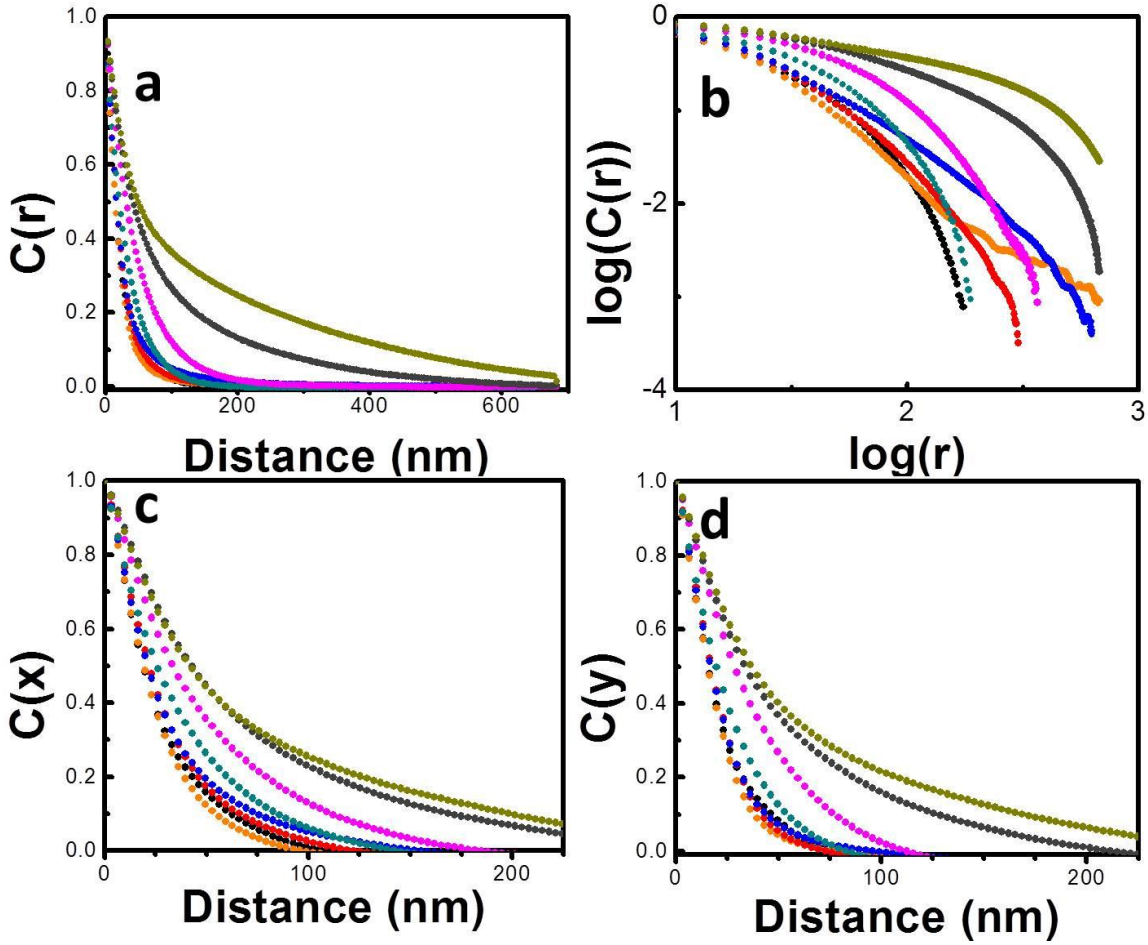

Figure 3.4 *Radially averaged autocorrelation function in both a linear (a) and a log-log (b) plot for the sample from Figure 3.1. The 1-dimensional autocorrelation function in the flow(c) and vorticity(d) directions are also shown. Each curve is the result of image analysis performed on 100 separate micrographs using Image J software. The different colors represent 8 different strains at which quenching occurs: 0(black), 1(orange), 3(red), 8(blue), 14(teal), 59(pink), 400(gray), and 1200(olive).*

3.4 Flow Response for 'Isolated Aggregates'

A nanocomposite, comprised of spherical nanoparticle clusters, which displayed effectively no stress overshoot is considered next. Judged from the rheological and TEM analysis shown in Figure 3.5, it is apparent that this sample shows hardly any changes in aggregation state with the application of strain. This result is also reflected in the calculated radially averaged correlation function, which remains practically invariant with applied strain as well, and the two components of the correlation function,

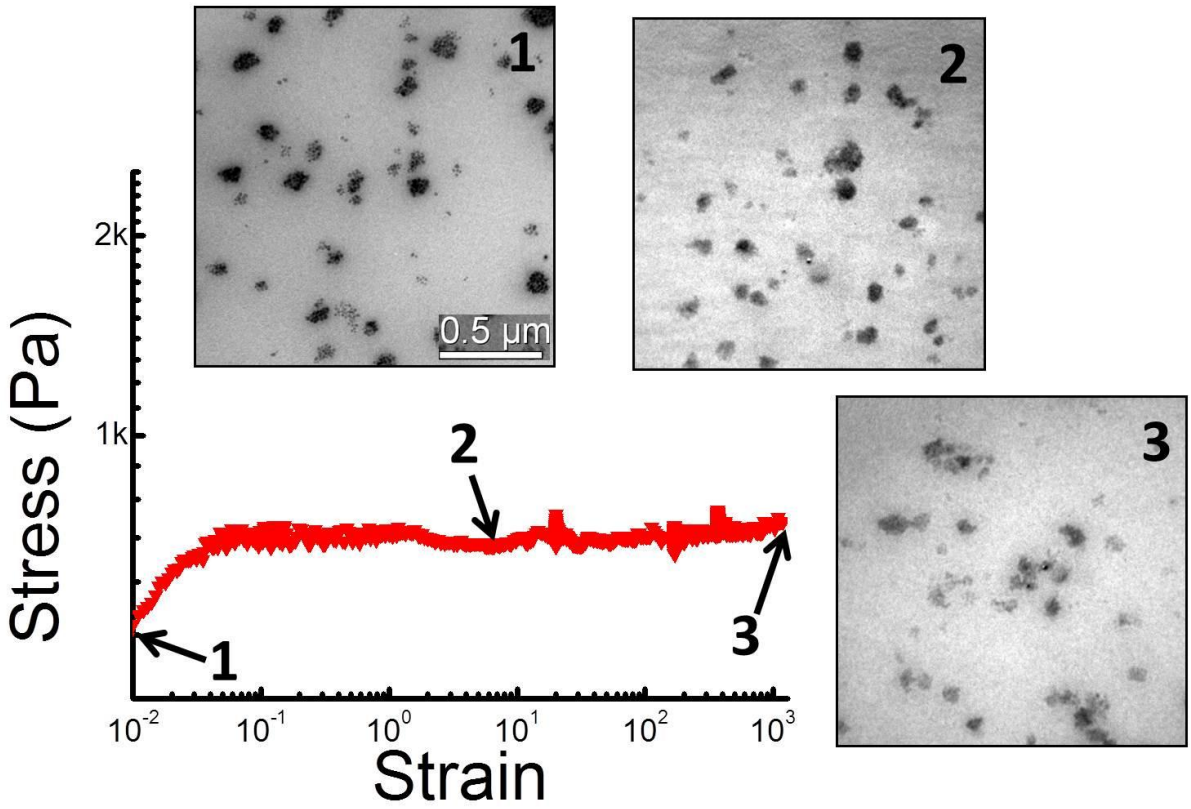

Figure 3.5 *The stress vs. strain relationship during a steady shear experiment for an initial dispersion state of small particle aggregates. The TEM images are at strains of 0 (1), 8 (2), and 1200 (3). In the aggregate case, there is no change in dispersion state with applied strain. All images are oriented such that the flow and vorticity directions are the horizontal and vertical directions, respectively.*

along the flow direction and vorticity direction also show minimal changes on the application of strain(Figure 3.6). We briefly discuss these results in light of the previous work of Pasquino et al. [113] who have suggested that the application of steady shear to a shear-thinning, shear-banding wormlike micellar solution containing micron-sized, spherical particles caused the particles to chain and eventually crystallize in the flow direction. These authors observed no stress overshoot in their case, and besides the very different matrix, the large particles in their study were non-Brownian and the combination of hydrodynamic effects along with the matrix normal forces and banding instability of the matrix appears to be responsible for the observed ordering[114], which occurs at much higher strains than those used currently. In the present case of nanoparticle structures with Pe~O(1), the matrix is a

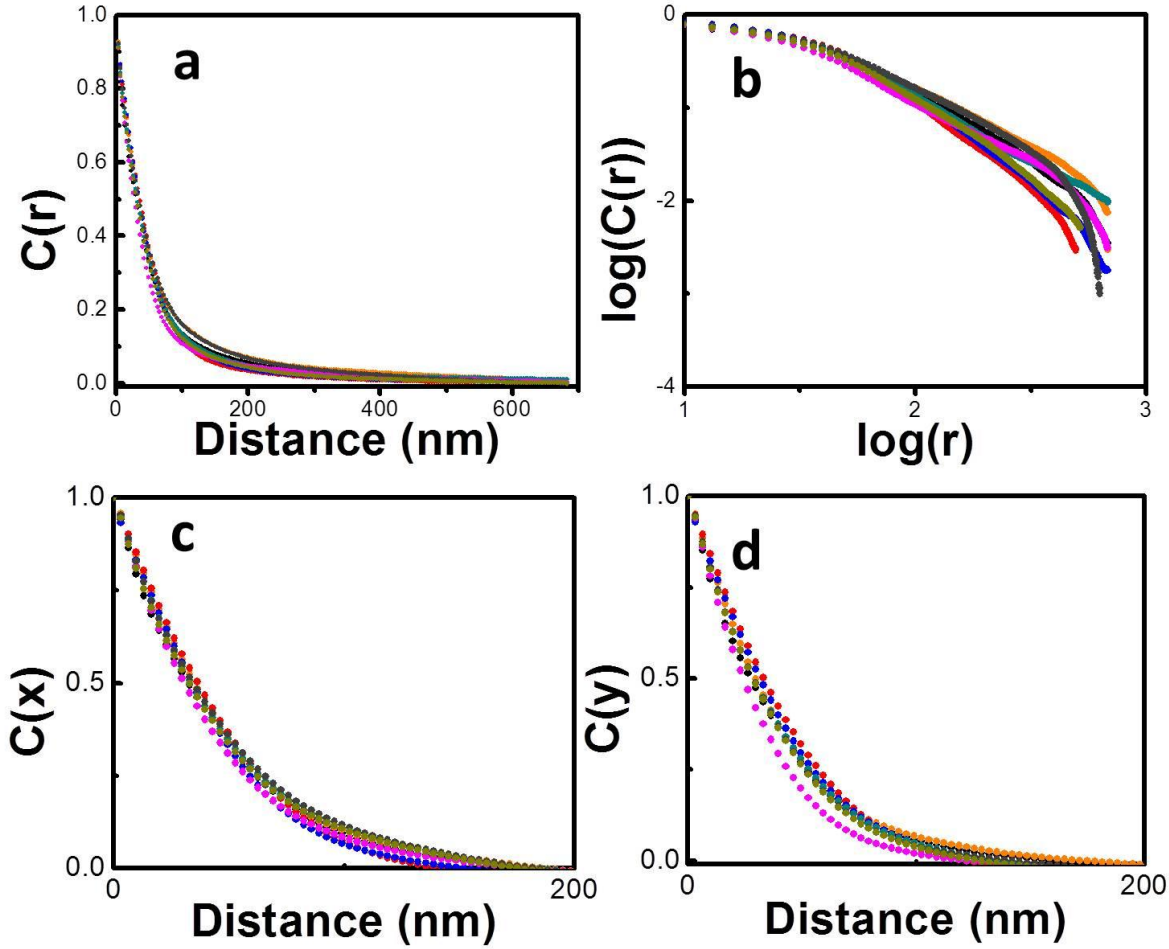

Figure 3.6 *Radially averaged autocorrelation function in both a linear (a) and a log-log (b) plot for the sample from Figure 3.5. The 1-dimensional autocorrelation function in the flow(c) and vorticity(d) directions are also shown. Each curve is the result of image analysis performed on 100 separate micrographs using Image J software. The different colors represent 8 different strains at which quenching occurs: 0(black), 1(orange), 3(red), 8(blue), 14(teal), 59(pink), 400(gray), and 1200(olive).*

weakly thinning but highly viscoelastic polymer melt far from any instability region. In addition, the attraction between nanoparticles is important, and hence the above conditions for shear-chaining and order of particles are not met. Therefore, nanometer-sized particles show qualitatively different behavior than their micron sized-analogs and the difference is attributed to a combination of their Brownian nature, interparticle forces and the matrix. Note that no order is observed when shearing Brownian suspensions of Newtonian particles at Pe=1[115].

3.5 Dispersion Effects on Degree of Aggregation with Shear

To establish the generality of these results we have examined a variety of systems on our "quiescent" morphology plot (Figure 1.3) which delineates regions where different structures form. We observe that the regions that have a particle network and thus show maximum reinforcement (Figure 2.8) [116], also show the greatest degree of coarsening with flow. In Figure 3.7 a quantitative analysis is performed on four composites from the morphology diagram, and the difference between the radially averaged autocorrelation is unequivocally greatest in the conneted/sheet morphology regime. These results can be qualitatively understood in Figure 3.8, in which several samples are shown before and after steady shear. The inset shows the location of these samples in the morphology diagram (Figure 1.3). Note that there is no dispersion change with spherical aggregates or well-dispersed particles, but in other cases, there is some obvious change, usually comprised of particle aggregation.

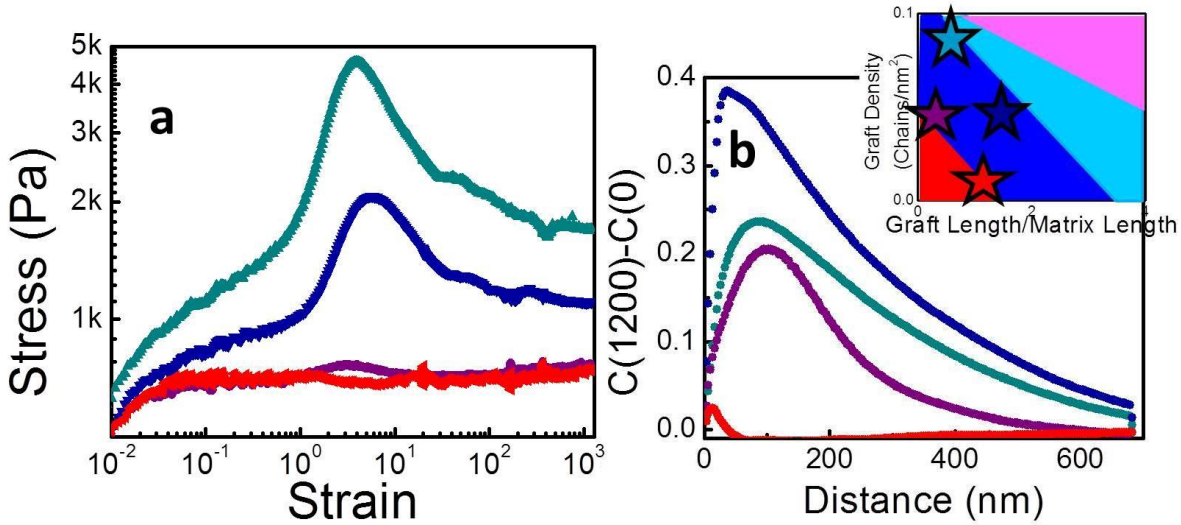

Figure 3.7 *Amount of aggregation subsequent to shear (strain = 1200) as a function of nanoparticle dispersion state. Aggregation is the greatest when dispersion is such as has been found to maximize mechanical reinforcement (see* ***Figure 2.8****). Both the steady state shear response of the composites at a shear rate of 0.1 (a) and the total aggregation, as measured by subtracting the autocorrelation of the quiescent composite from the autocorrelation of the strained composite (b) are shown. In the inset the location of the samples in the morphology diagram are displayed.*

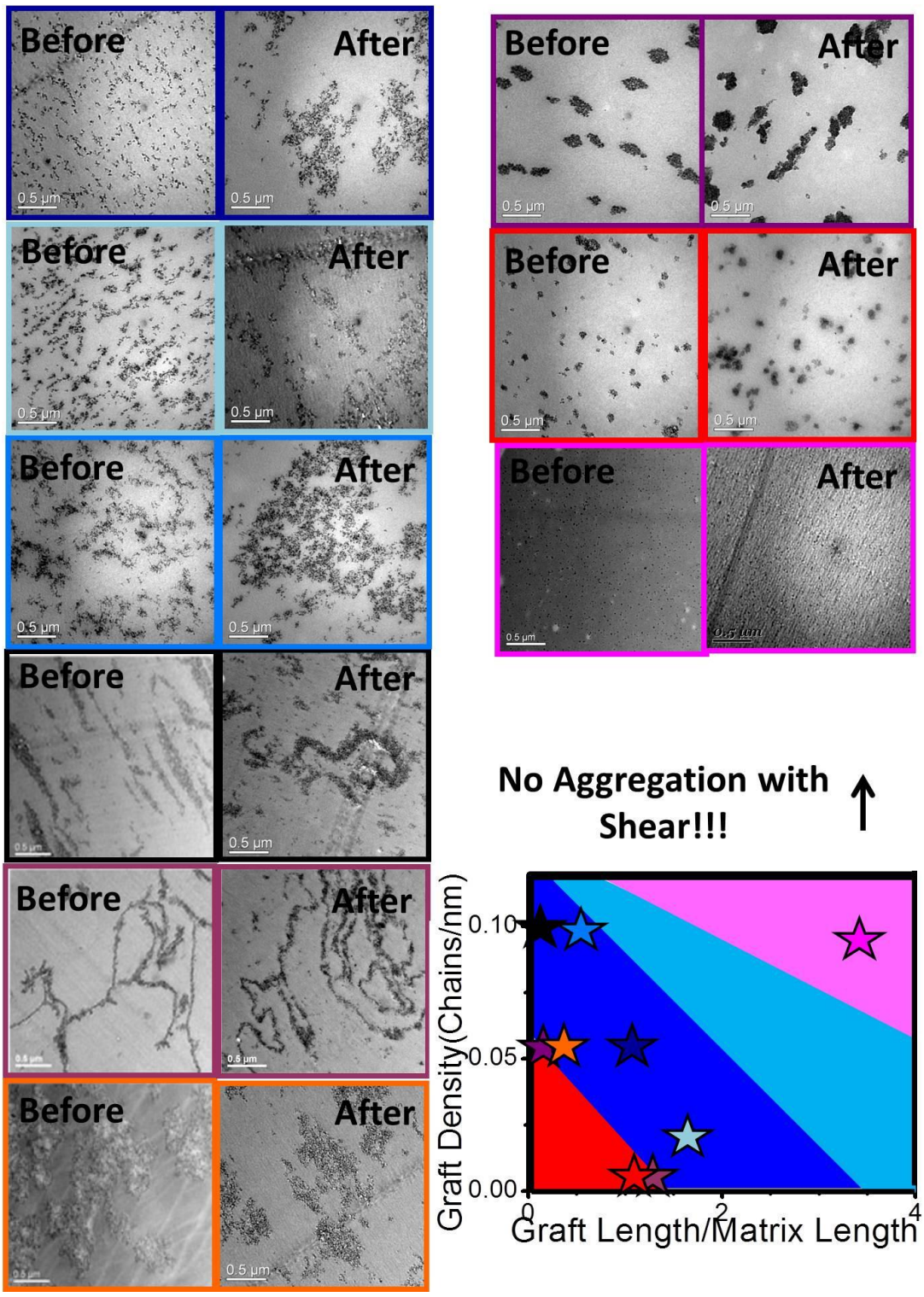

Figure 3.8 *TEMs before and after steady shear on 9 different nanocomposites that were taken to large strains(well past the overshoot). The location of the samples in the morphology diagram is also shown. For samples in the well dispersed region(magenta in the morphology diagram), or near or in the spherical aggregate region(red in morphology diagram), little or no aggregation is seen. The maximum aggregation is in the connected/sheet region (blue in the morphology diagram).*

3.6 Large Amplitude Oscillatory Shear as a Route to Alignment

The particle alignment which peaks at the stress overshoot is of particular interest because of its ability to impart directional properties. In this regard, optimizing the flow conditions for most effective alignment is a formidable challenge. Motivated by the body of work on alignment induced during large amplitude oscillatory shear (LAOS) in block copolymers[14, 15] we attempted to improve the alignment of the anisotropic SiO_2 nanoparticle assemblies using LAOS experiments and (in the case were the desired strains are prohibitively large for the ARES oscillatory motor mode) a series of flow reversal in steady-shear experiments. LAOS experiments were employed at a variety of different frequencies, in both parallel plate and cone and plate geometry and at maximum strains that ranged from roughly half the strain at which the overshoot occurred up to 10-15 times the overshoot strain. The primary set of LAOS experiments were done at strains just before or just after the strain of the stress overshoot. The rationale was as follows: The stress overshoot in steady shear experiments had been indicated to correspond to the maximum alignment and percolation of the sample (Section 3.3). Thus LAOS experiments with strains near the overshoot were deemed necessary. However, we have also shown that strains beyond this overshoot correspond to the breaking or coarsening of the nanoparticle structures. Two scenarios were thus possible: The structure might need to be broken and then re-form in a more aligned state in order to increase alignment, or the breaking of the structure might be detrimental to alignment, and instead increase coarsening. In fact, none of the many experimental conditions that were tried were successful in improving alignment beyond what was achievable with steady shear. To illustrate this point, we took the LAOS sample that had the best visually apparent qualitative alignment (as judged from TEM micrographs) and compared it to the alignment of its 'sister' sample that had been sheared unidirectionally. In Figure 3.9, the autocorrelation function in the vorticity direction is subtracted from the autocorrelation function in the flow direction for each of these two

samples. This can then be used as a measure of the overall alignment, and as can be seen in the figure, in both cases, the alignment is the same within reasonable error margins.

Thus the ultraslow timescales for the growth and equilibration of our nanocomposite structures preclude reordering and alignment on the time scale of a period of oscillation. Essentially, the various dispersion states from our phase diagram take days to form. In contrast, in LAOS of block copolymers, the structures break during the LAOS experiment, but reform quickly enough that oscillatory shear can be used to align them. In our case, for the structures to re-form, so as to be fully in equilibrium with the flow, takes too much time (as judged from their linear viscoelastic response[10, 43]) and thus the more likely scenario is either no effect, or the coarsening seen at large strains in steady shear. Further, due to the strong attractive forces holding these clusters together, it is unlikely they will deform in response to the flow field.

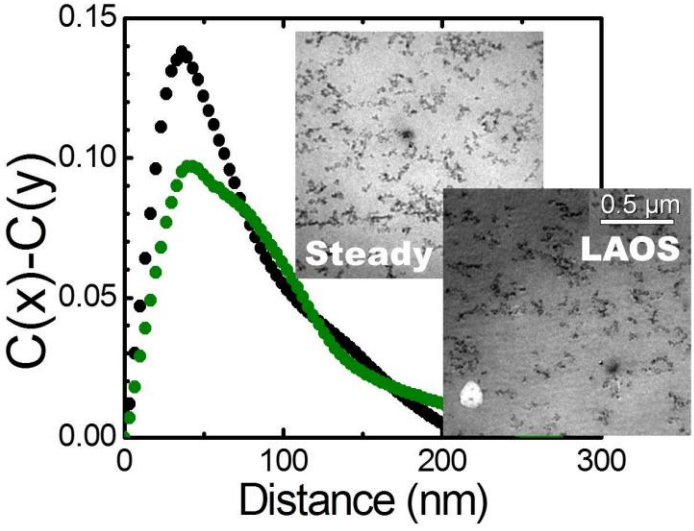

Figure 3.9 *Alignment comparison for a sample sheared in steady shear (black) and one in LAOS (green). There is no significant difference between the two samples. The horizontal and vertical directions are the flow and vorticity directions, respectively.*

3.7 Extensional Rheology

In extensional experiments, the primary consideration was the presence of both alignment and strain hardening (above and beyond that which would in any case have been observed for the pure polymer). As strong alignment had often been observed in shear flow, the expectation was for some degree of alignment in extensional flow, but it was not clear from the outset how the different flow would affect alignment. For example, extensional measurements on polypropylene/clay

nanocomposites have shown alignment of silicate layers perpendicular to the direction of extension[117]. To determine the extent of particle alignment with extensional flow, there are two relevant directions of possible alignment, parallel and perpendicular to the axis of elongation and these previous results make it unclear in which axis anisotropic assembled particle structures will align themselves in, if any. Therefore, after the samples were quenched they were prepared for TEM analysis to quantify alignment. This preparation was done but cutting the samples as shown in Figure 3.10. In this way, alignment could be checked in multiple directions.

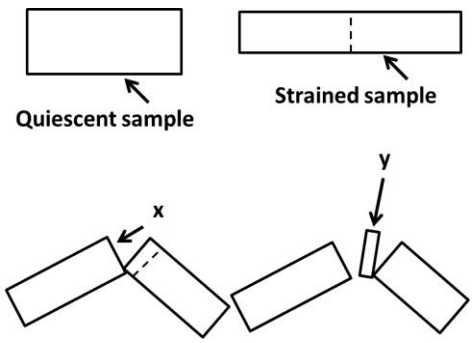

Figure 3.10 *The quiescent sample was strained as shown, and then cut in half. Images were taken both perpendicular (x) and parallel (y) to the axis of elongation.*

3.7.1 Alignment

In Figure 3.11 a sample of grafted SiO_2 particles in PS, from the connected region of the morphology diagram (see Figure 1.3), is considered. In this figure, there are TEMs for two shear histories. The first shear history was at a rate of 0.1 s^{-1} and taken to a strain of 2. Here the view parallel to the axis of elongation is shown in Figure 3.11a and the perpendicular view is shown in Figure 3.11b. The second shear history is at a rate of 1 s^{-1} and taken to a strain of 3. The view parallel to the axis of elongation is shown in Figure 3.11c and the perpendicular view is shown in Figure 3.11d. Because the applied strain is

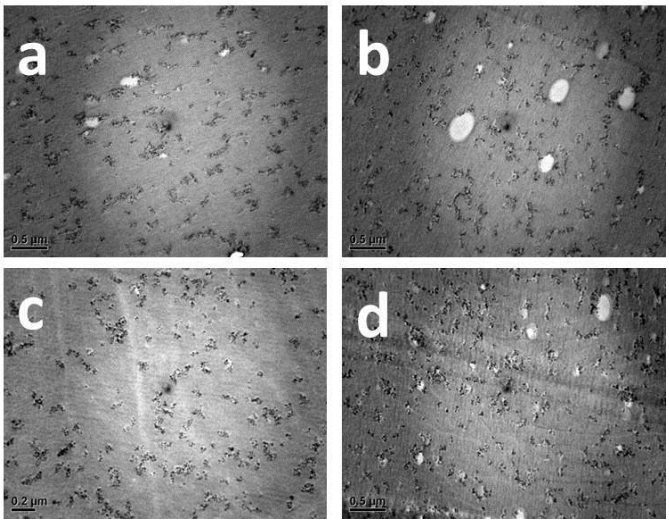

Figure 3.11 *TEMs of nanocomposite (5% by weight SiO_2, 79 kg/mol graft length, 0.05 ch/nm^2 graft density, and 214 kg/mol matrix length) under different elongation conditions. The images were taken on a sample at a rate of 0.1 s^{-1}, both parallel(a) and perpendicular(b) to the elongation, and at a rate of 1 s^{-1}, again parallel (c) and perpendicular (d) to the elongation.*

easier to visualize in a quenched elongational sample than in a quenched sample from steady shear (the shape of the sample changes with strain), in Figure 3.12, the quiescent sample and the two samples taken to the different strains are shown. While some degree of alignment is seen at the higher rate, it is apparent from the figure that the most alignment is visible at the low rate. This is consistent with what was discovered in steady shear experiments. Whether or not more alignment is seen when looking in the direction parallel or perpendicular to extension is not entirely clear. This would require more micrographs, and probably image analysis.

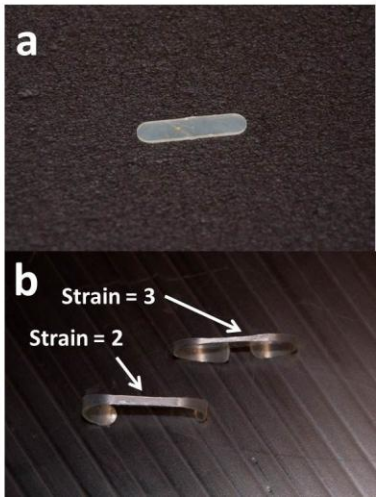

Figure 3.12 *Quiescent (a) and strained (b) geometry of quenched extensional samples.*

3.7.2 Strain Hardening

In this section the possibility of strain hardening (above and beyond what would be observed for a homopolymer) in extensional measurements is considered. Again, three different particle dispersion states are studied: spherical aggregates, connected structures, and particle strings. These dispersion states are obtained by mixing particles, again at 5% by weight of SiO_2, with 129 kg/mol homopolymer. The particles all have graft lengths of ~75 kg/mol, but at graft densities ranging from 0.01 ch/nm^2(aggregates), to 0.05 ch/nm^2(connected), to 0.1 ch/nm^2(strings). In addition, a sample in the connected region of our morphology diagram at a higher weight percent SiO_2 is compared (8%, 114kg/mol graft, 0.05 ch/ nm^2). Strain hardening is indicated by an elongational viscosity higher than that of the linear viscoelastic envelope. Since all of the matrices used are well above the entanglement molecular weight, in point of fact all of the samples will display strain hardening if the elongation rate is high enough. (Pure polymers exhibit strain hardening at elongation rates above the inverse Rouse stretch time, see Section 1.1.1). Thus if the nanoparticles are having an effect, this would manifest itself as strain hardening above and beyond that of the homopolymer at high rates or the emergence of strain

hardening at rates below the inverse Rouse time. The presence of strain hardening is dependent on the sample and the results can be seen in Figure 3.13 and are summarized in Table 3.2. Essentially, only the 8% sample shows strain hardening above and beyond what would be observed for the homopolymer, and this is the most dramatic when the measurement is taken at lower rates. However, the comparison is not direct, as the linear viscoelastic envelope is not necessarily the same for the nanocomposites and the homopolymer. Furthermore, Le Meins et al. [118] found that the addition of nanoparticles to polymer melts actually suppressed strain hardening. In their work, they used much larger particles and so the comparison is again not direct. Haraguchi et al. found an increase in strain hardening has also been found with polymer nanocomposites[119]. The potential strain hardening observed in the 8%

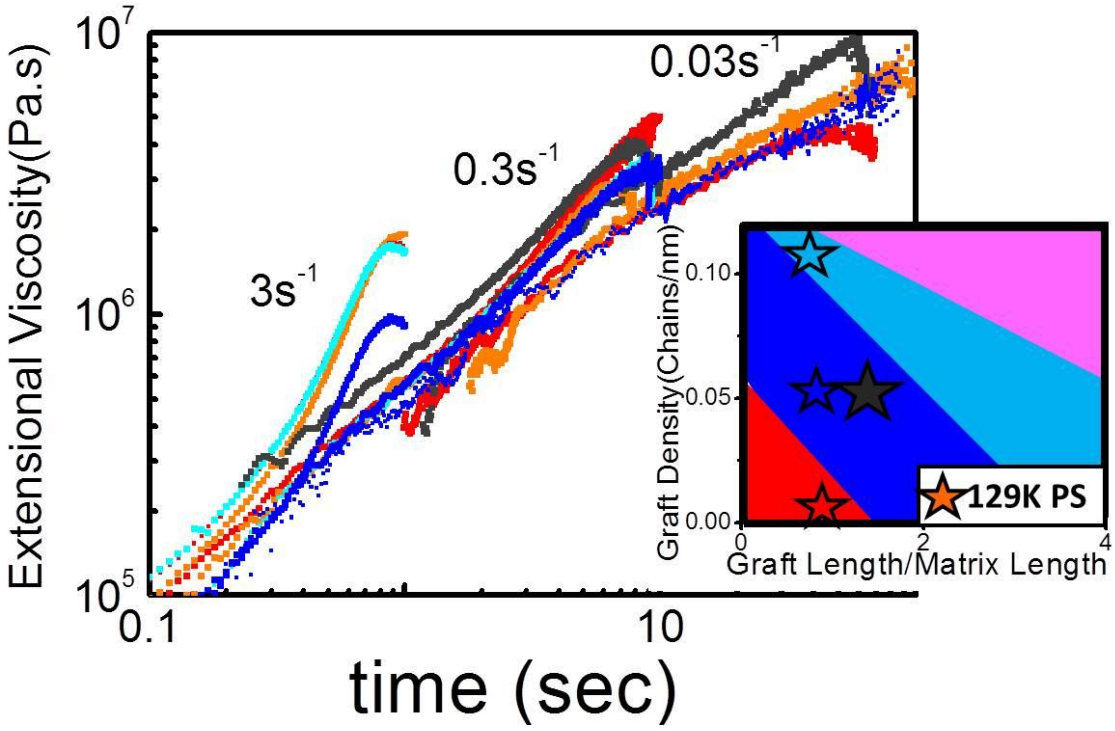

Figure 3.13 *Extensional viscosity as a function of time for five samples. All samples are in a 129 kg/mol homopolymer and the pure homopolymer measurements are included in the plot (orange). Three of the four broad regions of the morphology diagram are represented, strings (cyan, graft = 70 kg/mol, density = 0.11chains/nm^2, a connected structure (blue, graft = 79 kg/mol, density = 0.05 chains/nm^2) and spherical aggregates (red, graft = 78 kg/mol, density = 0.01 chains/nm^2). A sample from the connected region of the morphology diagram, at a higher loading of 8% is also shown (dark gray, graft = 114 kg/mol, graft density = 0.05 chains/nm^2).*

composite is consistent with many previous and current results from small amplitude oscillatory shear, where we see no effect of the particles except at low frequencies (low frequencies = long timescales = low shear rates). It is important that even in the case where we do see strain hardening for the 8% sample, it is at rates which are below where we expect to see strain hardening for a homopolymer. In homopolymers, strain hardening occurs at higher rates because the timescales involved are faster than the disentanglement time of the 'entangled network'. Thus here, potentially, we are seeing the effects of a particle network (which we know is present for the 8% sample). One additional 5% sample, in a higher molecular weight matrix, was also studied (not shown in the figure) and showed no strain hardening. It is not clear whether or not for the 5% samples, going to lower and lower rates of elongation would eventually lead to strain hardening or not. Indeed, this question needs further investigation.

Table 3.2 *Brush and matrix number-average molecular weights (M_n), polydispersities (PDI), brush graft densities, matrix solvent quality, morphologies and the presence of strain hardening in studied samples.*

Graft density (chains/nm^2)	Graft M_n (kg/mol)	Graft PDI	Matrix M_n (kg/mol)	Matrix PDI	Matrix Solvent Quality (α)	Morph-ology	Strain hardening?
0.01	78	1.3	129.2	1.03	0.60	aggregates	no
0.05	79.9	1.41	214	1.03	0.37	connected	no
0.05	79.9	1.41	129.2	1.03	0.62	connected	no
0.05, 8%	114	1.15	129.2	1.03	0.88	connected	yes?
0.11	70	1.1	129.2	1.03	0.54	strings	no

3.8 Conclusions

In conclusion, we have taken self-assembled anisotropic NP structures and by the use of well-defined steady shear flow fields grown the structures and aligned them in a favored direction. The alignment of these structures is maximized at the maximum in the stress response in a stress strain curve, and this is

confirmed using TEM in combination with image analysis and scattering. There is some evidence of alignment in extensional rheology, as well.

4. Entanglement of Grafts

In the preceding chapters, dispersion effects on polymer nanocomposite mechanical and flow properties were considered. PS grafted SiO_2 nanoparticles in a PS matrix self-assembled into a broad range of dispersion states, based upon the inherent dislike between PS and SiO_2. However, in the studied systems, it is difficult to vary the dispersion independently of the graft length and graft density of the chains. This is because these variables are fundamentally responsible for dispersion. Given a PS matrix molecular weight, it is possible to double the graft density and still achieve the same dispersion by decreasing the chain length. It is important to remember that the variation in properties between these similar dispersion states can be quite large (e.g. it was determined in Chapter 2 that mechanical properties are optimized when a connected network of particles exists *and* when the intermediate graft density of ~0.05 chains/nm^2 is chosen, for reasons that were explained in that chapter). Thus, it is important to determine how graft chains play a role in nanocomposite properties, independent of dispersion to the extent possible, and specifically focusing on graft entanglements (which have already been discussed somewhat in Section 2.3.3).

Entanglements of linear polymers are largely understood and were discussed in the introductory chapter. However, the graft chain entanglement behavior is expected to deviate from that of linear chains[120], and this is because the graft chains are tethered on one end. All of the grafted particles used in this chapter have graft lengths shorter than the matrix chain length and thus according to the discussion in Section 1.4, the matrix is a poor solvent for these grafts. Additionally, the graft densities are expected to be important as they will determine the configuration of the graft chain. There are three generally accepted regimes of configuration for grafted particles, a mushroom like configuration at low graft densities, a brush-like configuration at high densities in which the graft chains extend further outward from the surface and are entangled with each other, and a transition zone at intermediate

densities[121]. At the highest graft densities studied in this text (0.1 chains/nm^2) the graft chains just begin to enter this transition regime.

Limited work exists in the literature regarding entanglements of polymers grafted to particles in polymer melts, however the properties of entangelments of graft chains at a planar interface with elastomers[120, 122] and entangled melts [123] have been reported previously. In the latter case the effective friction was found to correlate to the flow rate, with slower flows leading to a higher value of friction.

In many ways, grafted particles are analogous to star polymers. Star polymers have varying numbers of chain arms all connected at a shared center[124] and entanglements in these systems are relatively well studied and follow the same tube model of entanglements[125] as linear polymers. Miros and Vlassopoulos studied star polymers diluted with linear chains and found that the entanglement molecular weight decreased with increasing volume fraction of star polymer[126]. However, the matrix polymer molecular weight was too small to be easily compared to the present study.

4.1 The Cone-Partitioned-Plate Setup and High Shear Rates

Here rheology is used to study entanglements of SiO_2 nanocomposites with PS grafted particles. In linear rheology, these entanglements manifest themselves in different ways. The primary evidence of them is the entanglement plateau. "This plateau is very similar to that exhibited by a cross-linked polymer, and it thus suggests the presence of an interaction between molecules that can simulate, over a certain range of frequencies, the effect of a rubber network." [12] However, for the samples studied at 5% by weight, the entanglement plateau only depended on the polymer molecular weight; the presence of the grafted particles had no significant affect. Another linear rheological phenomenon indicative of polymer entanglements is, for example, the abrupt change in the dependence of the viscosity on the molecular weight. The viscosity goes from being roughly proportional to the MW to

being proportional to the MW to the 3.4 power, and the critical weight at which this happens is at about twice the "average molecular weight spacing between entanglements."[127] However, it is difficult to use this to look at the entanglement in the grafted particles, as there are many different and competing factors which will also affect the viscosity.

Here non-linear measurements have the potential to provide new insights. However, in order to access information about polymer entanglements, one has to increase the shear rate to values high enough to correspond to the frequency where the entanglement plateau manifests itself in linear measurements. That is, if one considers pure PS at low shear rates, the rheology is relatively straightforward. The viscosity increases with shear and then reaches a plateau value. However, as the shear rate increases, the entanglements begin to exert influence on the rheology. Shear thinning occurs and there is a decrease in the steady state viscosity with increasing shear rate. Furthermore, a yielding process begins. An overshoot in viscosity is observed in the steady shear rate experiment, and this is similar to the overshoot that occurs for nanocomposites which emerges at much lower shear rates. The overshoot for linear polymers is traditionally related to "chain stretch" and "orientation of the chains in the flow field" [22]. Recently, Wang et al. have related this overshoot to the yielding of an entangled polymer network[128].

One major complication is that the use of high shear rates is fraught with experimental difficulties, primarily because of artifacts in the rheological data caused by phenomena such as edge fracture and shear banding. Of primary concern to the measurements herein is edge fracture. During edge fracture, the edges of the sample begin to fold inward or otherwise deviate from expected geometry, and the flows observed at the edge are not well-defined. Edge fracture initially only affects the outermost layer of the sample, but as an experiment progresses, these abnormal and poorly defined flows work their way inward, toward the center. However, since the edge of the sample is responsible

for the most torque in rotational measurements, from the very onset of edge fracture, the accuracy of rheological results is considerably undermined. Edge fracture will often manifest itself in a drop in the steady state viscosity in a start-up of steady shear experiment. In order to correct for this a special rheological set-up is used. This set-up is a cone and plate geometry with a partition ring (introduced in Section 1.1.1). In this set-up, there is a ring partition around the edge of the sample. This holds a buffer zone of sample in place, which is also being sheared, since the partition region is connected to the motor. However, because the partition is not connected to the transducer, no forces are measured from this region. The effect is to buy the measurement time. Even though edge fracture is occurring at the edge of the sample, since that portion is not being measured, the results are not affected. This can increase the experimentally accessible shear rates by an order of magnitude.

4.2 High Shear Rate Experiments

As explained previously, the presence of the cone-partitioned plate allows much higher shear rates than would otherwise be possible. This is because the buffer zone provided by the partition ring set-up delays the adverse effects of edge fracture (which invariably occurs at very high shear rates) until some reasonable length of time (which can generally be determined from the data). High shear rates can be directly related to high frequencies and short times in a small amplitude oscillatory shear experiment and a stress relaxation experiment respectively. Thus in these experiments we are probing the non-linear response, but in a completely different time regime than in all previous steady shear experiments. To understand this, it is probably easiest to consider the change in the steady shear behavior of unfilled linear polymer as the rate is increased. In our previous experiments we never went to a shear rate higher than 0.2 s^{-1}, and all PS homopolymers showed a viscosity or stress curve that rose up and plateaued with time. Although most of the composite samples would show a shear stress overshoot, this was never seen in the homopolymer samples. However, at higher rates, linear polymers do display an overshoot in viscosity in a steady shear experiment. In **Error! Reference source not**

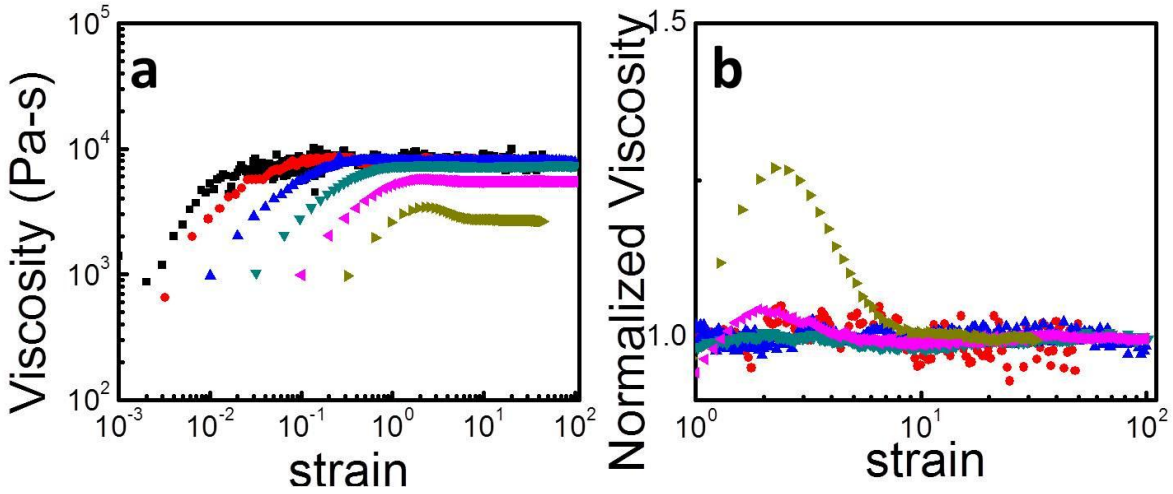

Figure 4.1 *The viscosity (a) and viscosity normalized using the high strain viscosity plateau (b) both as a function of strain. A cone partitioned plate geometry was used (to increase the maximum shear rate). The sample is a 129.2 kg/mol PS homopolymer. Six different shear rates were studied, 0.1(black), 0.32(red), 1(blue), 3.2(teal), 10(magenta) and 32 (dark yellow)* s^{-1}.

ound., both untreated and normalized steady shear results are shown for a 129 kg/mol, monodisperse PS. The normalized data are divided by the large strain, plateau viscosity, to emphasize the presence of an overshoot. A series of steady shear experiments are performed, one right after the other, with short rest times in between. The viscosity is shown instead of the shear stress in order to emphasize shear thinning, which commences at a rate of $3.2s^{-1}$. The first overshoot in the steady shear curve occurs at a shear rate of $10s^{-1}$. In our nanocomposite steady shear experiments, where we also see an overshoot, it had been rationalized by the yielding of a nanoparticle network upon shear. In the case of the homopolymer, there is of course no nanoparticle network, but the overshoot can be similarly rationalized as a result of a transient, 'entanglement network' the yielding of which we are able to probe at higher rates because the polymer does not have time to disentangle with response to shear.

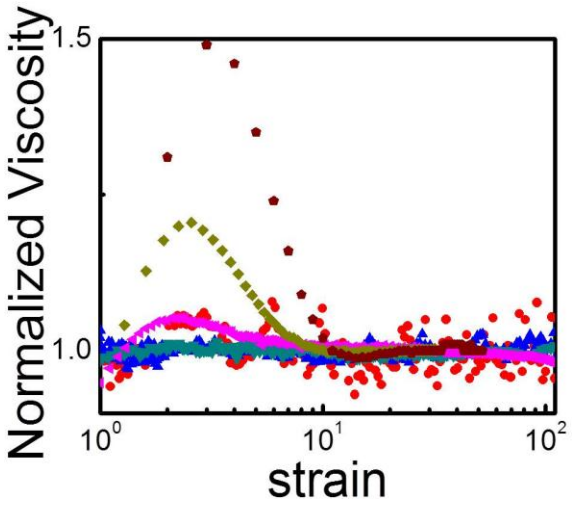

Figure 4.2 *The viscosity for a spherical aggregate structure (graft density = 0.01 chains/nm^2) normalized using the high strain viscosity plateau as a function of strain. A cone-partitioned plate geometry was used (to increase the maximum shear rate). The sample is in a 129.2 kg/mol PS homopolymer. Six different shear rates were studied, 0.32(red), 1(blue), 3.2(teal), 10(magenta) 32 (dark yellow) and 100 (dark red) s^{-1}.*

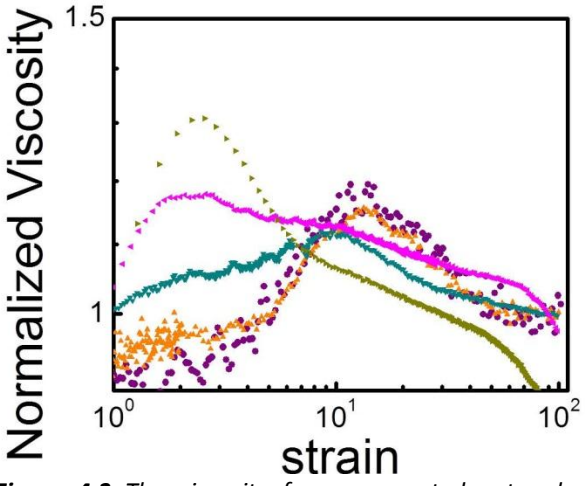

Figure 4.3 *The viscosity for a connected network sample (graft density = 0.05 chains/nm^2) normalized using the high strain viscosity plateau as a function of strain. A cone-partitioned plate geometry was used (to increase the maximum shear rate). The sample is in a 129.2 kg/mol PS homopolymer. Five different shear rates were studied, 0.2(purple), 0.63(gold), 3.2(teal), 10(magenta) and 32 (dark yellow).*

Since, in a similar fashion to the pure polymer, there was an absence of an overshoot in the case of many of the nanocomposites with a dispersion state of small spherical aggregates, the rheological response of such a composite was also tested at much higher rates. A sample with a 78 kg/mol graft, 129.2 kg/mol matrix, and 0.01 chains/nm^2 graft density was sheared to see at which rate the onset of yielding occurs. The results (Figure 4.) show that this aggregate sample essentially mimics what is seen for the homopolymer (suggesting a negligible effect of the particles).

Perhaps more interesting is what is seen when we increase the shear rate for our composite samples that have a clearly defined particle response in steady shear (as manifested in a viscosity overshoot at low rates). We turn first to a sample from the connected region of our morphology diagram (75 kg/mol graft, 129 kg/mol matrix, 0.05 ch/nm^2). In Figure 4., we see that such a sample has an overshoot at all shear rates. If we look at the magnitude of the normalized overshoot, we

see something even more interesting. At low rates the normalized overshoot peaks at a high value and then shrinks as the rate is decreased, such that at a rate of 3.2 s^{-1} the normalized peak is a lower value than it is at a rate of 0.2 s^{-1}. However, as we increase the rate further the normalized peak again seems to increase and now its magnitude is roughly in line with what was observed for both the homopolymer and the aggregate sample. An even more obvious feature of the figure is the dramatic shift in the strain of the overshoot as the rate is increased. As stated previously, all prior experiments were done at much lower rates. At these low rates, we typically saw an overshoot in the stress or the viscosity that occurred at strains between 5 and 15 (this is sample dependent, and specifically seems to be correlated with the grafted chain length in the samples, as discussed in Section 2.3.3). At low rates, this overshoot strain was independent of rate. Meanwhile, for the homopolymer sample and the aggregate dispersion state, which manifest an overshoot only at high rates starting at around 10 s^{-1}, and it always occurs at a strain between 2 and 3. With the 'connected' composite in figure 2, we see an overshoot at high strains at low rates, consistent with the previous low rate steady shear experiments, and we see an overshoot at low strains at high rates, consistent with the high shear rate data for the homopolymer and 'aggregate' dispersion state. Thus we can postulate that there are two yielding mechanisms and that the yielding that occurs depends on the shear rate. At high shear rates, we see polymer network yielding (it is unclear here whether that yielding is solely from the matrix or from the matrix and the polymer graft). At low shear rates, we see particle network yielding (and here it is unclear whether the yielding is from the particle core interactions or the graft interactions).

We now turn to the third dispersion state, the 'strings' state in our morphology diagram. Here we see something similar to what was observed with the 'connected' dispersion state. Namely, at the lowest rate, we see a high strain overshoot and at higher rates we see a low strain overshoot (postulated to be representative of particle yielding and polymer yielding respectively). However, the difference is the polymer yielding mechanism seems to start at even lower rates. At a rate of only 1 s^{-1} we already see an overshoot between a strain of 2 and 3 (Figure 4.). Recall this overshoot does not start until a rate of 10 s^{-1} for the homopolymer and 'aggregate dispersion state. Thus here we see polymer yielding at an order of magnitude of lower rates. To quantify all these results and present them in a way that is easier to visualize, in Figure 4.5 we plot the strain of the overshoot for all samples studied (including an additional, 5% sample with a connected structure) as well as the magnitude of the normalized overshoot. The relevant experimental details are plotted in Table 4.1. In Figure 4. all samples have overshoots that drop to very low strains (~2-3) at shear rates at or above 10 s^{-1}, with the sample in the 'strings' region of the morphology diagram having a much less abrupt drop towards this low strain yielding than the other samples. This sample also has a normalized overshoot peak that is much higher than for most other samples especially at the highest shear rate. This sample has many additional graft chains as compared to the other sample and apparently this causes the particles to act less like particles and more like non-linear polymer (i.e. star polymers), and therefore primarily work to enhance the entanglements experienced by the matrix polymer.

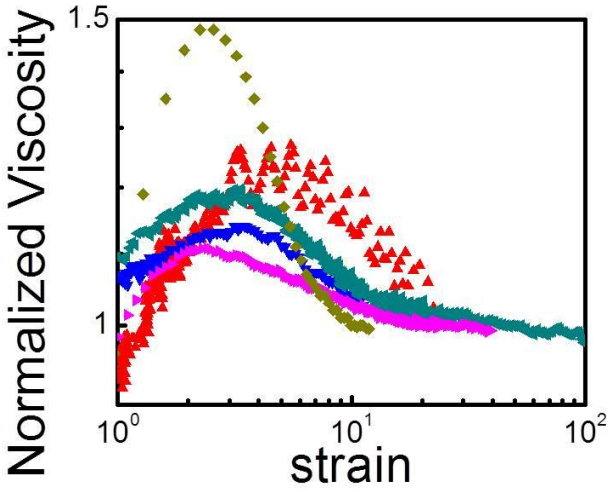

Figure 4.4 *The viscosity for a string structure (graft density = 0.11 chains/nm^2) normalized using the high strain viscosity plateau as a function of strain. A cone-partitioned plate geometry was used (to increase the maximum shear rate). The sample is in a 129.2 kg/mol PS homopolymer. Five different shear rates were studied, 0.32(red), 1(blue), 3.2(teal), 10(magenta) and 32 (dark yellow).*

Table 4.1 *Brush and matrix number-average molecular weights (M_n), polydispersities (PDI), brush graft densities, matrix solvent quality, morphologies and the shear rate at which overshoot is first observed for studied samples.*

Graft density (chains/nm^2)	Graft M_n (kg/mol)	Graft PDI	Matrix M_n (kg/mol)	Matrix PDI	Matrix Solvent Quality (α)	Morphology	Rate onset of overshoot (s^{-1})
N/A	N/A	N/A	129.2	1.03	N/A	homopolymer	10
0.01	78	1.3	129.2	1.03	0.60	aggregates	10
0.05	52	1.07	129.2	1.03	0.40	connected	<0.32
0.05	75	1.06	129.2	1.03	0.58	connected	<0.2
0.11	70	1.1	129.2	1.03	0.54	strings	<0.1

Because these steady shear experiments have the ability to significantly change the sample, it is important to note that some of them were done consecutively, on the same molded sample. This was done with the 129 kg/mol homopolymer and the aggregate sample and repeated experiments at the same shear rate showed the same results. For the higher graft density samples, sometimes fresh samples were used and sometimes repeated measurements were taken on the same sample but the trends observed in the strain were not affected. Thus while the results are generally trustworthy, repetition on fresh samples in all cases is probably necessary.

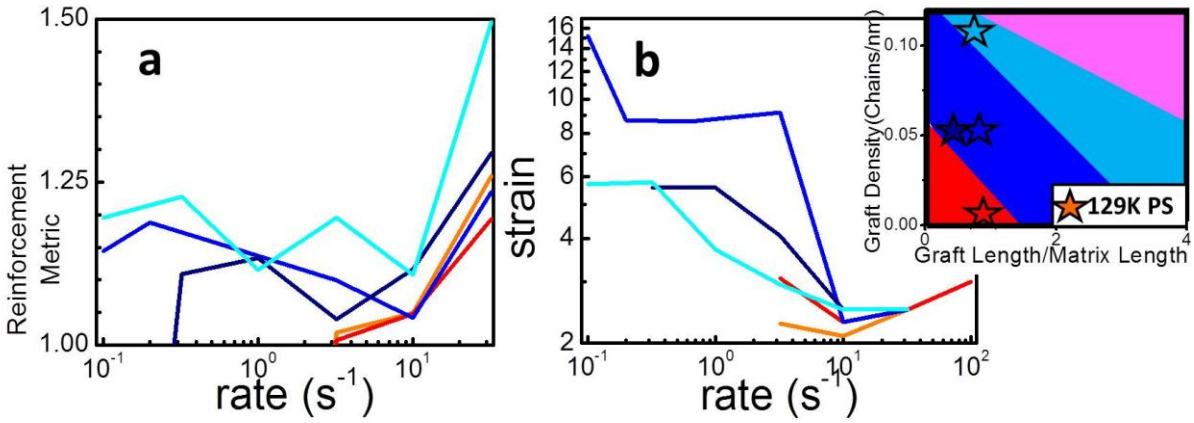

Figure 4.5 *Reinforcement metric first presented in Section 2.3.2 as function of shear rate for four nanocomposites and a homopolymer(a) Strain of overshoot for the same samples (relevant information in Table 4.1) again as a function of shear rate (b). The inset shows the location of the samples in the experimental morphology diagram.*

4.3 Stress Relaxation after Steady Shear

Next we turn to the stress relaxation that was allowed to happen after most of the steady shear experiments, to determine how much nanoparticle structure remained. These experiments were done, as stated, to observe what degree of structure was still present after shear. We first consider the case of an 8% sample (the same sample used throughout this text). This composite was sheared to a strain of 7 (at the peak of the overshoot) and using a separate, fresh sample, to a strain of 100 (well past the peak and into the stress plateau region). In each case, the stress was then allowed to relax. These results can be seen in Figure 4.6. The 8% sample comes from the connected/sheet region of our morphology diagram. We note that the stress relaxes more slowly for the cessation of shear at the lower value. This lends more credence to the conclusion that the overshoot represents a yielding process that breaks down structure. This is further confirmed by the fact that small amplitude oscillatory shear experiments done before and after shear display a decrease in the low frequency G' for most samples, including the 8% sample shown in Figure 4. (for the limited number of 5% samples where this decrease does not occur, it is not necessarily because the sample did not lose structure after shear, but more likely that the recovery was too quick to be probed with a SAOS experiment). To quantify the speed of storage modulus recovery after shear and determine how much the 'devastation' caused depends on shear rate, we next consider

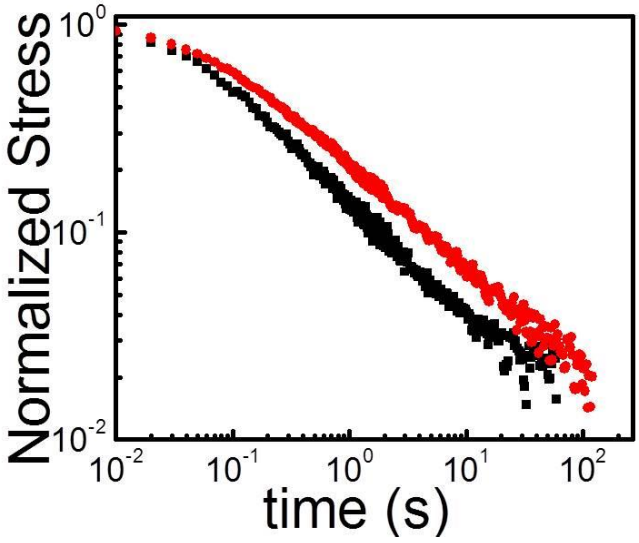

Figure 4.6 *Relaxation of the normalized stress after steady shear for an 8% composite taken to a strain at stress max (strain = 7, red data points) and a strain well past the stress max (strain = 100, black data points). The graft density is 0.05 chains/nm^2, and the graft length is 114 kg/mol. The matrix polymer is 129.2 kg/mol.*

Figure 4.7. Here we again focus on the 8% nanocomposite sample in the connected/sheet region, as this sample has a nanoparticle network measureable using the storage modulus. In Figure 4.7 we show the low frequency G' recovery of this sample after three separate rates (4.7a) and the recoverability of the steady shear response after a long wait time (4.7b). Even after very long wait times, the structure is not fully recoverable. Furthermore, the structural breakdown with shear seems to be more dramatic and less recoverable at higher shear rates. The experimental results from Figure 4.7a involved incredibly long experimentation times and therefore in some cases because of limited nitrogen gas (which is necessary for high temperature experiments, to limit polymer degredation), it was not possible to carry the experiments on for as long of times as would have been desired.

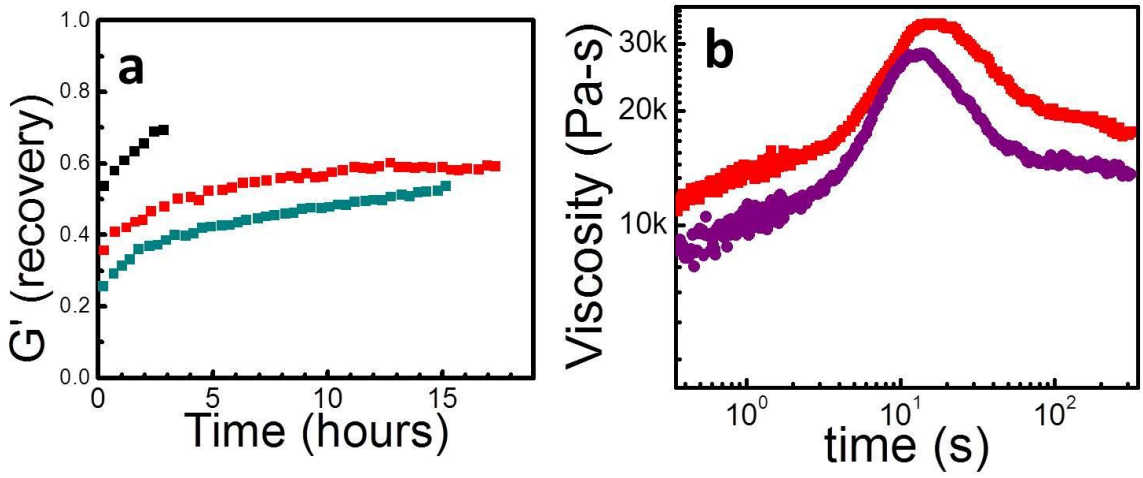

Figure 4.7 *Recovery after shear of the storage modulus for the same composite as in Figure 4.6. Three different shear rates are considered in (a), 0.1 (black), 0.32 (red), and 3.2 s^{-1} (teal). Steady shear viscosity vs. time data before and after recovery at a rate of 0.32 s^{-1} is also considered in (b). The red data is on a quiescent sample and the purple data is on the sample that slowly recovered (at 180 degrees C) in the rheometer for 18 hours.*

We also did many stress relaxation experiments after steady shear for 5% samples and specifically, for the homopolymer and three representative composites (aggregates, a connected network, and strings). These experiments were performed at a range of shear rates and the results are presented in Figure 4.8. Generally, we see that the connected/sheet morphology has stress that persists

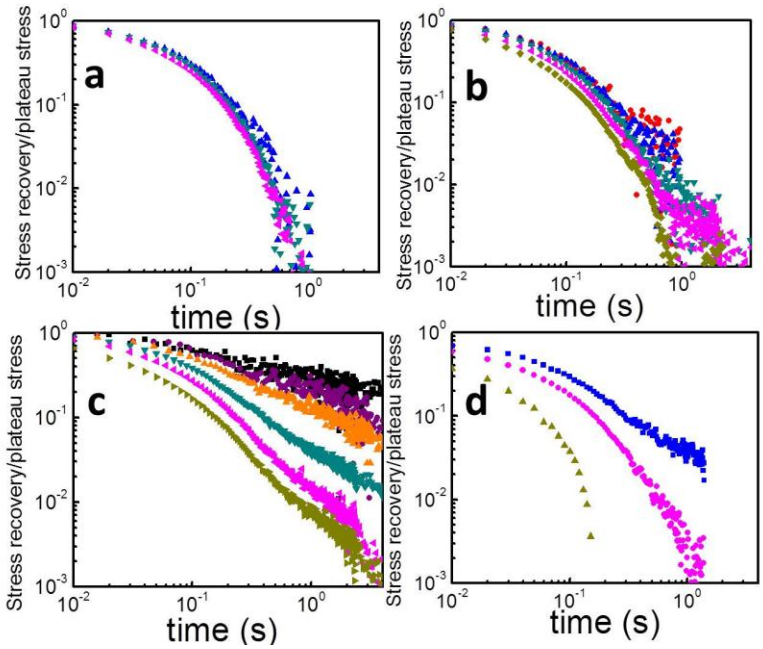

Figure 4.8 *Stress relaxation after steady shear for a 129 kg/mol homopolymer (a) and 5% by weight composites with a 129 kg/mol homopolymer and three different particles: 78 kg/mol graft, 0.01 chains/nm^2, aggregate dispersion state (b), 75kg/mol graft, 0.05 chains/nm^2, connected structure dispersion state (c) and 70 kg/mol graft, 0.11 chains/nm^2, string dispersion state (d). Several rates are considered: 0.1 (black), 0.2 (purple), 0.32 (red), 0.6 (gold), 1 (blue), 3.2 (teal), 10 (magenta) and 32 s^{-1} (dark yellow).*

for the longest time after cessation of shear. However to probe these results more deeply, the following analysis was done: we took the recovery of the composite samples and divided out the recovery of the homopolymer in order to see how much additional structure there was from the particles. These results proved fruitful, and are displayed in Figure 4.9. They have been categorized by rate, to show which sample has the most residual structure at a given rate. While the aggregate samples residual structure as compared to the homopolymer does not seem to depend strongly on rate, the connected structure and the string structure both decrease with increasing rate. This is consistent with the results presented in Figure 4.7, where for an 8% composite the 'devastation' in structure was greatest at the highest rate. In the case of the high graft density or 'string' structure this increase is the most dramatic, such that at the highest shear rate, the stress relaxation curve shows evidence of less structure than was even observed in the homopolymer. The total significance of this result is not clear, but it fits with the previous results that show at high rates, this sample higher grafting density sample is an exception. Clearly, the large number of graft chains in this composite has a significant effect which can be probably be related to additional entanglements.

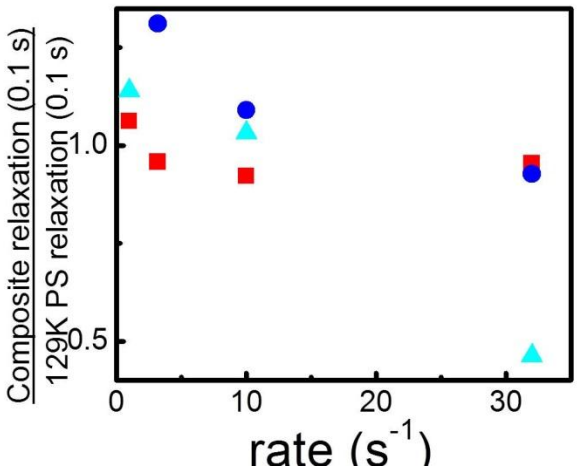

Figure 4.9 *Stress relaxation of composite divided by stress relaxation of homopolymer at a time of 0.1 s.*

5. The Polymer Bound Layer in Bare Particles

Although it has long been understood that nanoparticles are more effective at reinforcement of polymeric materials than micron sized particles, limitations in particle synthesis have, until recently, limited the ability of researchers to investigate this effect at very small sizes. Consider that solvent molecules, which have typical sizes of less than a nanometer, are observed to plasticize polymeric materials, weakening their mechanical properties. If these molecules are treated as the analogue of sub-nanometer particles, it is entirely reasonable to conclude that traditional fillers, when reduced to this size range, will also prove detrimental to material mechanical properties. Indeed, this has been seen for 2nm diameter particles[7]. In such a case the radius of gyration of the polymer begins to be much larger than the particle diameter, and this might be responsible for the observed behavior.

While many groups have demonstrated a difference in bound polymer for nanoparticles vs. a flat surface, the magnitude of this effect as a function of size is as yet unclear. It is clear there is an effect of size on 'bound layer' thickness but it is important to place this effect in context. That is, at what particle size does this behavior onset? Furthermore, how quickly does the bound layer move from the full thickness observed at a flat surface to a layer of ~$1/5^{th}$ that thickness at 14nm, and potentially to the complete absence of a bound layer at some finite nanoparticle size? How do annealing, polymer molecular weight, and nanoparticle weight fraction affect the total 'bound layer'. In this chapter, an attempt is made to address these questions for bare particle systems

5.1 Bound Polymer Thickness in Attractive Polymer Particle Systems: Differential Scanning Calorimetry

The Kumar group had previously studied a system of P2VP and SiO_2 nanocomposites and observed many interesting characteristics, including a much smaller T_g shift than expected base on the attractive polymer-particle interaction[74]. The T_g in this experimental system was studied using

differential scanning calorimetry (DSC) and the same data was used to determine a bound layer thickness of 1.4nm (±0.3nm). These results were obtained for 14nm particles. In order to better understand bound layer thickness in attractive polymer-particle systems, two additional polymers were chosen for a similar DSC study here. Poly(methyl methacrylate) (PMMA) and poly (ethyl methacrylate) (PEMA) both also have strong hydrogen bonding interactions with 14nm particles which facilitate miscibility. Dispersion was tested for these systems using TEM and was found to be uniformly good. Using DSC, the T_g was also determined for all these composites and it was determined that it does show a dependence on nanoparticle loading, but the magnitude of the shifts is less than 10 K for all nanoparticle loadings. These results agree with the picture that there are negligible shifts in glass transition temperature on confinement. Here we focus on the bound layer thickness determined by the same DSC measurements.

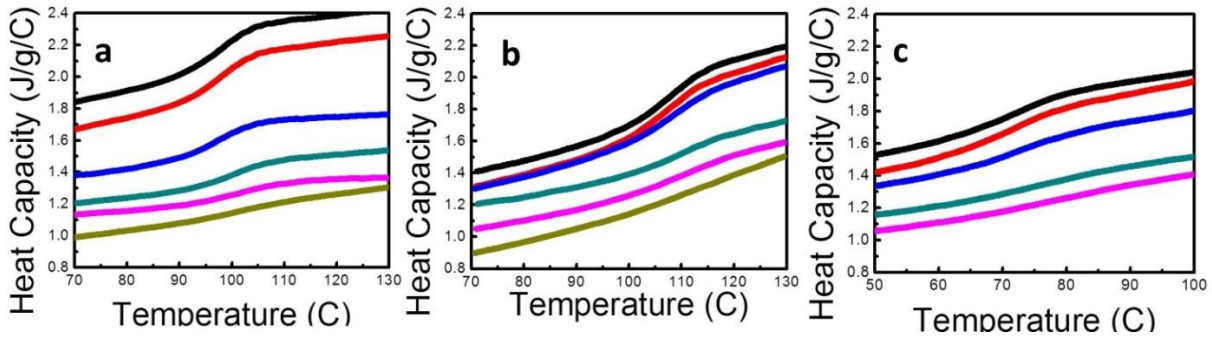

Figure 5.1 *DSC as a function of 14nm SiO_2 particle loading for three different homopolymers, P2VP (a), PMMA (b), and PEMA (c). The homopolymer (black), 1% (red), 20% (blue), 40% (teal), 50% (magenta), and 63% (dark yellow) loadings by weight were studied. Slight increases in T_g as a function of nanoparticle loading are evident.*

Figure 5.1 shows the DSC data for the three mixtures of polymer and particle at weight fractions ranging from 0.01 to 0.63. The slight shift in T_g that was mentioned in the previous paragraph is apparent in the three different systems. In Figure 5.2, we perform an analysis of this data to determine the bound layer thickness. Note that the strength of the DSC transition in Figure 5.2 (i.e., ΔCp) decreases linearly with increasing SiO_2 content, but the slope of the line is larger than unity. This suggests that the heat capacity goes to zero for finite polymer concentration. This implies that there is a

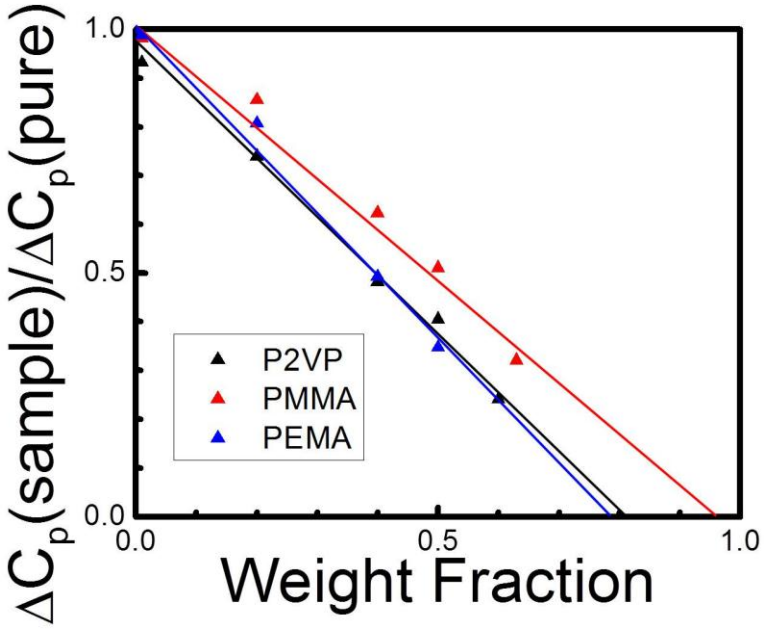

Figure 5.2 *ΔC_p scaled by the value for the pure polymer plotted as a function of the volume fraction of silica. The plot should scale linearly if there is no bound layer and go to zero for 100% of SiO_2.*

bound layer of polymer on each particle, and we estimate based on the slopes of the lines that the thicknesses are 0.8 nm, to within relatively large error bars (±0.6 nm). From this we consider a picture that is inspired by our previous work on the phase transitions in thin polymer films [129, 130]. In the presence of strong polymer−surface interactions it is now well accepted that a "bound", essentially irreversibly adsorbed, polymer layer forms at the particle interface. Because of the essentially irreversible nature of polymer adsorption, this bound layer is dynamically decoupled from the "free" polymer on top of it; i.e. the free polymer has essentially no interactions with the attractive surface. We postulate that the bound layer does not relax in the time frame of our DSC experiments, and hence only the bulk of the sample (i.e., the free chains) shows a glass-like relaxation. Since this layer is unaffected by the surface it essentially has the same T_g as the bulk polymer. Additional credence for this assessment is provided by recent experiments on PS spheres[131] and for PMMA− SiO_2 composites[75] where the heat capacity change in traversing the glass transition region was found to decrease monotonically with increasing surface content. In fact, this reduction in ΔCp on confinement has previously been used to determine the effective thickness of the bound polymer layer, giving more credence to this picture.

5.2 Various Silica Particle Sizes in Poly (2-vinyl pyridine)

As the DSC measurements discussed in Section 5.1 contained large error bars, and were only for a particle size of 14nm, a more in depth analysis was pursued for the composite consisting of P2VP and SiO_2. We study this system of SiO_2 nanoparticles in poly (2-vinyl)pyridine (P2VP) in more depth to fully explore potential causes of the observed maxima in mechanical reinforcement. We focus on this system because, as we have demonstrated previously, the favorable interaction between the P2VP and the SiO_2 surface will allow the particles to randomly disperse themselves throughout the polymer, thus removing dispersion as a variable. This was confirmed with transmission electron microscopy (TEM), ultra small angle x-ray scattering (USAXS) and small angle x-ray scattering(SAXS)[74]. In this work we have taken TEMs of all studied samples, to confirm uniform dispersion. In Figure 5.3 we show representative TEMs of the four particle sizes at 30 weight percent of SiO_2. Uniform dispersion is especially important when calculating the total 'bound layer' thickness from the thermogravimetric analysis (TGA) results, as a well-defined geometry is necessary for accurate calculations. Good dispersion will allow for full bound layer formation at low enough loadings and creates a well-defined dispersion state, allowing comparison of different particle sizes.

Additionally, the favorable polymer-particle interaction will allow the polymers to form an adsorbed or bound layer on the particle surface and our previous evidence has supported the necessity of attached polymer chains to mediate mechanical reinforcement[116].

The experimental system chosen is SiO_2 nanoparticles (from ~14-100 nm in diameter) in P2VP (2-940 kg/mol). Our motivation for choosing this system is that the favorable interaction between the SiO_2 and the P2VP, as mentioned previously, should allow a truly random dispersion of the SiO_2 particles in the polymer matrix. Furthermore, Nissan Chemicals provides complimentary samples of several different SiO_2 nanoparticle sizes. The ability to use many nanoparticle sizes all from the same manufacturer is important, because here we have aimed specifically to measure the 'bound layer'

thickness as a function of nanoparticle size, ignoring variables such as type or shape of NP. We want to compare the magnitude of the change in 'bound layer' thickness with size to the opposing phenomena

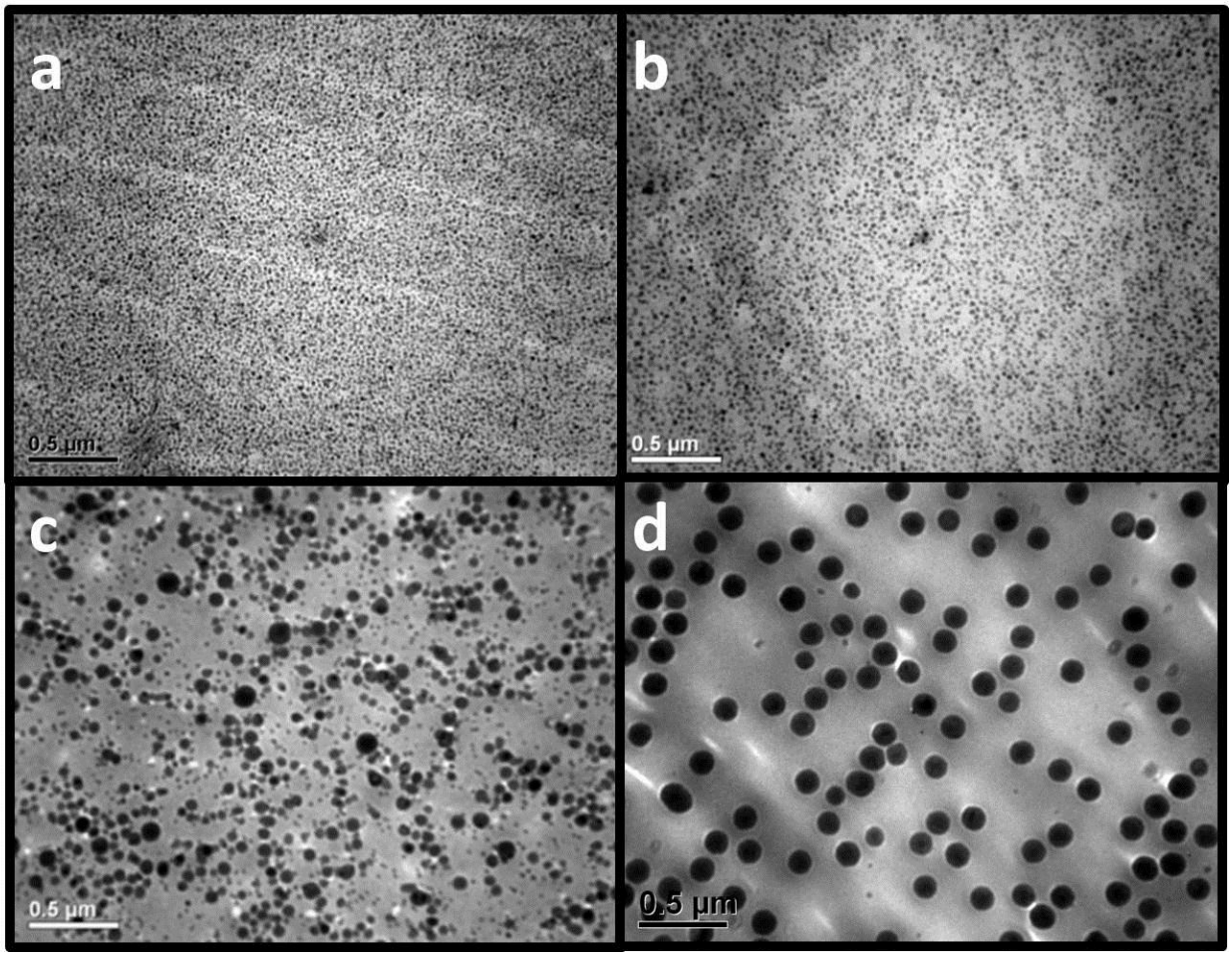

Figure 5.3 *TEMs confirming excellent dispersion for four different sizes of particles from Nissan chemicals, small particles ~14nm in diameter (a), medium particles ~22nm in diameter (b), large particles ~70-85nm in diameter (c) and extra large particles ~110 nm in diameter (d).*

which improve particle properties as nanoparticle size decreases (including the favorable change in surface area to volume ratio as particle size decreases).

5.3 Thermogravimetric Analysis Experiment Design

The silica nanoparticles were generously donated by Nissan Chemicals and come dispersed in one of two solvents, both at 30-31 weight percent SiO_2: methyl ethyl ketone (MEK) or isopropyl alcohol

(IPA). The particles come in one of four sizes as reported by Nissan: 10-15nm, 17-23nm, 40-50nm, and 70-100nm (these will be referred to as small(S), medium(M), large(L) and extra large(XL) respectively from here on). The particle sizes that are used in calculations are different than those reported by the manufacturer, as will be discussed further on. The S and L particles come in MEK and the M, L, and XL particles come in IPA (thus the L particles come in two different solvents). In order to create precise measurements of the bound layer thickness, a well-defined nanoparticle geometry is necessary. The size is reported by Nissan as a range, but an average size is required for bound layer thickness calculations. Therefore, a large number of TEM images were taken of the particles, and the diameters of several hundred particles were measured using Image J software. This analysis was compared to similar measurements taken using a DLS and the results are reported in Figure 5.4 and Table 5.1.

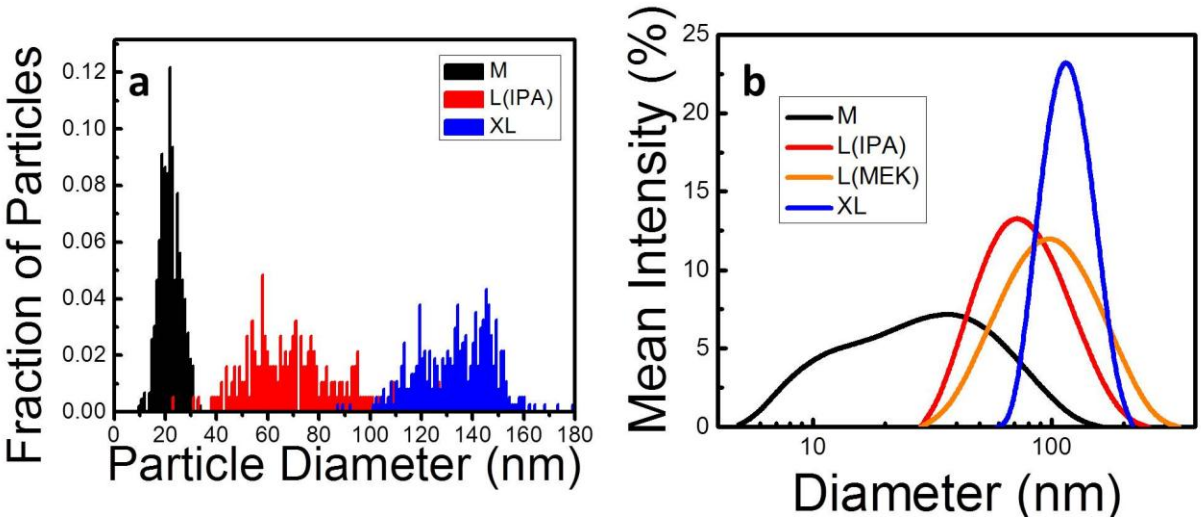

Figure 5.4 *Particle size distribution for the three larger Nissan particles as taken by image analysis of TEM micrographs (a) and using a DLS on 1% solutions of the particles (0.1% in the case of the XL particles) (b). The S particles were taken to be of size 14nm, which has been well reported in the literature.*

Table 5.1 *Calculated Particle Sizes*

Particles:	**M**	**L(IPA)**	**L(MEK)**	**XL**
Nissan distribution (nm)	17-23	40-50		70-100
TEM Average diameter (nm)	22.5	70.9	56.0	134
DLS Average Diameter (nm)	22.2	70.5	87.4	114

The P2VP is purchased from *Polymer Source Inc.*and has number average molecular weights of 2.1, 5, 14, 22, 50, 97, 277, and 854 kg/mol with P.D.I. of 1.14, 1.07, 1.05, 1.09, 1.04, 1.08, 1.09 and 1.10 respectively. Unless otherwise noted, the 50kg/mol P2VP is used. Particle solutions in MEK are prepared by adding 1 mL pyridine to 4 mL of the particle solution as manufactured. Particle solutions in IPA must be further diluted to prevent gel formation by combining 2 mL of the particle solution as manufactured with 10 mL of IPA and 3 mL of pyridine (in that order). The pyridine is added in a 4:1 ratio of particles to pyridine in order to improve particle dispersion through charge stabilization (pyridine acts as a Lewis base) and through competitive hydrogen bonding of the pyridine to the SiO_2 surface. This prevents premature cross-linking of the SiO_2, which will lead to particle agglomeration and precipitation[74]. Various ratios of pyridine to solvent were tested and 4:1 was determined to be optimal. For each nanocomposite to be prepared, 0.2 g of P2VP is dissolved in 4 mL of solvent, either MEK or IPA depending on which solution the particles are provided in. These prepared solutions are vortexed for 1 hour. The concentration of each solution is then measured by pipetting 100 µL onto a tarred weighing paper, allowing the solvent to fully evaporate, and using the observed weight to calculate concentration. Based on the measured concentrations, appropriate volumes of both the particle solution and the polymer solution are combined such that 30% of the combined mass is SiO_2 and 70% is P2VP, except in the case of the M particles, where 40% SiO_2 is used to promote full pellet formation. This combined solution of both particles and P2VP is again vortexed overnight, followed by one minute of sonication (2s sonicate, 1s rest). It is then poured into a teflon coated petri dish and left in the fume hood to dry.

After drying, a small section of the sample is selected to confirm the particle dispersion state using electron microscopy. The section is embedded in epoxy and cured at 80˚C for 8 hours. It is then microtomed using a Leica UCT microtome into 60nm sections and placed on a Formvar coated copper TEM grid. These sections are visualized using a JEOL JEM-100 CX transmission electron microscope.

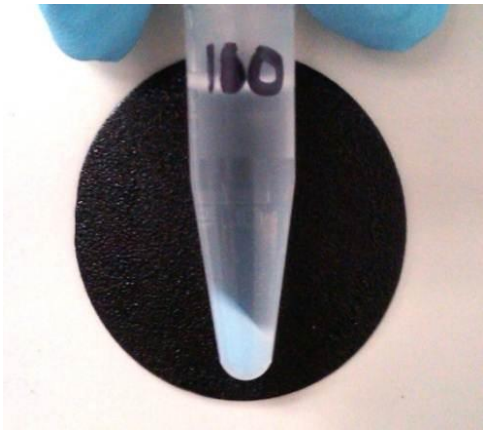

Figure 5.5 *Pellet formed after centrifugation of a redissolved composite, in this case, a 100nm, 50kg/mol P2VP composite.*

To determine the bound layer thickness, the remainder of the sample is again dissolved in its respective solvent, either MEK or IPA. If the sample is to be annealed, then it is placed in an oven under vacuum at 150˚C before dissolving. This dissolved sample is vortexed overnight and then centrifuged at 13,000 rpm for 5 minutes. The particles form a pellet at the bottom of the centrifuge tube, and any bound P2VP is incorporated into the pellet as well. The unbound P2VP remains in the supernatant. A fully formed pellet from a 100nm sample is shown in Figure 5.5. This

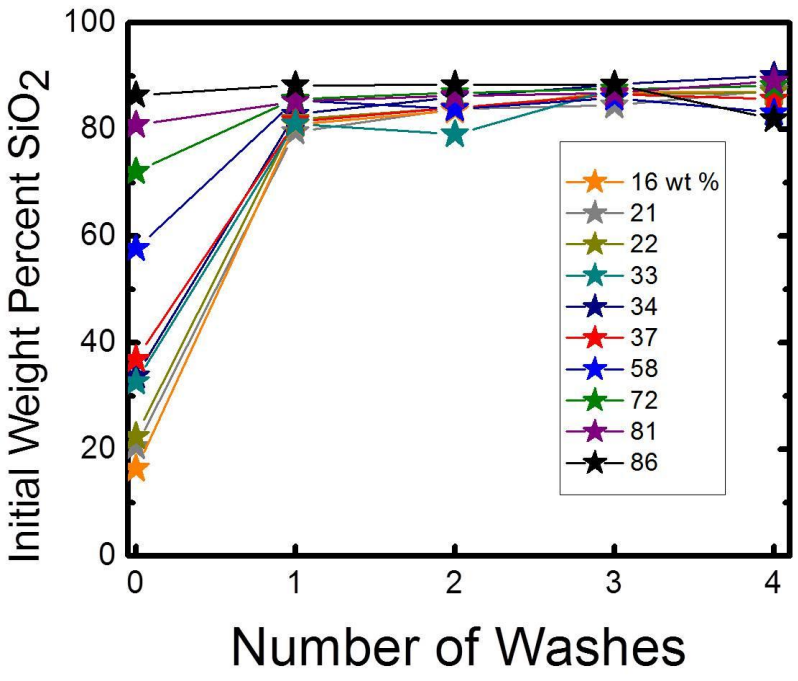

Figure 5.6 *Weight Percent SiO_2 as a function of the initial loading, and number of washes, of the nanocomposite. The bound layer achieved is largely independent of initial loading, up to a loading of 86% by weight.*

washing process is repeated, to ensure removal of all unbound P2VP. (It was experimentally determined that two washes is sufficient after observing a convergence of the bound layer thicknesses at two washes of samples that were washed between one and five times (Figure 5.6). (This was done for nanocomposites with particle weight fractions ranging from 16-86%). The resulting pellets are completely dried first in the fume hood overnight, then at 80˚C under vacuum. Finally, the pellets are each burned in a thermogravimetric analyzer (TGA) in a heating sequence as follows: an isotherm at 30.0˚C for 2.0 minutes, followed by a temperature ramp from 30 to 150˚C at 20.0˚C/min, then an isotherm at 150.0˚C for 10.0 minutes (to confirm the absence of solvent), and finally a temperature ramp from 150.0 to 1000.0˚C at 10.0˚C/min where the P2VP is expected to burn off at around 450˚C. The SiO_2 does not burn off. Assuming that each particle and any bounded polymer conforms to a perfectly spherical geometry, and using weight fraction of P2VP in the pellet as determined by TGA, the bound layer thickness is calculated. Since we do not know the exact density of the bound P2VP, we assume the same density as the bulk to calculate thickness.

Table 5.2 *Nanoparticle Coating Information*

Particle Size (nm)	**Solvent**	**Thickness of Coating (nm)**	**Fraction of ParticleThat is Coating**
Small	MEK	0.12 ± 0.03	0.022 ± 0.005
Medium	IPA	0.06 ± 0.01	0.008 ± 0.001
Large	MEK	0.27 ± 0.02	0.0104 ± 0.0008
Large	IPA	0.208 ± 0.03	0.008 ± 0.001
Extra Large	IPA	0.5055 ± 0.1	0.010 ± 0.002

Note that the particles are manufactured with a coating that prevents agglomeration. This coating may at least partially burn off during the TGA run. Since the Nissan particles are proprietary,

information about the coating is not readily available. Therefore samples of pure particles of each size were burned to determine what fraction of the particle is coating. Similarly, to account for the small amount of P2VP that does not burn off, TGA runs were performed on pure P2VP. The results were different for each particle size and solvent and are shown in Table 2. The fraction of the particle that is coating is directly used in every bound layer thickness calculation.

5.4 Nanocomposite Characterization

In order to provide a strong foundation for measurements of the polymer 'bound layer' all nanocomposites were meticulously characterized. This included a thorough analysis of the dispersion state of the nanoparticles, as a well-defined dispersion state is paramount if the 'bound layer' calculations are to have any meaning. Furthermore, nanoparticle size must be precisely measured, as this significantly affects the 'bound layer' calculations.

5.4.1 Nanoparticle Dispersion

We first consider the dispersion achieved using the preparation techniques outlined in the experimental section. Figure 5.7 demonstrates the excellent dispersion shown for nanocomposites, independent of particle size and loading fraction as is consistent with previous work in the Kumar group. Although most of the samples studied using TGA were at 30 weight percent, particles are shown at many different weight fractions, as it can be difficult to observe dispersion quality with the naked eye at loadings as high as 30 percent. Good dispersion is paramount , as this allows for an accurate calculation of the bound layer thickness. For all samples studied, micrographs were taken to confirm good dispersion. In some of the micrographs in Figure 5.7, strings of particles were observed, and thus a computer analysis was performed to confirm that these strings are consistent with random dispersion, and we turn to this discussion now.

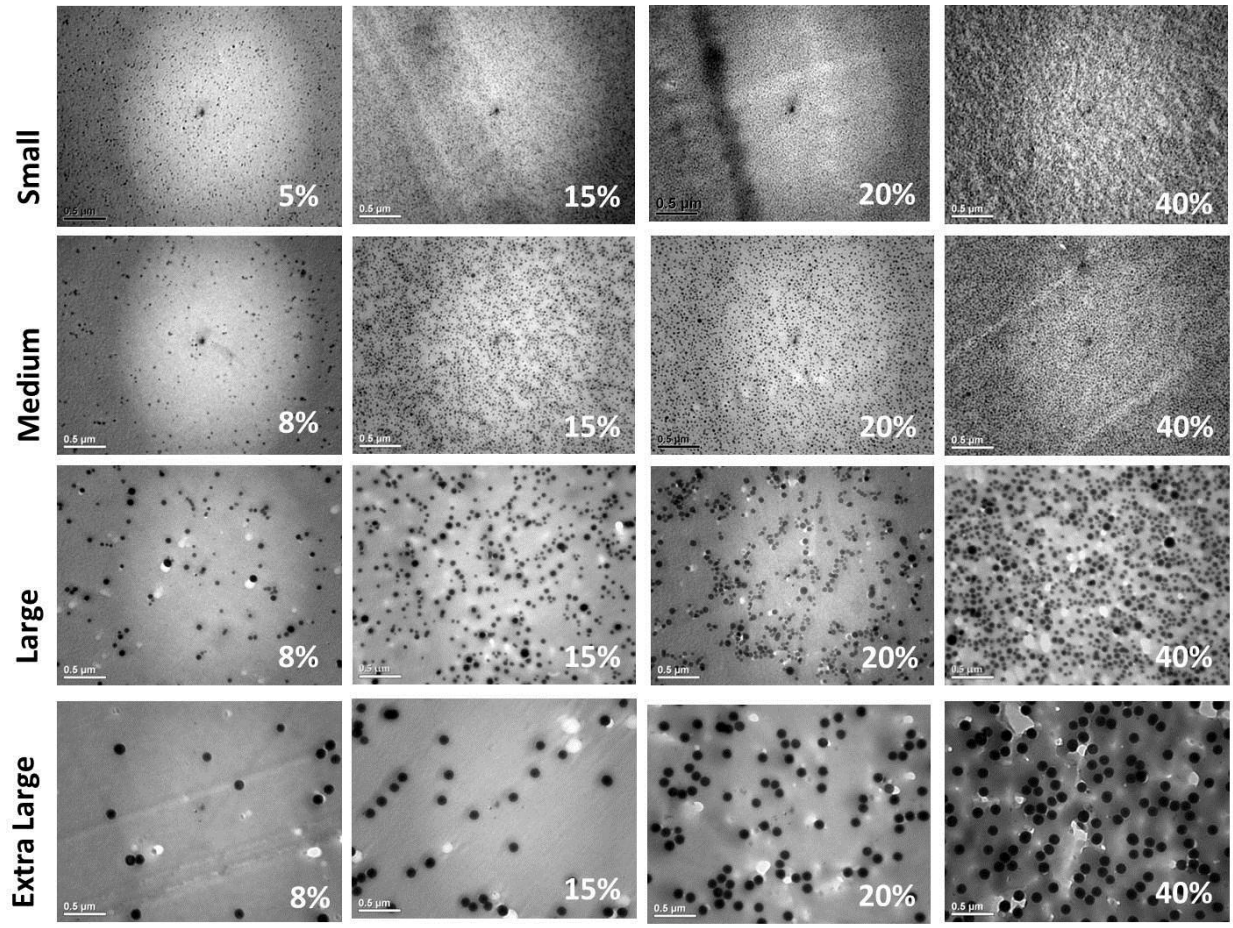

Figure 5.7 *Using the preparation procedure described, the particles are well dispersed independent of the weight fraction and of size.*

In the qualitative assessment of dispersion quality presented in Figure 5.7, in order to further confirm randomly dispersed samples, image analysis was done. This was the result of our concern over the fact that a quick perusal of the micrographs suggests that the particles often appear to be arranged as strings. Are the strings of particles that are observed a result of natural multi-particle associations in a two dimensional projection of a random, three dimensional particle distribution? In order to compare the dispersion states achieved to the ideal dispersion state, the following experiment was performed: micrographs for the large particle composites at five different weight percents (8, 10, 20, 30 and 40) were binarized using Image J software. Meanwhile, using the particle size distributions from the image analysis on the large particles, a computer generated three dimensional space with the dimensions of a

TEM slice was created (60nm thick x ~400nm wide x ~300nm tall). Inside, particles of sizes determined by the calculated distribution were randomly placed, until the desired weight fraction was reached. A 2-dimensional projection was then created of this three dimensional space, generating a truly random equivalent of the binarized images taken from the actual samples. Autocorrelation functions were performed on both the computer generated and sample generated binarized images. In Figure 5.8a the images created using a computer and using the actual samples are compared at 10% and 40% by weight. In Figure 5.8b, the difference between the autocorrelation function for the computer generated and sample generated images is shown. In each case, the computer generated images seem to be slightly larger, perhaps due to an underestimated particle size distribution. The shapes of the autocorrelation functions do not deviate considerably from each other, and the results are taken as evidence of truly random dispersion. Of special interest is that the occasional strings of particles that are observed in the electron micrographs are also present in the randomly dispersed computer generated images!

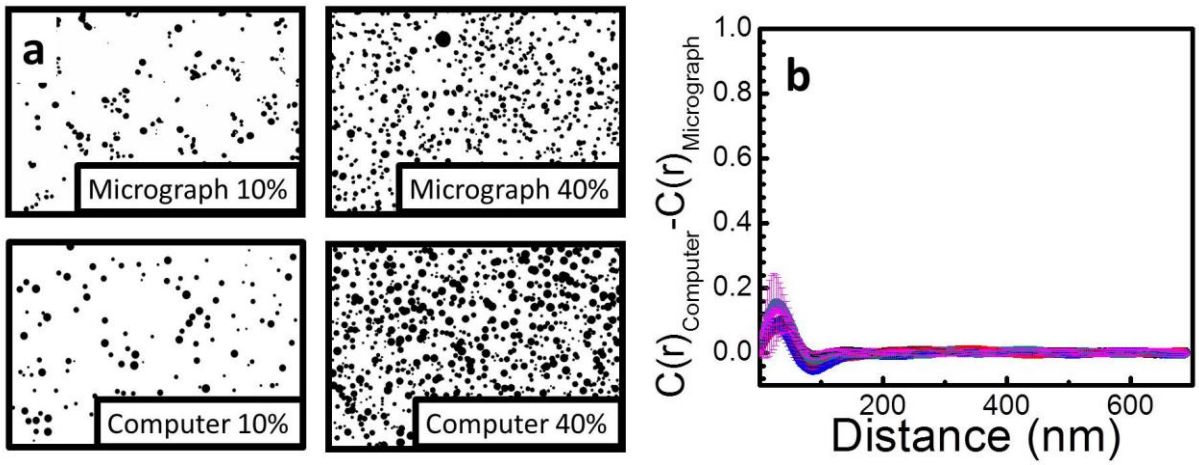

Figure 5.8 *Dispersion quality as confirmed through comparisons of computer generated and micrograph generated binary representations of 10% and 40% by weight samples (a). The autocorrelation function for the computer generated image was slightly higher at all weight percents, as demonstrated by the difference between the two functions (b). This is consistent with random dispersion in both sets of images, but a slightly larger particle distribution in the computer generated images. Five particle loadings were studied, 8(black), 10(red), 20(blue), 30 (teal) and 40 (magenta) percent* ***SiO_2*** *by weight.*

5.4.2 Nanoparticle Size

For the three largest sizes, a size distribution was determined by image analysis from TEM and compared to a size analysis using a DLS (Figure 5.4). For TEM, several hundred particles were imaged and the resulting images were binarized and analyzed to create a size distribution. Both the TEM and the DLS gave average particle sizes that were on the high end of Nissan Chemicals range of particle sizes and the agreement between the two was generally good. Because of the much higher statistics involved in a scattering experiment, the average particle sizes obtained this way were used in all calculations. For the S nanoparticles, because the size approaches the limit of accurate measurement for both TEM and a DLS, we instead take the well recorded literature value of ~14nm in diameter for these particles[10, 44, 45]. Average particle sizes for the particles were thus determined to be: 14 for the S particles, 22.2 for the M particles, 70.5 for the L particles in isopropanol, 87.4 for the L particles in MEK, and 114 nm for the XL nanoparticles. As a side note, the noticeably larger particle size as compared to the Nissan distribution for the L particles is a product of how the size distribution was calculated. The size distribution for the L particles as contained in the bottle is actually significantly broader, however not all of these particles are included in the pellet resulting from centrifugation (some of them are too small). Thus, we see a significantly narrower and smaller diameter range than what is measured straight from the vial. For the smaller two particle sizes, this is not an issue, as the particles are close enough to each other that they are bridged by polymer, and thus connected by a particle polymer network (at 30% by weight of particles). Therefore, all particles make it into the pellet. Note: if only bare particles in solvent are centrifuged, then the two smallest particle sizes form no pellet, and the XL Nissan nanoparticles form a pellet that has approximately twice the volume of the L nanoparticles. In this work, all calculations are carried out using the average measured particle diameter.

5.5 Bound Layer Dependence on Particle Loading

In Figure 5.6 we plot the fraction of SiO_2 in the pellet as a function of particle loading (the remainder of the pellet is adsorbed polymer). This is done for the S nanoparticles. In the figure, we plot the fraction of SiO_2 in the freshly prepared composite, and after four different wash cycles. Ten samples ranging from 16-86% SiO_2 by weight were studied in order to determine the effect of weight percent on 'bound layer' thickness. For small weight fractions, we do not expect to see a difference in the calculated 'bound layer' thickness, as there is plenty of polymer to form a full equilibrium bound layer. As the weight fraction is increased, the total amount of polymer available per particle should decrease, and at some point, there may no longer be enough to fully distribute itself to the nanoparticles. Such a scenario would presumably lead to a decrease in the 'bound layer' thickness (an increase in the percent SiO_2, in Figure 5.6). Apparently, even at the highest NP loadings studied, this threshold is not reached. The thickness of the 'bound layer' was essentially invariant. Even at a loading of 86 wt % (which translates to 76% volume) the particles are still able to form a full (or very close to full) equilibrium layer. Note, however, that to ensure that the amount of polymer would not limit the bound layer size, all actual 'bound layer' experiments were done with particles that were 40% or less by weight of SiO_2 particles.

The invariance of bound polymer with weight fraction suggests two things: first, the NPs adsorb strongly beginning in solution and as long as enough polymer exists to form a full 'bound layer' it virtually all goes to the surface. This is in good agreement with the strongly attractive surface. The adhesion energy for SiO_2/P2VP has been estimated using infrared spectroscopy to be -350 mJ/m^2[132]. It is also in agreement with DLS measurements on solutions of particle and polymer. Second the particle dispersion is maintained even at very high weight fractions were it is difficult to accurately determine dispersion from TEM. Only at the very highest weight fractions do we begin to see a drop off in thickness, and this is where there is not enough polymer to fully distribute, no matter how strongly it

adsorbs, or how well dispersed the particles are. Unfortunately, weight fractions larger than 86% could not be tested, due to the difficulty of preparing composites at such high loadings. All the composites converge to the same bound layer thickness after two washes, and throughout this manuscript, this is the number of washes utilized.

5.6 Bound Layer Dependence on Annealing

We now consider the effect of annealing at high temperatures on bound layer thickness for polymer nanocomposites. The purpose of annealing is to achieve a full, equilibrium bound layer. In order to determine the appropriate annealing time, the bound layer thicknesses of particles of size L annealed from 6 hours to 8 days were compared. The large particles were chosen as they are approximately the same size and they come in both of the studied solvents and thus facilitate a solvent comparison. The results in Figure 5.9 show an increase in bound layer thickness from 6 hours up to 3 days. Beyond 3 days of annealing, the thickness remains roughly constant with perhaps a slight decrease in thickness at the longest time of 8 days (possibly indicating degradation). The results are consistent for both IPA and MEK although in all cases the IPA particles have a thinner bound layer, expected given the smaller particle size. However, a thinner bound layer in IPA was also achieved when particles of the exact same size were washed in the two different solvents. Based on these results, as a precaution, all samples were washed with MEK, even those prepared in IPA. Five days is also apparently

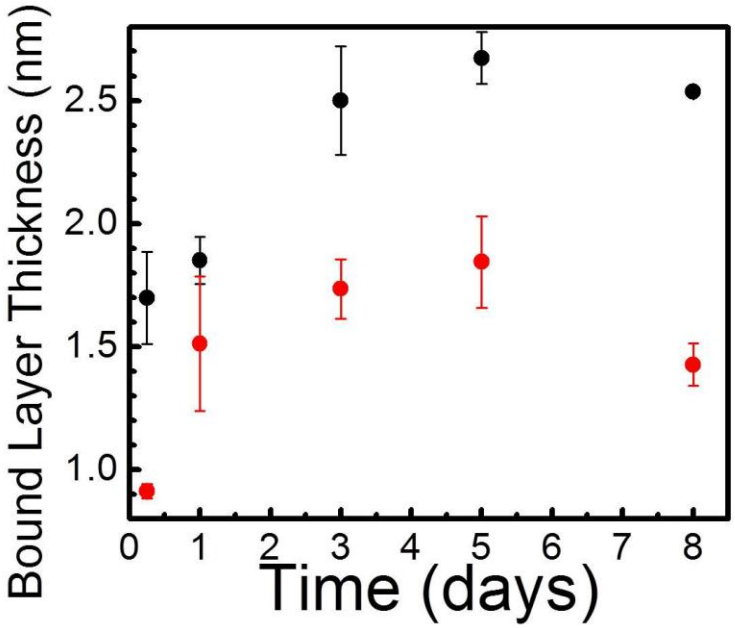

Figure 5.9 *Bound layer thickness as a function of annealing time for large Nissan particles in both IPA (red) and MEK (black).*

the optimal annealing time for the formation of a bound layer. Apparently, in solution, the chains do not fully adsorb, presumably because of competition with the solvents. Pyridine is used as a co-solvent and it is a strong Lewis base. In solution, it competes with the P2VP for surface sites, therefore annealing is crucial to allow a full bound layer formation.

5.7 Bound Layer Dependence on Particle Size

We now turn to the bound layer thickness as a function of particle size. As we treat the separate solutions of the L particles as two different sizes, this gives us five sizes for consideration. This is a limited but still meaningful number, and provides a clear trend in behavior. Here we performed bound layer calculations on samples both before and after annealing, and the results are shown in Figure 5.10. We plot bound layer thickness vs. both particle diameter and one over the diameter. In the latter case the thickness for a planar surface can be extrapolated by looking at where the curve intercepts the y-axis. Visually, this is between 4 and 5 nm, which fits well with the thickness of planar surfaces that have been measured in the literature (around 4nm).

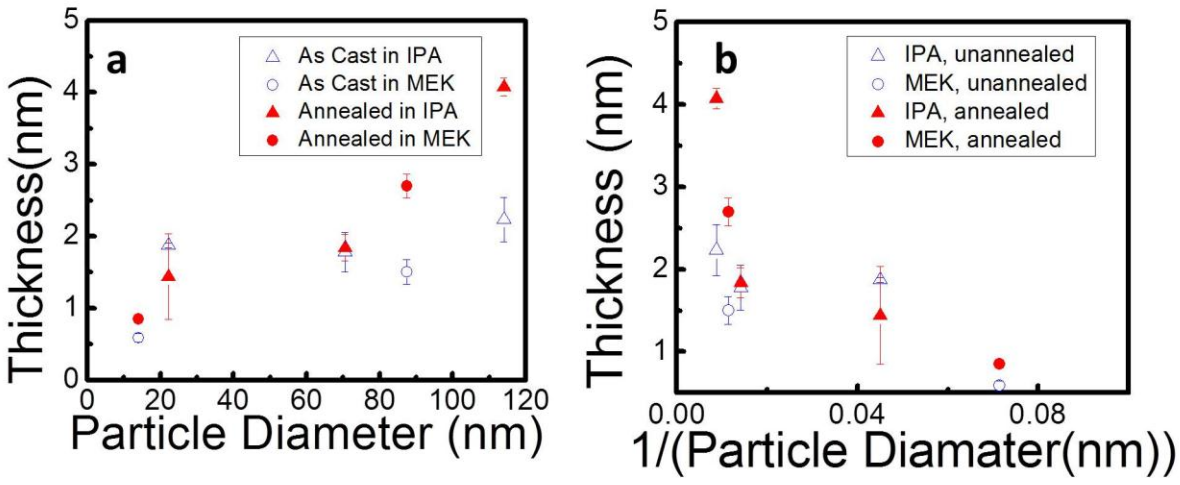

Figure 5.10 *Bound layer thickness as a function of particle diameter (a) and one over the particle diameter (b). Both as cast (open blue) and annealed (closed red) composites are studied in IPA (triangles) and MEK (circles).*

In fact, nanoparticles of sizes even smaller than 14nm in diameter were also measured. These particles were procured in both a powder state and in solution with MEK from Meliorum technologies. The bound layer measured in these cases was of an even smaller thickness than what was measured for 14nm particles, however the results are not reported because a well-dispersed state was not confirmed for the nanoparticles. After multiple attempts at improving dispersion, the only state that could be achieved were small aggregates of particles (Figure 5.11). The thinner bound layer found for these particle sizes is consistent with expectations, but the measurement accuracy on these small nanoparticles is somewhat in doubt.

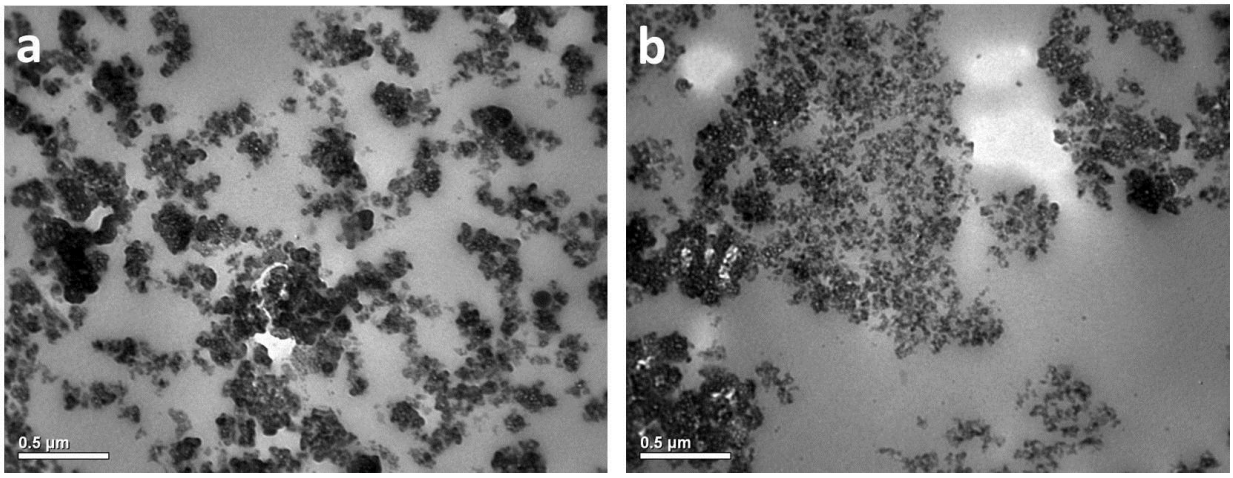

Figure 5.11 *Dispersion state achieved for very small particles at two diameters: 4nm (a) and 10 nm (b).*

It is important to put the decrease in 'bound layer' with nanoparticle size in context. Since the surface area to volume ratio and interparticle distance continue to increase and decrease respectively with decreasing nanoparticle size, there must be some competing effect that opposes these phenomena. This opposition is expected to become stronger as the particle size is diminished. Building off the results in Chapter 2 in which we showed that in PS-SiO_2 nanocomposites the nanoparticle interactions are undeniably mediated by the attached polymer chains (in that case grafted) we postulated that the ability of the polymers themselves to mediate interactions between the particles is

decreased as the particle size decrease until eventually it is non-existent. This picture fits well with the experiments on the bound polymer layer thickness presented.

5.8 Bound Layer Dependence on Molecular Weight

Finally, we consider the effect of P2VP molecular weight on bound layer thickness. The results are presented in Figure 5.12. Because the molecular weight range included very low weights (e.g. 2kg/mol, 5kg/mol) such that the polymers would have difficulty bridging particles, the measurements on the S particles were difficult, and usually only one pellet was burnt. (These particles are not large enough to form pellets without particle-polymer-particle bridging.) This is why these data points do not have error bars. The increase in 'bound layer' thickness with increasing P2VP molecular weight is in line with the experiments of Tannenbaum et al.[133] who obtained the same result for cobalt oxide particles in PMMA. Additionally, Cohen-Addad[134] found an increase in bound layer with increasing polymer molecular weight in a silica-siloxane composites. Specifically, it was found that the bound layer goes as the square root of the molecular weight of the adsorbed polymer and this was explained with two different models of polymer behavior. For the S particles, it is not clear whether there actually is an increase in size or whether the curve is level. To better understand this behavior, we compare these results to the bound layer found for particles mixed with polymer in solution, which was measured with DLS. These results are presented in Figure 5.13. The first thing to note is that in solution, the larger particles still appear to have a thicker

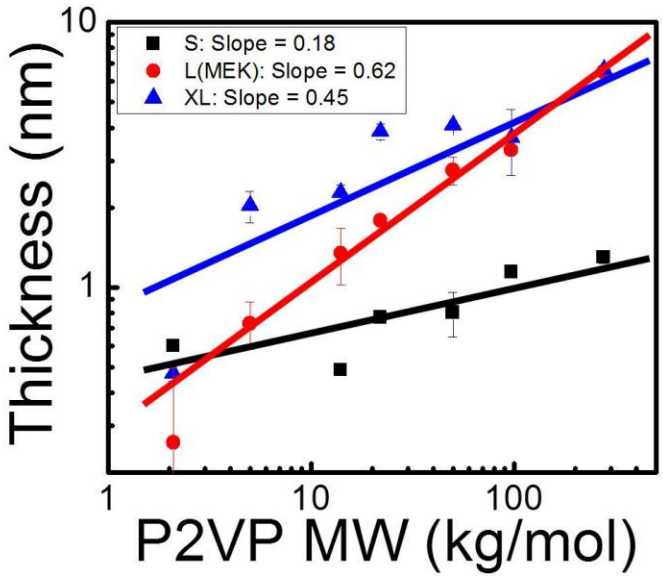

Figure 5.12 *Bound layer dependence on P2VP molecular weight for S particles (black squares), L particles in MEK (red circles) and XL particles (blue triangles).*

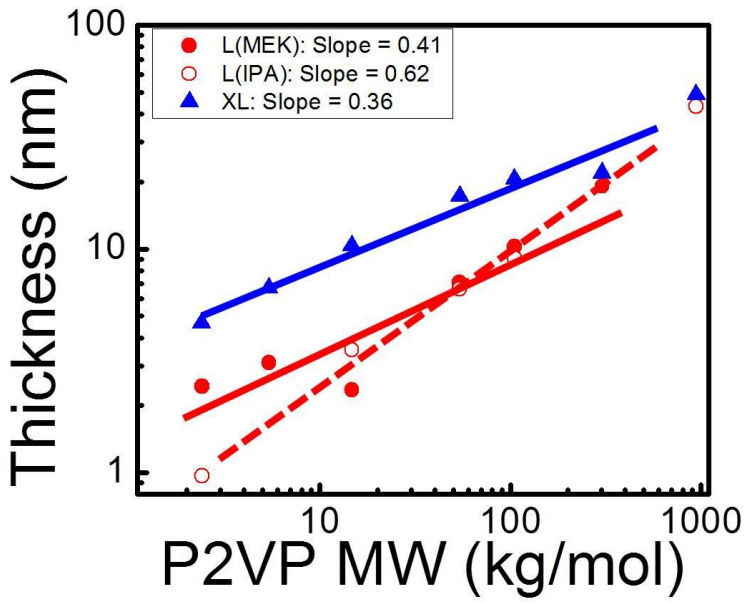

Figure 5.13 *Bound layer dependence on P2VP molecular weight for L particles in MEK (solid red), L particles in IPA (open red) and XL particles (blue). All measurements were taken using DLS of solutions of polymer and particle in their respective solvents.*

'bound layer' and the bound layer of all the particles in solution is greater than that in the melt. The S and M 'bound layers' could not be measured in solution because the bare particle size is too similar to the size of the polymer measured by DLS. Clearly, these solution measurements represent an overestimate of the 'bound layer' in the melt, however the TGA measurements probably represent an underestimate (as some not insignificant amount of bound polymer might be removed in the washing step). Thus by performing both types of measurements, we create a lower and upper bound for the actual bound layer thickness.

5.9 Conclusions

In conclusion, we observe a bound layer at ~1nm in thickness for three different polymers with an attractive interaction with SiO_2. As the particle size is increased we observe a steady increase in the bound layer thickness, and we postulate that this could be responsible for the decreasing ability of particles to reinforce nanocomposites at very small particle sizes. In fact, if the particle size is small enough, the bound layer may completely disappear! We thus present this as a mechanism for the plasticization of PNCs when solvents or very small particles are added. We show further that as the molecular weight of the polymer is increased the total amount of polymer bound to particles also increases, and this is consistent with the literature.

6. Rheology and X-ray Photon Correlation Spectroscopy on Bare Particle Systems: Dispersion and Weight Fraction

In order to achieve a more general understanding of polymer-particle nanocomposites, it is necessary to consider polymer-particle pairs both where there is repulsion between the particle and polymer (e.g. PS-SiO_2) as well as systems in which there is attraction. In Chapter 2, a great deal of attention was paid to the effect that SiO_2 dispersion state and SiO_2 weight fraction have on nanocomposite properties for a repulsive system. Despite the repulsion, the dispersion was controllable via grafted polymer chains, which mitigate the dislike between the polymer and particle. In this chapter, the focus turns to an attractive system, SiO_2 in P2VP. This system was discussed in great detail in Chapter 5, in the context of polymer 'bound layer' thickness dependence on particle size and other variables. A discussion of mechanical properties in this system, and specifically their dependence on particle dispersion and weight fraction, were not discussed in Chapter 5 and are instead discussed here. Because the SiO_2 particles are naturally miscible with P2VP, new strategies must be employed to study dispersion.

6.1 Rheology and X-ray Photon Correlation Spectroscopy at Different Weight Fractions

X-ray Photon Correlation Spectroscopy allows for the microscopic characterization of mechanical reinforcement. In the past, the Kumar group has run XPCS experiments on two extremes of dispersion in the grafted particle system: one well dispersed and one with the nanoparticles arranged in sheets. In the first system there was no evidence of mechanical reinforcement at low particle loadings (5% or less). In the second system mechanical reinforcement was occurring even at particle loadings as low as 1%.[10] In combination with the rheological data presented in Chapter 2 of this work, this is consistent with significant improvement in mechanical properties as a function of particle dispersion. How

dispersion affects mechanical properties in a bare particle system will be discussed in detail later on in this chapter. However, because, as was discussed in Chapter 5, the bare particle system is comprised of particles of several different sizes, it is also important to understand how particle size affects nanocomposite mechanical properties. To facilitate these studies, nanocomposites at many different weight fractions and of many different particle sizes were prepared as discussed in Chapter 5. Some were sent to collaborators at Penn State University, to run rheological measurements, and some were studied in house, using TGA and other methods (primarily discussed in Chapter 5). In order to compliment the rheological experiments, several visits were made to Argonne National Laboratory, beamline 8-ID-XOR to run X-ray Photon Correlation Spectroscopy experiments. These experiments are the x-ray equivalent of dynamic light scattering and were discussed in more detail in the introductory chapter. Using XPCS, one can determine the diffusion coefficient of the particles as well as other signatures of gel-like behavior. Diffusion of particles is heavily affected by the presence of entangled polymers[135]. In Figure 6.1, we focus on the diffusion coefficient as a function of time for composites with 14nm SiO_2. The diffusive behavior observed for the nanoparticle motion is in line with other XPCS measurements on polymer nanocomposits [136]. The samples are not well equilibrated as the diffusion coefficient of the particles generally decreases with time, and at any rate does not reach a level, long time value. This is a difficulty of working with glassy systems, which can take long amounts of time to fully relax. However,

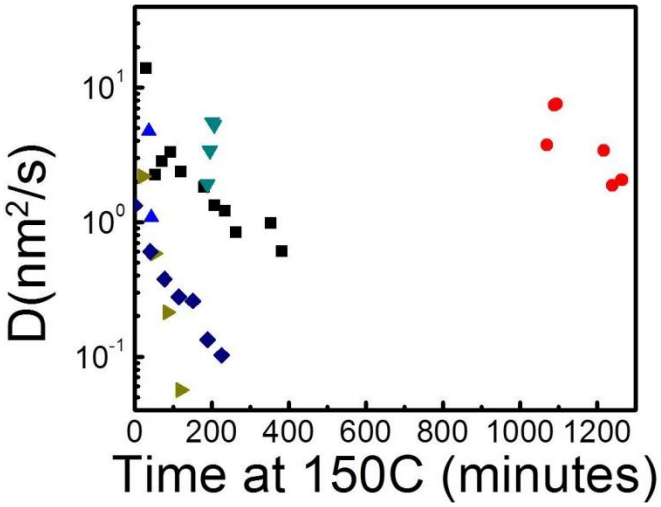

Figure 6.1 *Diffusion coefficient as a function of time annealing for S (14nm diameter) SiO_2 particles at several different loadings: 2.5 weight % (teal), 15 weight % (black, blue, and red), 40 weight % (olive) and 60 weight % (dark blue). The 15 weight % samples were repeated three times.*

of immediate note is the relatively sharp decline in diffusion coefficient starting at a weight percentage of 40. This suggests percolation of the samples, however, where this percolation occurs is not clear because of the sparsity of weight fractions studied. One can still draw a clear contrast with grafted particles, where even the well-dispersed particles had already percolated at 15 weight percent (according to both XPCS and SAOS data). In the bare particle system, there is a large gap between 15% and 40% (where we first see the dramatic drop in diffusion coefficients), and it is therefore not completely clear where percolation begins. Thus these results seem to indicate that intermediate loadings are needed in bare particle systems to observe true solid-like behavior and plans are under way to study samples intermediate to 15 and 40% with XPCS.

In the absence of additional XPCS data, rheological results are presented in order to lend more clarity to the behavior of the material in these intermediate weight fractions. Rheological measurements were done on many loadings of composites made from all the different particle sizes offered by Nissan. These measurements were done by collaborators at Penn State University.

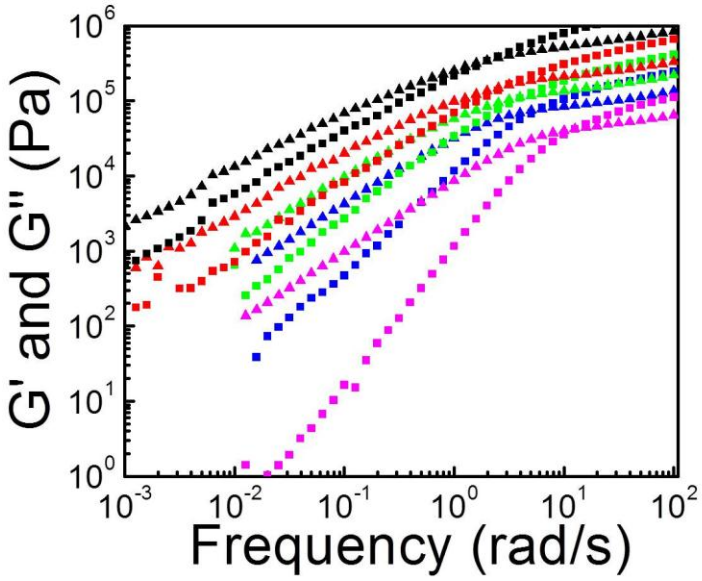

Figure 6.2 *G' (squares) and G'' (circles) for the 97 kg/mol homopolymer (magenta) and particles loaded with four different weight percentages of S (14nm diameter) silica particles: 10% (blue), 20% (green), 30% (red) and 40% (black).*

In order to directly compare these results with the XPCS diffusion data in Figure 6.1, in Figure 6.2 SAOS results from S (14nm diameter) SiO_2 composites at four different weight percentages are presented. The samples studied include 97 kg/mol P2VP, and 10, 20, 30, and 40% SiO_2 by weight. Immediately noticeable is that, in stark contrast to the 14nm particles studied in Chapter 2, where even at only 8% by

weight there was clear evidence of a low frequency plateau corresponding to the solid-like response of the particle network, here there is no such plateau even at loadings of 40%. This was the case at all SiO_2 particle sizes studied. Even at the highest loadings studied (which was typically 40%) no plateau was seen! While it could be that some of these samples display a plateau at frequency regimes below the measureable range for ARES, the result is still very surprising. In order to better understand this, the following analysis is considered: The storage modulus in rheology must decrease as the frequency decreases. On a log-log plot, the slope of this storage modulus can range between two extremes. A slope of zero will be observed for a low frequency plateau corresponding to a solid like response of a particle network, whereas for terminal relaxation the slope will be two (this is what is seen for the pure polymer). Thus the low frequency G' can be normalized by the slope of the pure polymer and the slope of this normalized function on a log-log plot will range from 0 for the pure polymer itself, down to -2 for a composite showing a solid-like network response. The results of this analysis for all four particles are shown in Figure 6.3. From this analysis, it appears the S and M particles (14nm and 22nm in diameter) have an increasing solid-like response with increasing loading, and that a maximum in reinforcement behavior as a function of particle size is perhaps achieved for M particles. However, for all four particle sizes studied, the loadings reach values as high as 50% by weight, and still no plateau is apparent at measureable frequencies! This is in stark contrast to the

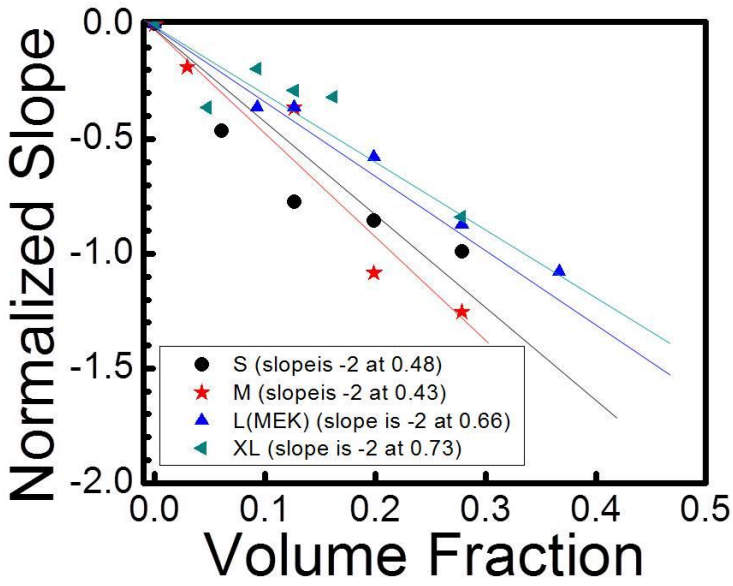

Figure 6.3 *Normalized low frequency slope on a log-log plot for four different particle sizes as a function of loading. A plateau in the storage modulus (indicative of solid like behavior) will lead to a normalized slope of -2*

grafted particle system discussed in the earlier chapters. This is consistent with Ndong et al., who looked at polydisperse, 20nm titania particles in PDMS that were both bare and grafted with PDMS. At matrix molecular weights comparable to the ones used here they found that grafted particles resulted in a much larger increase in the viscosity of the composite as compared to the neat melt[137].

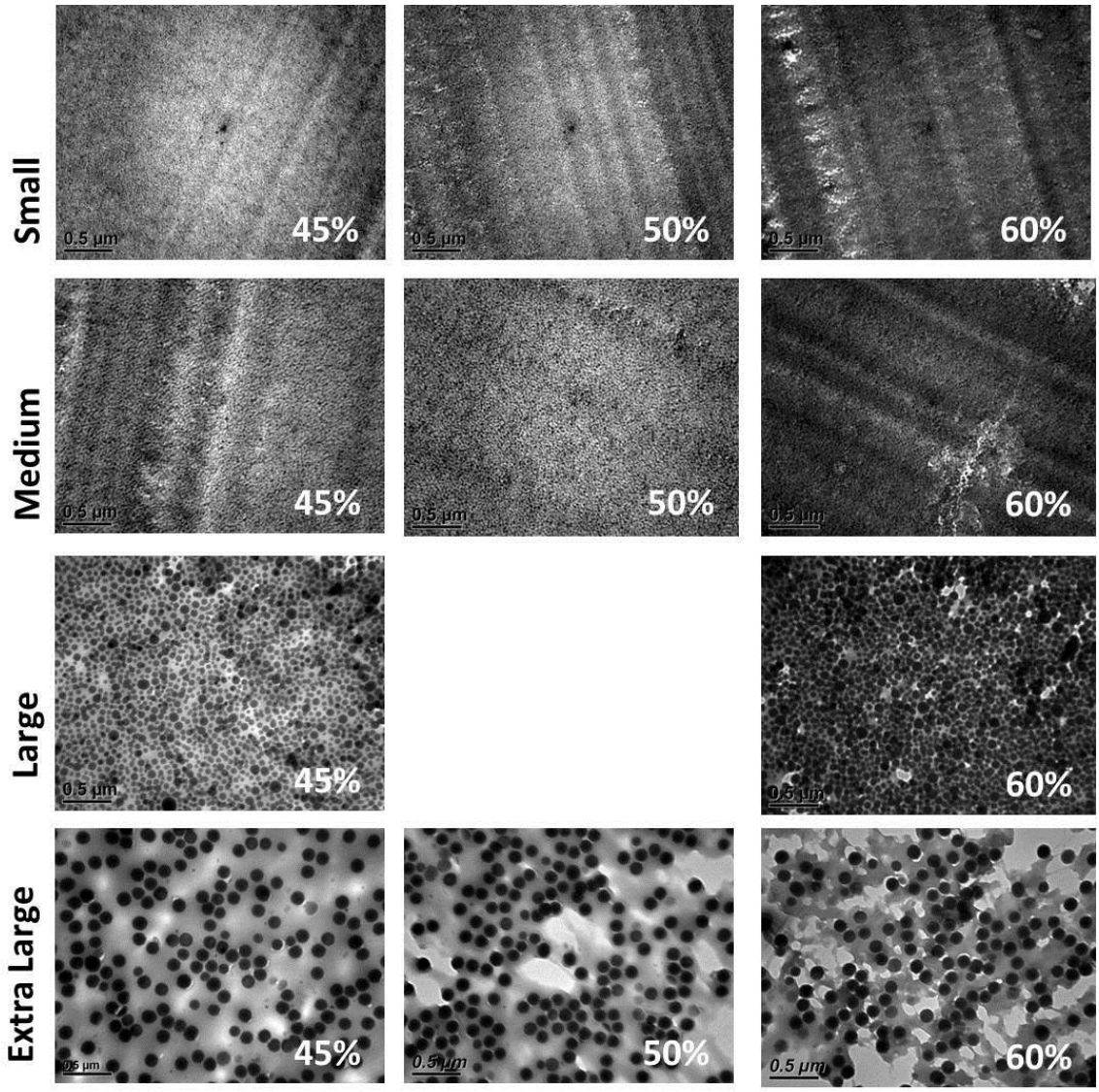

Figure 6.4 *TEM micrographs at high weight percentages for the four particle sizes. The loadings shown are 45, 50, and 60% by weight. The TEM for the nanocomposite composed of L particles at 50% is conspicuously absent.*

Since apparently, very high loading fractions are needed in order to see long-lived solid like behavior from bare nanoparticle composites, samples were prepared at much higher loadings. TEM micrographs

were taken to test the dispersion quality. These can be seen in Figure 6.4, but rheological experiments on these high loading samples have not yet been performed. However, this first step is important, as it was not initially clear whether it was even possible to make particles past a certain weight fraction.

6.2 Effect of Solvent Choice on Miscibility of P2VP and Silica

In the discussion of SiO_2-P2VP nanocomposites in Chapter 5, P2VP and SiO_2 were added in appropriate proportions in a solvent mixture primarily composed of methyl ethyl ketone, with a small, additional amount of pyridine added, to prevent bridging of the particles in solution. The mixtures were solvent cast and the resulting samples were dried and annealed (see section 5.3) in preparation for further experimentation. Pyridine acts as a displacer of P2VP on the surface of SiO_2, and in its absence, when particles are mixed with the polymer, a series of bridging events takes place. These events result in macroscopically large clusters of particles, which precipitate from solution. Small amounts of pyridine can be added to prevent this process. However, given enough time, this precipitate has been observed to slowly re-enter the solution, *even in the absence of pyridine*. Apparently, in solution, the P2VP is not irreversibly adsorbed to the surface, and the polymer is constantly detaching and reattaching. Given the favorable gain in entropy, the equilibrium state is one in which each particle eventually enters solution, with its own independent bound polymer, and bridging is diminished, if present at all. Indeed, this picture is reinforced by dynamic light scattering measurements taken of the particle-polymer solution, which show augmentation of the primary particle size, but on a scale much too small to be accounted for by particle agglomerates in solution, and much more likely to be a result of polymer bound to *individual* particles.

Thus, the minute amounts of pyridine added in the experiments in Chapter 5 served simply to prevent the initial bridging and quicken the process of sample preparation. Given enough time, the same well dispersed particles will result. However the ability of pyridine to act as a displacer can have a

striking effect on dispersion morphology. To illustrate this, in Figure 6.5a, TEMs are displayed at four different concentrations of pyridine relative to the total amount of SiO_2. The concentration was varied at values intermediate to what is shown in the figure, but for clarity, these are left out. Apparently, if the pyridine concentration is too high, the dispersion is sub-optimal, but below a concentration of pyridine of ~0.8 (mL Pyr/g SiO_2), good dispersion is achieved. (Note that all the experiments in Chapter 5 were performed using a concentration of 0.7 (mL Pyr/g SiO_2). In Figure 6.1b, autocorrelation functions on several images are displayed, showing more quantitatively the shift from good to poor dispersion. These surprising results prompt the question, what if the nanocomposites are prepared in the complete absence of pyridine, are they still well dispersed? Alternatively, what if the nanocomposites are prepared in the absence or near absence of MEK (i.e. using pyridine as the solvent)? When 14nm Nissan particles were taken from the initial concentrated solution in MEK (~31 weight percent), added to pyridine, and mixed with P2VP, the composites displayed even more dramatic aggregation than is seen in Figure 6.1. The solution of SiO_2 particles in pyridine, sans P2VP, remains clear, suggesting well-dispersed particles, and this is consistent with the dynamic light scattering measurements which show

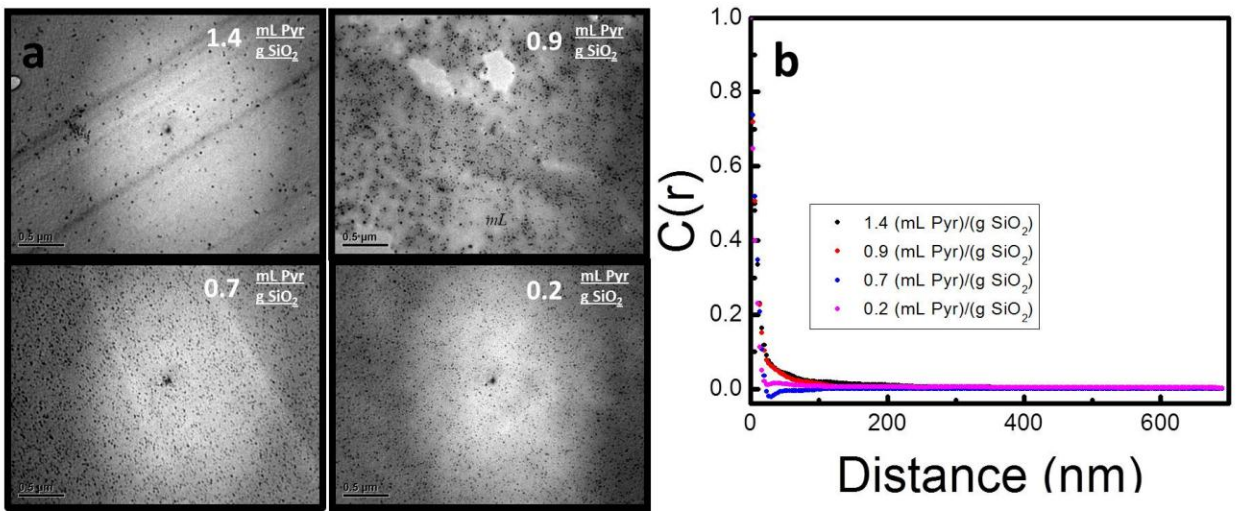

Figure 6.5 *TEM micrographs showing dispersion quality as a function of pyridine concentration in the preparation solution (a) and a quantitative analysis of dispersion quality using a radially averaged autocorrelation function (b) which shows the onset of aggregation is probably at a pyridine concentration of ~0.8 (mL Pyr)/(g SiO_2) for the S particles (14nm in diameter)*

the same particle size independent of the choice of pyridine or MEK as solvent. Upon P2VP addition to this solution no cloudiness or opaqueness results, again precluding the possibility of aggregation. Dynamic light scattering for solutions of P2VP and SiO_2 in pyridine show a bimodal distribution in particle size, where the two peaks represent the size of the particles and polymer in their independent respective solutions. This suggests that the components in the solution are not aggregating, however the augmented particle size observed in a solvent of MEK is not seen (recall this resulted from P2VP binding to the SiO_2 surface). Apparently, during the solvent casting process, aggregation of the particles occurs, as the resulting composites show dramatic particle aggregation. The striking difference in the dispersion states can be seen in Figure 6.6, where composites prepared in the different solvents are compared (at 5 different weight percentages of SiO_2). While particles produced solely in methyl ketone present a uniform dispersion state, the pyridine procedure results in large aggregates of particles. Note that this difference is most pronounced at low weight fractions of SiO_2 and seems to disappear past a weight fraction of 20%. Indeed, as the weight fraction increases, the number of particles in solution increases, but since the total volume of the preparation solution was held constant, the (mL of pyridine)/(g SiO_2) necessarily decreases (from ~112 to ~12) and according to Figure 6.5, this might lead to a decreased propensity for aggregation. However, since all the values are still well above the concentration threshold where good dispersion was achieved in Figure 6.5 (~0.8 (mL of pyridine)/(g SiO_2)) an alternative explanation is that the particles are too concentrated at the higher loadings for significant differences in aggregation state to be perceived in a TEM micrograph, despite their existence. While it is not clear what is occurring on a microscopic scale, the propensity of the pyridine molecules to displace the P2VP on the surface suggests the following mechanism of aggregation: First, in solution, all of the particles are covered with pyridine, and no P2VP is able to make it to the surface. This pyridine remains at the surface as the solvent evaporates during solvent casting, and, due to Asukura and Oosawa depletion forces[138], the particles are driven together once the solution becomes sufficiently

concentrated. Alternatively, if MEK is used as the solvent, the equilibrium state in solution is well-dispersed particles each with a thin layer of adsorbed polymer. This state cannot be reached if pyridine is present at sufficient concentrations because all the surface sites that are available will be occupied. Furthermore, the aggregation of particles caused by Asukura and Oosawa depletion is kinetically trapped, as the poor dispersion observed in Figure 6.6 persists in the resulting nanocomposites even after annealing for several days at 50K above the glass transition temperature of P2VP.

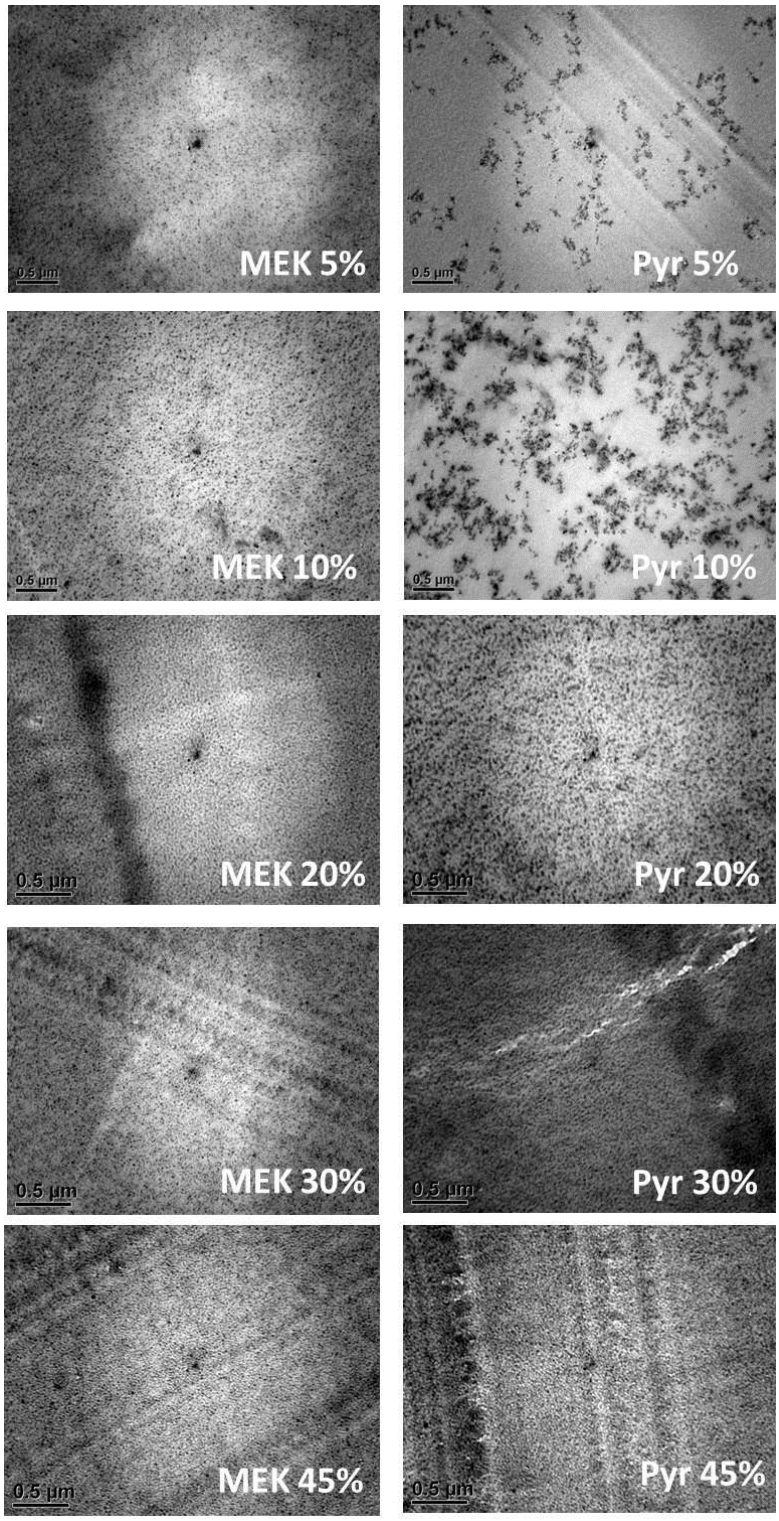

Figure 6.6 *Dispersion state of nanoparticles in P2VP as a function of preparation solvent (MEK or pyridine) and loading (5-45 weight %).*

Thus a bare particle system can be used to achieve two broadly different dispersion states, which, while they do not represent the full phase space of the morphology diagram presented in Section 1.4,

nevertheless present an interesting case study for how dispersion effects material properties in bare vs. grafted particle system.

6.3 Mechanical Properties as a Function of Dispersion for Bare Particle System

As was discussed in Section 6.2, the presence or absence of pyridine can have a dramatic effect on the nanoparticle dispersion in a bare SiO_2/P2VP system. In a grafted particle system, the dispersion state was found to have a critical effect on the resulting mechanical properties of the material. This was discussed in Chapter 2. However, in this same chapter, when two dispersion states were compared, both of a fractal network of particles, but with different graft densities and grafted chain lengths, it was found that longer graft chains at slightly lower graft densities contributed to better mechanical reinforcement. In the current study, there are no graft chains. Thus the opportunity presents itself to better understand the effects of dispersion in their absence. To do this, 14nm SiO_2 particles are mixed with 97 kg/mol P2VP in both methyl ethyl ketone (which leads to well dispersed particles) and pyridine (which leads to fractal aggregates of particles).

Since in Section 2.2.2 we saw that at a weight fraction of as low as 0.08 and probably much lower (according to our calculations, closer to a fraction of ~0.04) evidence was already present of a particle network in the low frequency rheology (in the form of a plateau in the storage modulus), a further point of interest is at what point a network can be discerned in these bare particle systems at the two extreme dispersion states, and thus we also study the rheology of the samples at more than one weight percent.

In order to facilitate this comparison, SAOS was performed. In Figure 6.7, we compare the low frequency storage and loss moduli of the 'dispersed' and 'aggregated' bare particle systems at 5 weight percent. This is the percentage of particles that was used in the bulk of the rheological measurements

taken on grafted systems. Whereas in the grafted particle case the difference between well dispersed particles and particle aggregates was dramatic, here we see almost no difference. It is not really clear which dispersion state gives the higher low frequency storage modulus. This is perhaps not surprising, since in the absence of graft chains the 'reach' of the particles is much smaller and therefore a greater number of particles are required to form the network that would be responsible for any increase in the storage modulus. Because of the particle organization in the aggregated sample, it is probably easier for these particles to form a network, however in both the 'dispersed' and 'aggregate' case 5% by weight of 14nm particle is likely too low for any far reaching particle interactions, since in the grafted system, where the grafts added an extra 5-10nm in length to the particles, 5 % particles was at the threshold. It is apparent from work shown in Chapter 5, however, that there is a significant amount of bound polymer in both of these systems and indeed, its magnitude should be considerably greater in the dispersed system, where there are no particle-particle contacts and thus presumably more surface available for polymer binding. Since this bound polymer has often been proposed to operate as an additional glassy layer which effectively increases the filler volume fraction it seems prudent to use this to try and explain the small differences we see in the low frequency G'. That is, these differences could simply arise because of an effective slightly larger filler loading.

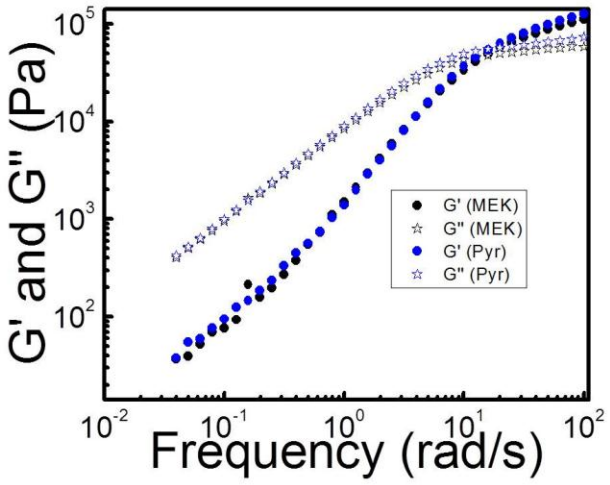

Figure 6.7 *Low frequency storage (closed circles) and loss (open stars) moduli for composites of 14nm in diameter bare silica particles in P2VP. Two preparation solvents are used MEK (black) which leads to well dispersed particles, and pyridine (blue) which leads to particle aggregation.*

In Figure 6.8, the SAOS data for two dispersion states created using different preparation solvents at a loading of 10 weight percent is presented. An additional, well-dispersed sample with some 0.7 (mL Pyr/g SiO_2) is considered. Here again little to no difference is seen between the two dispersion states. However, the well dispersed samples shown here have an unambiguously larger low frequency storage modulus. The sample with a mixture of pyridine and MEK was prepared using the same concentration of pyridine as the samples in Chapter 5. In the context of the bound glassy layer, this makes sense, as one can expect this layer of bound polymer to add to the total volume fraction of glassy material. Indeed, when the SAOS data is used to calculated the complex viscosity, we see that as this variable heads toward the limiting case of the frequency equaling zero, the viscosity calculated is larger for the well-dispersed case by approximately 20%. This percentage is the same percentage increase in the volume of glassy material that would be expected if these well-dispersed particles had a full equilibrium bound layer (~0.8 nm in thickness, as calculated in Chapter 5). However, the error bars on the measurements preclude the drawing of any direct conclusions.

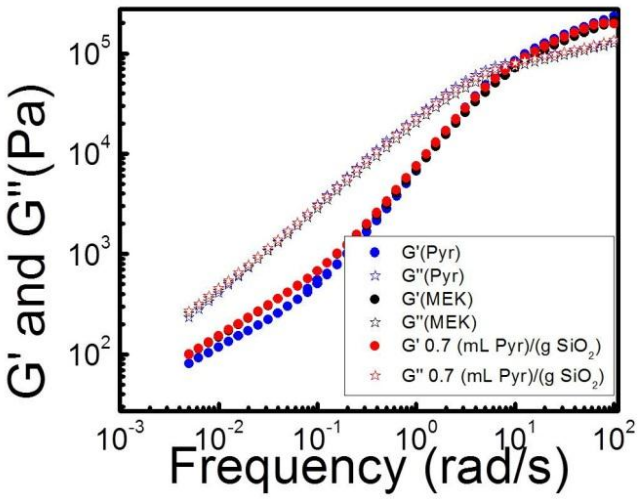

Figure 6.8 *Low frequency storage (closed circles) and loss (open stars) moduli for composites of 14nm in diameter bare silica particles in P2VP. Both MEK (black) which leads to well dispersed particles, and pyridine (blue) which leads to particle aggregation were used as preparation solvents. Additionally, we use the same mixture of pyridine an MEK that was used in Chapter 5 and led to well dispersed particles (red). This last data overlays with the well dispersed particles prepared in MEK.*

The minimal changes in properties as a function of dispersion seen here conflicts with the results presented on the effect of dispersion on mechanical properties in Chapter 2 and this is rationalized by a

fundamental difference between the two systems: the presence of the graft chains. Essentially, these chains extend the potential reach of the nanoparticles, and their absence here significantly increases the threshold at which a nanoparticle network can form. Essentially then, the dispersion state here has little effect. The entanglement number is not increased, and the particles are reinforcing the polymers by a more straightforward mechanism which is proportional to volume fraction only, and minimally dependent on dispersion state.

7. Other Avenues to Varying Particle Dispersion State

In Chapters 1-4, the broad applicability of grafted nanoparticles controlling dispersion properties in polymer nanocomposites (and by extension, mechanical properties) was discussed. However, the dispersion states achieved were limited to the extent that they depended on a PS matrix. Furthermore, the synthesis of the particles themselves was involved and not easily amenable to scale up. Thus, to lay the foundation for the use of particles grafted particles in actual materials, it is important to determine the feasibility of new routes of creation of these particles.

In this chapter, experiments involving two broad goals are discussed: First the extension of the morphology diagram to include other matrix polymers, and second, the use of di-block copolymer and bare SiO_2 particles to mimic grafted particles.

7.1 Self-Assembly of Grafted Particles in Poly (2-vinyl Pyridine)

In order for grafted particle self-assembly to have broad industrial applications, the self-assembly should not depend on a specific choice of matrix. To see if this is potentially the case, it is important to consider the driving forces behind the dispersions achieved in the original PS grafted SiO_2 nanoparticles and PS homopolymer, which, as the reader recalls, are displayed in the phase diagram in Figure 1.3. The dispersion in these systems is a function of the miscibility of the three components in the system: the grafted polymer chains, the matrix polymer, and the SiO_2 particles. The SiO_2 particles are generally immiscible with PS, but since the grafted PS chains are chemically bound to the surface, the particle and grafted polymer cannot phase separate. The grafted polymer and matrix polymer miscibility depends on their relative lengths: When the graft chains are longer than the matrix chains, the solvent quality, α (as discussed in Section 1.4), is larger than unity and the two forms of PS mix. If the graft chains are shorter than the matrix chains than the grafted PS and the free PS segregate.

In light of this, it is reasonable that polymers that are miscible with the PS grafts (in the appropriate molecular weight range) would produce a very similar phase diagram to the one in Figure 1.3. Simulations suggest this is the case [43, 139]. Thus in this section, the focus is on matrix polymers that are immiscible with the PS grafts, but, miscible with SiO_2. As has been discussed in detail in Chapters 5 and 6, P2VP is completely miscible with SiO_2 particles under many mixing conditions, and this miscibility is primarily controlled by a bound layer of polymer at the particle surface. Thus, the amphiphyllic nature of the grafted particles can again be used for particle self-assembly in the P2VP system, and here the detailed information already known about bare SiO_2 in P2VP provides a foundation for understanding self-assembly.

Grafted particles with a diameter of 14nm are used, as discussed in experiments in Chapters 2, 3 and 4. In these chapters, two extremes of dispersion existed in the experimental morphology diagram (Figure 1.3). At low graft densities and grafted chain lengths, aggregates of particles were observed. At high graft densities and grafted chain lengths, well-dispersed particles were observed. In the case of bare SiO_2 particles in PS, phase separation leads to gigantic aggregates of particles (Figure 1.2). If P2VP is chosen as the matrix, this behavior will *reverse*. Bare SiO_2 particles are miscible with P2VP (Figure 1.2, Chapter 5). Meanwhile, P2VP and particles densely grafted with PS will be immiscible. At high graft densities and graft lengths, the SiO_2 core will be completely hidden by PS and the immiscibility of PS and

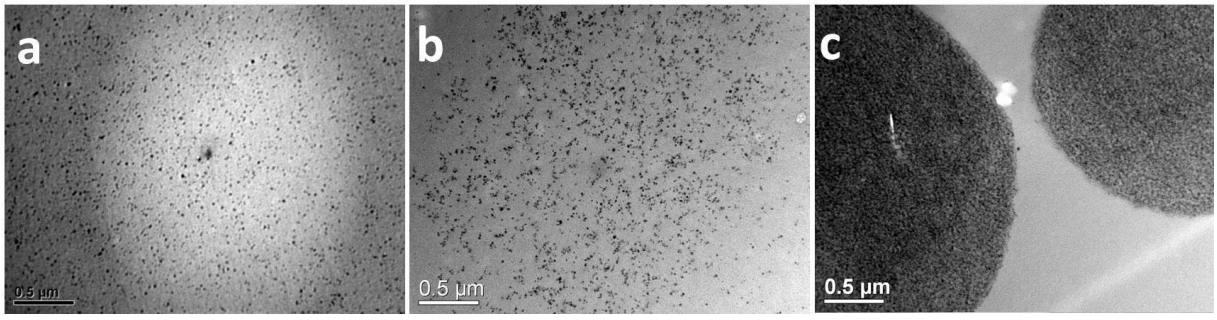

Figure 7.1 *TEMs of bare particles (a), lightly grafted particles (b) and densely grafted particles (c) in SiO_2*

P2VP will dominate and lead to phase separation. Indeed, this is exactly what is seen (Figure 7.1).

And what is the dispersion at intermediate graft densities and chain lengths? A reasonable supposition is that for PS grafted particles in a P2VP matrix a morphology diagram analogous to Figure 1.3 might show a complete reversal of phase behavior. For example, in the classic di-block copolymer phase diagram for two immiscible polymers, the morphology is symmetric and short hydrophobic blocks and long hydrophyllic blocks have morphologies that mirror short hydrophyllic blocks and long hydrophobic blocks[39].

The first point of consideration is that in the PS matrix system, the intermediate graft densities (where strings and sheets and fractal aggregates of particles were observed) were acting as a 'sweet spot' where the particles behaved as amphiphyles and thus self-assembled. That is, the definitions of low graft densities, intermediate graft densities and high graft densities used in the figure were dependent on the resulting dispersion states. Consider that the highest graft density used was 0.11 chains/nm^2. If one peruses the literature, it becomes clear that even this graft density (considered as densely grafted in the experimental morphology diagram) is relatively sparsely grafted when compared to what is possible. In general, the consensus of those who synthesize grafted particles is that densely grafted particles are equal to or greater than 0.5 chains/nm^2 [140, 141], almost an order of magnitude higher than the most densely grafted particles considered in this text. In this context, it becomes clear that the most interesting phase behavior occurs only in a relatively narrow range of graft densities. For the PS grafted particles in PS, this was from approximately 0.01 chains/nm^2 up to 0.1 chains/nm^2, and above this, the phase behavior is expected to be rather dull, in that the particles will remain well dispersed.

Also, the range of graft density in which the PS grafted nanoparticles in a PS homopolymer were truly behaving as amphiphiles depended on the matrix solvent quality, α, first discussed in Section 1.4.

When α was greater than unity, the graft chains were larger than the matrix chains, and the grafts were in good solvent, and therefore were more likely to extend away from the SiO_2 surface. Alternatively, when α was less than one, the poor solvent environment for the graft chains resulted in the grafts retracting toward the SiO_2 surface, away from the brush, and a broadening of the range of graft densities at which immiscibility of particle and matrix polymer was observed.

In the case of PS grafted particles in P2VP, the solvent quality of the matrix for the grafts will be poor, independent of their relative length. Thus the graft chains should tend to segregate themselves toward the surface of the particle, and away from the matrix P2VP. This does not mean the graft length size relative to the matrix length is unimportant. As many previous experimenters have observed, this can be very important. For example, it has been found that the ratio of the R_g of the polymer over the radius of the particle is critical for dispersion, and when this is greater than one, well dispersed particles emerge[78]. In light of this, the question then becomes, how does all of this affect the graft density 'sweet spot'? In the PS graft in a PS matrix system, poor solvent quality pushed the graft density 'sweet spot' upwards. However, in this system, in which the mirror of that behavior is expected, one might reasonably assume the reverse will be true, and this 'sweet spot' will occur at lower graft densities (and indeed this will be seen to mostly be the case).

In addition to well dispersed particles, and large scale phase separation, three other broadly defined dispersion states were observed: small aggregates, micelles, and aggregates of micelles. Representative TEMs of these can be seen in Figure 7.2a, b, and c respectively. Here we achieve a surprising result. In contrast to the PS grafted particles, where sheets and strings and fractal aggregates formed at the 'sweet spot' graft densities, here, micellular structures are observed instead. Thus, a true reversal of the phase diagram is not achieved.

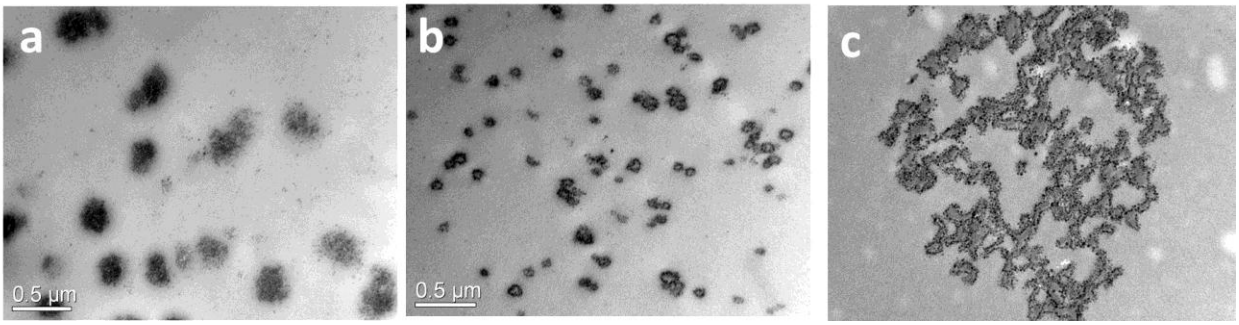

Figure 7.2 *Three of the representative morphologies achieved in a PS grafted particle in P2VP system: small aggregates (a), micelles (b), and aggregates of micelles (c).*

The presence of micelles is not completely unexpected. Voulgaris et al. studied star polymers with equal numbers of PS and P2VP arms in a solution of toluene [142]. The toluene selectively solvated the PS arms and micellular structures formed. The primary question is what determines whether the formation of micelles dominates or, as in the case of PS grafted SiO_2 particles in a PS matrix, whether a wider array of structures such as strings, sheets, and fractal networks of particles are seen. In the case of PS grafted particles in a PS matrix, particle structure formation is driven largely by the tendency of the SiO_2 core to avoid exposure to the matrix. It is reasonable to assume that in the PS grafted particles in a P2VP matrix, a driving force of structure formation will therefore be a tendency to shield the PS grafts from exposure to the matrix P2VP. However, because the SiO_2 core is in the interior of grafted particles, it is relatively easy to shield and a wide range of dispersion states are achievable, whereas because the PS grafts are on the surface, they are not as easily hidden, and the possible dispersion states are apparently limited to micelles.

As a first cut at a morphology diagram for this system, Figure 7.3 is presented. This figure plots the dispersion state for several nanocomposites using the same axes as were used in Figure 1.3. While the well-dispersed composites are at low graft densities and chain lengths, as expected, it is clear from the lack of a consistent trend in the data that this morphology diagram is not a good fit. This is not unexpected, consider that the immiscibility of the P2VP and the grafts is a complicating factor.

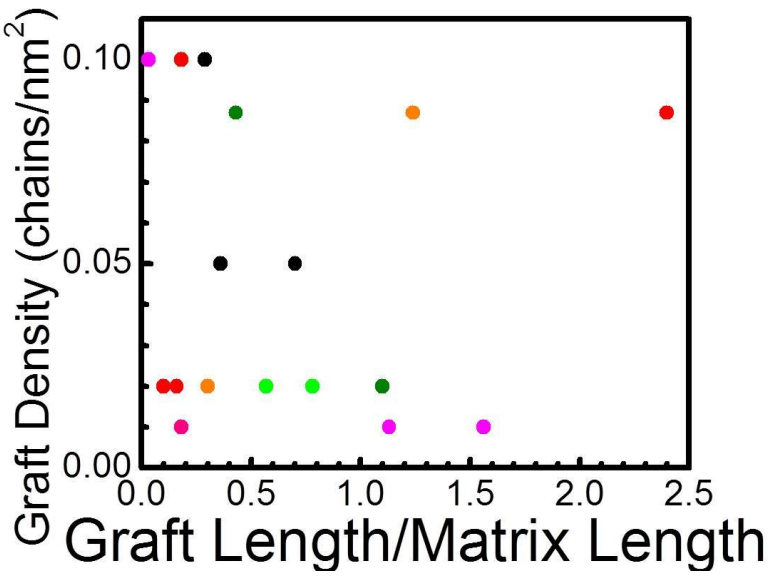

Figure 7.3 *A 'morphology diagram' for PS grafted particles in P2VP using the same axes as Figure 1.3. The color of the data points represents the dispersion state. Magenta represent well-dispersed particles, red represents small aggregates of particles, light green represents micelles, dark green represents large aggregates of micelles, orange represents a mixture of micelles and small aggregates, and black represents phase separation.*

It is apparent that the axis used in the original morphology diagram are not sufficient, and to improve upon these the following new axis are proposed: The radius of gyration of the P2VP and the total weight fraction of PS. The radius of gyration has proven very important in past miscibility studies. And since the total amount of PS is an important factor driving phase separation, it is reasonable to include this as an axis in the phase diagram. In figure 7.4, this morphology diagram is presented with considerably more success than was seen in Figure 7.3. This phase diagram can be separated into three very broadly defined regions, dispersed particles and small aggregates of particles, micelle like structures, and large scale phase separation. However, the trends in these regions do not completely fit with what is expected and more work is needed.

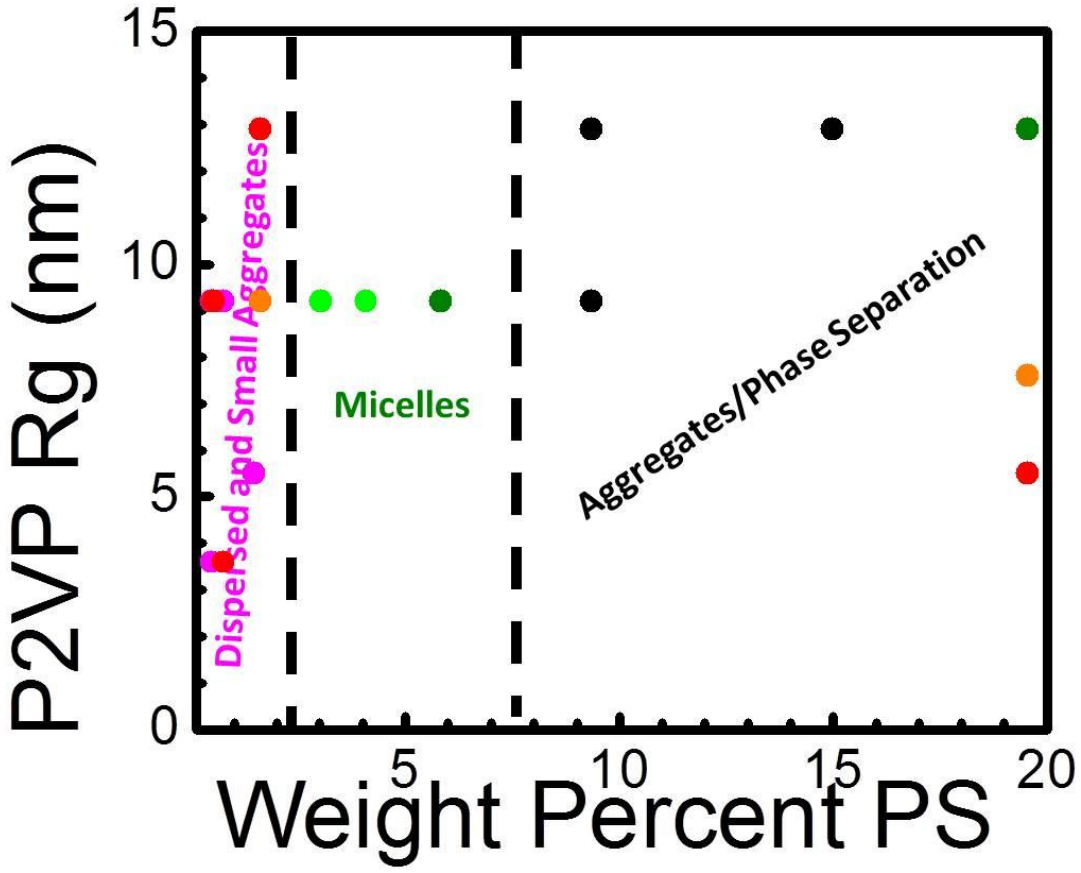

Figure 7.4 *A new 'morphology diagram' for PS grafted particles in P2VP using P2VP radius of gyration and the weight percent of PS to explain the phase behavior. The color of the data points represents the dispersion state. Magenta represent well-dispersed particles, red represents small aggregates of particles, light green represents micelles, dark green represents large aggregates of micelles, orange represents a mixture of micelles and small aggregates, and black represents phase separation.*

7.2 Grafted Particle Mimics Using Block Copolymers

Throughout this text, the means of creating many different nanoparticle dispersion states in a polymer matrix using grafted particles have been explored. The resulting composites have the ability to optimize many nanocomposite properties that fundamentally depend on dispersion, such as mechanical properties, electrical properties, optical properties and gas permeability as discussed in the introduction. However, grafted particle synthesis is a challenging endeavor and is limited by two major problems. The

first is the ability to scale up the process and the second is the cost. The high cost of production of grafted nanoparticles has obvious implications for their use in industrial applications. For example, one of the advantages of nanoparticle addition to polymeric materials is that it can sometimes result in an improved *and* cheaper product, in cases in which the polymer is very expensive. The introduction of grafted particle adds an additional expense that probably can't be justified from a corporate perspective (despite the many unique benefits of the composites). Thus here, the focus is turned to finding a cheaper way to create these amphiphyllic particles that still results in the same properties, namely by replacing SiO_2 particles grafted with PS with SiO_2 particles with PS adsorbed to the surface, by use of block copolymers. Such particles are expected to also self-assemble, based on reports in the literature[143].

Diblock copolymers are selected with one block of PS chains (which replicate the behavior of the PS grafts in the case of grafted polymers) and a second, shorter, copolymer block. The copolymer block must be of a chemistry that it will adsorb to the SiO_2 surface, and in theory, this adsorption could replicate the chemical bond of the graft chains in the di-block copolymer case.

In these experiments, an appropriate chemical identity and copolymer molecular weight are necessary to ensure the block copolymer and bare particle combination truly mimics the grafted particles. PMMA-b-PS was chosen as the appropriate di-block copolymer (recall that cost was a primary motivation for this set of experiments, and this is one of the cheaper di-block copolymers on the market). As was discussed in Chapter 5, poly(methyl methacrylate) (PMMA) has a strongly attractive interaction with the SiO_2 particle surface. Thus the PMMA block will adsorb as an anchor and the PS block will extend outward as a graft. The next important choice is the copolymer molecular weight, which will affect the 'graft density'. Belder et al. found that the anchor molecular weight did not have a strong effect on the thickness of the buoy block (the equivalent of graft density in the grafted system)

[144] . These authors studied P2VP-b-PS, where the PS block was held constant and the P2VP block varied. They also found that at least 24-96 hours were needed for full layer formation. However, this finding was restricted to the case where the buoy polymer was considerably larger than the anchor polymer, and thus the adsorption density was dominated by the inability of the buoy (or grafted) chains to overlap. These findings were also seen in P2VP-b-PS group using neutron reflectivity[145]. In the current study, a 19 kg/mol anchor block of PMMA was chosen and a 135 kg/mol buoy block of PS was chosen. The P.D.I. of the block copolymer is 1.09, and they are in the buoy dominated regime.

The particle size chosen for these experiments was 14nm, as this is the same size as was used in the grafted particle assembly discussed in the introduction. Since the Nissan particles of 14nm size were in methyl ethyl ketone, this was the initial solvent choice. With the particle size, block copolymer, and solvent set, the two primary variables of interest were PS matrix molecular weight and the concentration of block copolymer in solution. Two matrices were studied, one of 290 kg/mol PS and a second of 91.8 kg/mol PS. In Figure 7.5, TEMs for composites solvent cast at three di-block copolymer concentrations in each of the studied matrices are considered (thus there are a total of 6 samples). A primary focus is on the dispersion state. Several different and interesting particle structures are found here, including instances of sheets of particles, small particle aggregates and a more complex structure apparently caused by insertion of particles into a naturally occurring structure from the block copolymer phase diagram. However there is no clear trend in structure formation, either with the concentration of the di-block copolymer grafts or with the matrix PS MW. Furthermore, the homogeneity of the samples was much less than seen in the self-assembling grafted system. That is, as the electron microscope moved through different fields of view in the same composite, the dispersion state often varied dramatically, for instance from strings to particle aggregates. No trend was also seen upon annealing of the samples. Often times, new structures emerged or structures disappeared in the annealed sample that could not have naturally evolved from the unannealed structures (presumably these structures

already existed in the unannealed samples but were not present in the particular microtome slice viewed.

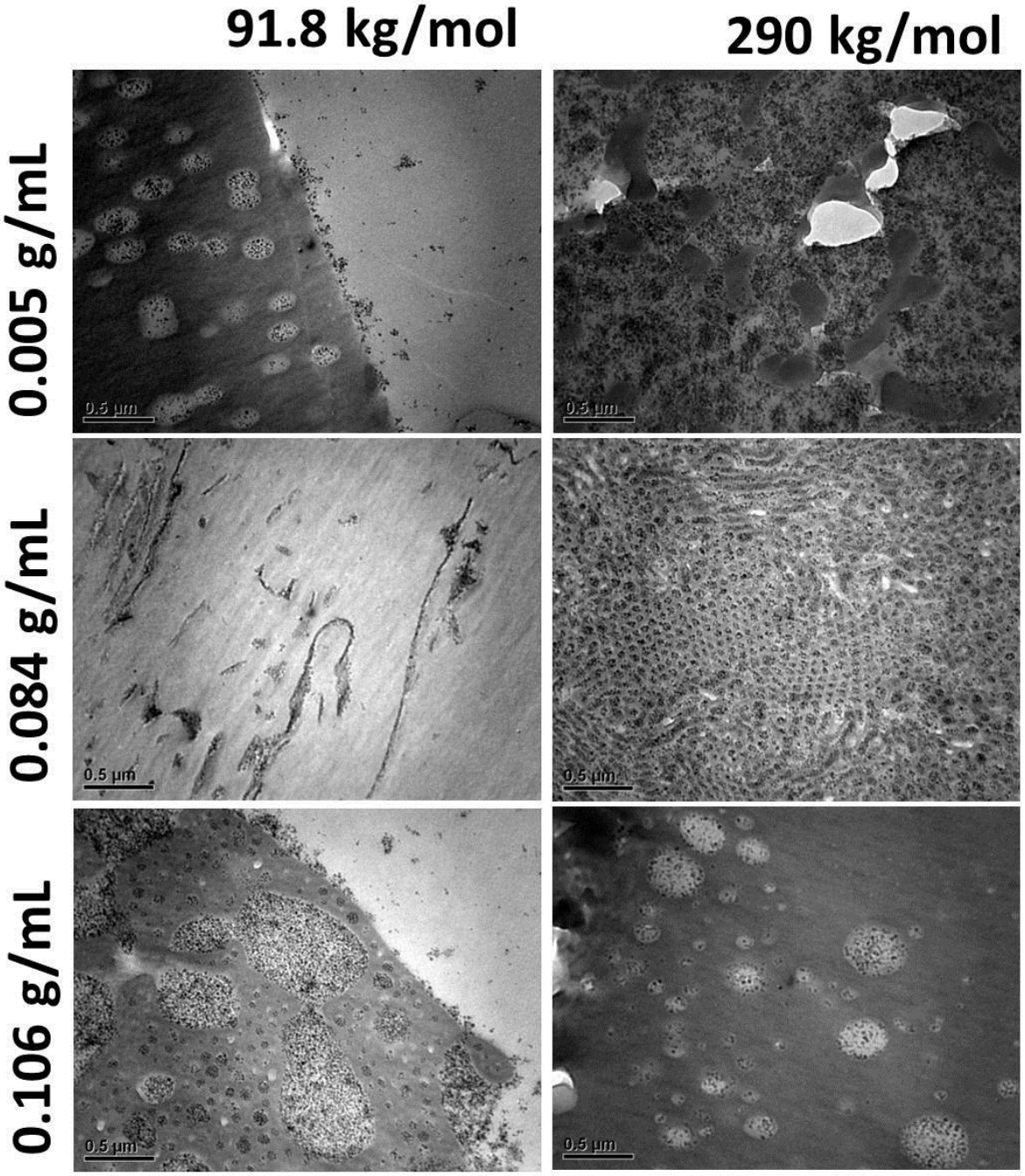

Figure 7.5 *Self assembled structures using different concentrations of PMMA-b-PS and different matrix molecular weights.*

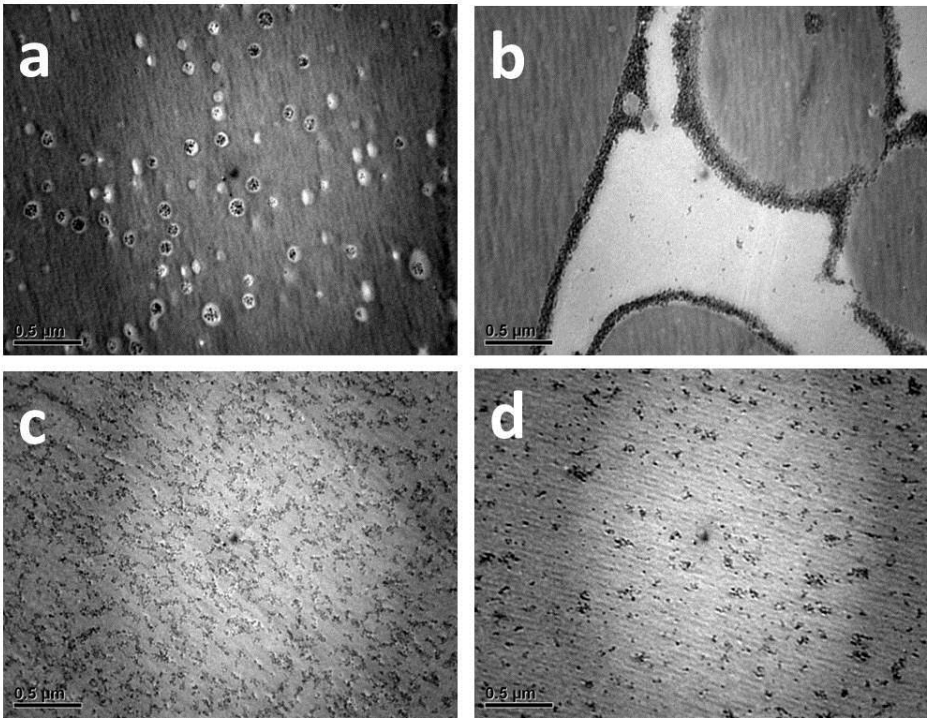

Figure 7.6 *Dispersion states for SiO_2 particles with PMMA-b-PS chains physically adsorbed to the surface. Four different solvents are considered, MEK (a), tetrahydrofuran (b), benzene (c) and toluene (d). The concentration of block copolymer was held constant at 0.0168 g/mL.*

Furthermore, it is not clear what effect the concentration of block copolymer can have as during the solvent casting process, as solvent evaporates, this concentration will necessarily increase. Thus depending on the speed with which adsorption and desorption of the di-block copolymers occurs, there may be plenty of time for these composites to equilibrate to a new more concentrated copolymer state as the solvent evaporates.

A major flaw in the above experiments was poor choice of solvent. Two more appropriate solvent choices were benzene and toluene. The ability of this solvent to solvate both blocks and the bare SiO_2 particles can have a large effect on whether the particles adsorb to the SiO_2 surface. Several different solvents were considered. In Figure 7.6, dispersion states achieved using these two solvents are presented, with somewhat more promising results (the composites prepared in benzene and toluene were largely homogenous). However this study needs considerable further work.

8. Conclusions

In this dissertation, many nanocomposites have been considered, with a focus on the effects of particle dispersion and particle size on the mechanical properties. Dispersion was varied in many different ways. The primary means was through polystyrene (PS) grafted silica (SiO_2) in a PS matrix. Previous work in the Kumar group showed that in such a system, the inherent dislike between the SiO_2 core and the graft chains drove particle self-assembly, producing a wide array of nanoparticle dispersion states. Attempts to mimic this behavior using block copolymers and bare SiO_2 particles proved promising, albeit limited in their initial success. Alternatively, different dispersion states than were possible in the PS matrix system were achieved when the matrix used was P2VP. Specifically, while at the extremes of the graft density it was still possible to get well-dispersed structures and aggregates of particles, intermediate graft densities led to micellular structures.

8.1 Dispersion Effects

When the mechanical properties of the many experimental dispersion states were compared, a clear maximum was found at the intermediate dispersion states, specifically where a fractal like network of particles percolated through the material. While this result is perhaps not completely surprising, more interesting was the fact that this maximum seemed to not only depend on the dispersion state, but also the character of the graft chains. Specifically, the same dispersion states at the highest graft densities studied did not lead to the same degree of reinforcement, because the graft chains were too short. Polymer entanglements play a key role. (Recall that to maintain a dispersion state as graft density is increased, graft length must decrease). Thus the polymer interactions at the surface of the particle were found to be paramount, which has been a persistent theme throughout this text.

This is reinforced by data showing little or no difference in mechanical properties in a bare particle system at two extremes of dispersion. Apparently, bare particles have no ability to interact at the low

loadings, presumably because of the absence of grafts, and thus dispersion state is inconsequential (discussed in more detail in Section 8.4).

8.2 Structure Alignment

The same self-assembled structures achieved in the grafted particle system were aligned using steady shear flow. While flow is very useful for aligning anisotropic structures that have already self-assembled, it is not able to accomplish alignment of isotropic structures such as individual particles, or spherical aggregates of particles. When alignment of structures occurs, it is maximized at the maximum in the stress response in a stress strain curve, and this is confirmed using transmission electron microscopy (TEM) in combination with image analysis and scattering. Large amplitude oscillatory shear (LAOS) was investigated as a means to improve upon alignment observed in steady shear, however this was not possible, suggesting fundamental differences between these polymer nanocomposites and other self-assembling polymer systems, such as di-block copolymers, where LAOS has been found to result in dramatically improved alignment. Despite this, the alignment shown in this text is still impressive, and has relevance in a range of fields. It holds promise for use in materials ranging from batteries to fuel cells.

8.3 Polymer Bound Layer

The particle size was varied in a bare particle system; P2VP and Nissan particles were studied at four different sizes and many different weight percentages. Here the bound polymer layer was considered and it was found that the thickness of this layer had a dependence on particle size, polymer molecular weight, and many other pertinent variables. Specifically, the bound layer thickness increased as the particle size was increased and also increased with increasing polymer molecular weight. This was true both in solution and in the bulk composite material as analyzed through TGA and light scattering. Apparently, the behavior of this surface polymer has a profound effect on the composite mechanical

properties. When the grafted system and the bare particle system are compared, the threshold loading at which a long-lived particle network is observed is much, much lower in the grafted case (discussed in more detail in the proceeding section).

8.4 Grafted Particles vs. Bare Particles

Dispersion was also varied in a bare particle system with P2VP as the homopolymer by using two preparation solvents, methyl ethyl ketone, which allows full adsorption of the P2VP onto the SiO_2 surface, and pyridine, which is a displacer for P2VP on the SiO_2 can potentially prevent the formation of a bound layer and result in particle aggregation. Small amplitude oscillatory shear (SAOS) was performed on these two samples at both 5% and 10% by weight of SiO_2 particles, and the dramatic differences in dispersion state did not lead to significant differences between these two samples (recall in the grafted particle system, dispersion had a profound effect on rheology)

Furthermore, whereas in the grafted particle system, estimates of the onset of a low frequency plateau leading to a particle network were less than 5 weight percent, for the bare particle system, loadings much higher (at least up to 30 weight percent) were used without clear evidence in either the rheology or the XPCS data of solid like behavior. This suggests a fundamentally different mechanism for the reinforcement in these two systems. This has *everything to do with the particle surface chemistry*! In the grafted system, the grafted PS does not have a strong attraction to the surface and thus extends outward, extending the reach of the nanoparticles. In the bare particle system, the P2VP at the surface is tightly adsorbed and depending on particle size extends the reach of the nanoparticles as little as 1 nm. It is also postulated that the ability of these adsorbed chains to entangle is probably greatly reduced.

8.5 Future Work

Many experiments were left unfinished and many questions left unanswered in this text. In the grafted particle system, a theoretical foundation for the strain at which the overshoot occurs needs development. Why do the graft chains push this strain up much higher than it is in a pure polymer melt? Furthermore, why is an overshoot only ever seen at one strain, either the strain characteristic of the pure polymer or the strain characteristic of the grafted particles? In this system, it would also be of interest for a future student to study the yield stress behavior. What is the relationship between the yield stress and the sample morphology, volume fraction, and studied shear rate? Additionally, because of limitations in sample minimal experiments were performed on two regioins from the morphology diagram, the string region and the well dispersed region. However, the well-dispersed region in particular is of interest in the solid state and both of these regions deserve considerably more study to elucidate their rheological properties.

For the project on mimicking of grafted particles, much work still needs to be done. While it is clear from the work presented in Chapter 7 that di-block copolymers, given the correct chemistry of the grafts, readily adsorb to the surface of SiO_2 nanoparticles, this process is as of yet not controlled. More appropriate solvents need to be chosen, and there must be a means of ensuring that the di-block copolymers adsorb evenly over all of the particles.

Experiments at an increased number of particle loadings need to be performed in the bare particle system, especially using XPCS. Additionally, a broader range of particle sizes needs to be considered. The expectation is that some of the most interesting changes in composite behavior upon addition of nanoparticles to polymers will occur at very small nanoparticle sizes. Many of these anticipated changes, such as a significant decrease in the mechanical reinforcement with decreasing particle size, were not observed.

Furthermore, a negligible effect of particle dispersion state was seen in the bare particle system, but it is not clear that this would persist as the particle loading is increased. A key parameter in determining the mechanical reinforcement in the grafted particle system was the presence or the absence of a nanoparticle network. It may be the case therefore that dispersion primarily matters when a certain dispersion state creates a particle network. Perhaps at loadings of only 10% by weight, this is not the case for bare particles, no matter what the dispersion state (recall these particles only have a thin bound layer and thus do not extend their ability to interact with other particles very far). Therefore, rheology on different dispersion states in the bare particle system must be done at higher loadings.

While the work presented here represents significant progress toward a fundamental understanding of mechanical reinforcement upon addition of nanoparticles to polymeric materials, there is still a considerable amount to be learned.

Bibliography

1. Payne, A.R., *Effect of dispersion on the dynamic properties of filler-loaded rubbers.* Journal of Applied Polymer Science, 1965. **9**(6): p. 2273-2284.

2. Payne, A.R., *A note on the conductivity and modulus of carbon black-loaded rubbers.* Journal of Applied Polymer Science, 1965. **9**(3): p. 1073-1082.

3. Heinrich, G. and M. Klüppel, *Recent Advances in the Theory of Filler Networking in Elastomers*

Filled Elastomers Drug Delivery Systems. 2002, Springer Berlin / Heidelberg. p. 1-44.

4. Gusev, A.A., *Micromechanical Mechanism of Reinforcement and Losses in Filled Rubbers.* Macromolecules, 2006. **39**(18): p. 5960-5962.

5. Ounaies, Z., et al., *Electrical properties of single wall carbon nanotube reinforced polyimide composites.* Composites Science and Technology, 2003. **63**(11): p. 1637-1646.

6. Okada, A. and A. Usuki, *Twenty Years of Polymer-Clay Nanocomposites.* Macromolecular Materials and Engineering, 2006. **291**(12): p. 1449-1476.

7. Böhning, M., et al., *Polycarbonate/SiC nanocomposites—influence of nanoparticle dispersion on molecular mobility and gas transport.* Polymers for Advanced Technologies, 2005. **16**(2-3): p. 262-268.

8. Vaia, R.A. and J.F. Maguire, *Polymer Nanocomposites with Prescribed Morphology: Going beyond Nanoparticle-Filled Polymers.* Chemistry of Materials, 2007. **19**(11): p. 2736-2751.

9. Brown, D., et al., *Effect of Filler Particle Size on the Properties of Model Nanocomposites.* Macromolecules, 2008. **41**(4): p. 1499-1511.

10. Akcora, P., et al., *"Gel-like" Mechanical Reinforcement in Polymer Nanocomposite Melts.* Macromolecules, 2009. **43**(2): p. 1003-1010.

11. Chevigny, C., et al., *Polymer-Grafted-Nanoparticles Nanocomposites: Dispersion, Grafted Chain Conformation, and Rheological Behavior.* Macromolecules, 2010. **44**(1): p. 122-133.

12. Dealy, J.M. and K.F. Wissbrun, *Melt Rheology and Its Role in Plastics Processing*. 1999, Dordrecht, The Netherlands: Kluwar Academic Publishers.

13. Rubinstein, M. and R.H. Colby, *Polymer Physics*. 2011, Oxford, United Kingdom: Oxford University Press.

14. Stangler, S. and V. Abetz, *Orientation behavior of AB and ABC block copolymers under large amplitude oscillatory shear flow.* Rheologica Acta, 2003. **42**(6): p. 569-577.

15. Chen, Z.-R., et al., *Pathways to Macroscale Order in Nanostructured Block Copolymers.* Science, 1997. **277**(5330): p. 1248-1253.

16. Amos, R.M., et al., *Fabrication of large-area face-centered-cubic hard-sphere colloidal crystals by shear alignment.* Physical Review E, 2000. **61**(3): p. 2929-2935.

17. Krishnamoorti, R. and K. Yurekli, *Rheology of polymer layered silicate nanocomposites.* Current Opinion in Colloid & Interface Science, 2001. **6**(5–6): p. 464-470.

18. Ren, J. and R. Krishnamoorti, *Nonlinear Viscoelastic Properties of Layered-Silicate-Based Intercalated Nanocomposites.* Macromolecules, 2003. **36**(12): p. 4443-4451.

19. Lele, A., et al., *In situ rheo-x-ray investigation of flow-induced orientation in layered silicate--syndiotactic polypropylene nanocomposite melt.* Journal of Rheology, 2002. **46**(5): p. 1091-1110.

20. Krishnamoorti, R. and E.P. Giannelis, *Strain Hardening in Model Polymer Brushes under Shear.* Langmuir, 2001. **17**(5): p. 1448-1452.

21. Nam, P.H., et al., *Foam processing and cellular structure of polypropylene/clay nanocomposites.* Polymer Engineering & Science, 2002. **42**(9): p. 1907-1918.

22. Snijkers, F. and D. Vlassopoulos, *Cone-partitioned-plate geometry for the ARES rheometer with temperature control.* Journal of Rheology, 2011. **55**(6): p. 1167-1186.

23. Meissner, J., R.W. Garbella, and J. Hostettler, *Measuring Normal Stress Differences in Polymer Melt Shear Flow.* Journal of Rheology, 1989. **33**(6): p. 843-864.

24. Schweizer, T., *Comparing cone-partitioned plate and cone-standard plate shear rheometry of a polystyrene melt.* Journal of Rheology, 2003. **47**(4): p. 1071-1085.

25. Schweizer, T., J. van Meerveld, and H.C. Ottinger, *Nonlinear shear rheology of polystyrene melt with narrow molecular weight distribution---Experiment and theory.* Journal of Rheology, 2004. **48**(6): p. 1345-1363.

26. Shweizer, T., *A Quick Guide to Better Viscosity Measurements of Highly Viscous Fluids.* Applied Rheology, 2003. **14**(4): p. 5.

27. Sen, S., et al., *Chain Conformations and Bound-Layer Correlations in Polymer Nanocomposites.* Physical Review Letters, 2007. **98**(12): p. 128302.

28. Rittigstein, P. and J.M. Torkelson, *Polymer–nanoparticle interfacial interactions in polymer nanocomposites: Confinement effects on glass transition temperature and suppression of physical aging.* Journal of Polymer Science Part B: Polymer Physics, 2006. **44**(20): p. 2935-2943.

29. Spatz, J.P., S. Sheiko, and M. Möller, *Ion-Stabilized Block Copolymer Micelles: Film Formation and Intermicellar Interaction.* Macromolecules, 1996. **29**(9): p. 3220-3226.

30. Beck Tan, N.C., D.G. Peiffer, and R.M. Briber, *Reactive Reinforcement of Polystyrene/Poly(2-vinylpyridine) Interfaces.* Macromolecules, 1996. **29**(14): p. 4969-4975.

31. Fink, J.K., *Poly(vinylpyridine)*, in *Handbook of Engineering and Specialty Thermoplastics*. 2011, John Wiley & Sons, Inc. p. 189-250.

32. Bansal, A., et al., *Quantitative equivalence between polymer nanocomposites and thin polymer films.* Nat Mater, 2005. **4**(9): p. 693-698.

33. Li, C. and B.C. Benicewicz, *Synthesis of Well-Defined Polymer Brushes Grafted onto Silica Nanoparticles via Surface Reversible Addition−Fragmentation Chain Transfer Polymerization.* Macromolecules, 2005. **38**(14): p. 5929-5936.

34. Li, C., et al., *A Versatile Method To Prepare RAFT Agent Anchored Substrates and the Preparation of PMMA Grafted Nanoparticles.* Macromolecules, 2006. **39**(9): p. 3175-3183.

35. Moad, G., et al., *Advances in RAFT polymerization: the synthesis of polymers with defined end-groups.* Polymer, 2005. **46**(19): p. 8458-8468.

36. Baussard, J.-F., et al., *New chain transfer agents for reversible addition-fragmentation chain transfer (RAFT) polymerisation in aqueous solution.* Polymer, 2004. **45**(11): p. 3615-3626.

37. Lowe, A.B. and C.L. McCormick, *Reversible addition–fragmentation chain transfer (RAFT) radical polymerization and the synthesis of water-soluble (co)polymers under homogeneous conditions in organic and aqueous media.* Progress in Polymer Science, 2007. **32**(3): p. 283-351.

38. Whitesides, G.M. and B. Grzybowski, *Self-Assembly at All Scales.* Science, 2002. **295**(5564): p. 2418-2421.

39. Khandpur, A.K., et al., *Polyisoprene-Polystyrene Diblock Copolymer Phase Diagram near the Order-Disorder Transition.* Macromolecules, 1995. **28**(26): p. 8796-8806.

40. Thurn-Albrecht, T., et al., *Ultrahigh-Density Nanowire Arrays Grown in Self-Assembled Diblock Copolymer Templates.* Science, 2000. **290**(5499): p. 2126-2129.

41. Nie, L., et al., *One-Pot Synthesis of Amphiphilic Polymeric Janus Particles and Their Self-Assembly into Supermicelles with a Narrow Size Distribution.* Angewandte Chemie International Edition, 2007. **46**(33): p. 6321-6324.

42. Hartgerink, J.D., E. Beniash, and S.I. Stupp, *Self-Assembly and Mineralization of Peptide-Amphiphile Nanofibers.* Science, 2001. **294**(5547): p. 1684-1688.

43. Akcora, P., et al., *Anisotropic self-assembly of spherical polymer-grafted nanoparticles.* Nat Mater, 2009. **8**(4): p. 354-359.

44. Janes, D.W., et al., *Dispersion Morphology of Poly(methyl acrylate)/Silica Nanocomposites.* Macromolecules, 2011. **44**(12): p. 4920-4927.

45. Nusser, K., et al., *Conformations of Silica−Poly(ethylene−propylene) Nanocomposites.* Macromolecules, 2010. **43**(23): p. 9837-9847.

46. Li, Y. and B.C. Benicewicz, *Functionalization of Silica Nanoparticles via the Combination of Surface-Initiated RAFT Polymerization and Click Reactions.* Macromolecules, 2008. **41**(21): p. 7986-7992.

47. Schadler, L.S., et al., *Designed Interfaces in Polymer Nanocomposites: A Fundamental Viewpoint.* Materials Research Society Bulletin, 2007. **32**: p. 335-340.

48. Glotzer, S.C. and M.J. Solomon, *Anisotropy of building blocks and their assembly into complex structures.* Nat Mater, 2007. **6**(7): p. 557-562.

49. Matsen, M.W. and J.M. Gardiner, *Autophobic dewetting of homopolymer on a brush and entropic attraction between opposing brushes in a homopolymer matrix.* Journal of Chemical Physics, 2001. **115**(6): p. 2794-2804.

50. Gohr, K., et al., *Dynamics of copolymer micelles in an entangled homopolymer matrix.* Macromolecules, 1999. **32**(21): p. 7156-7165.

51. Gohr, K. and W. Schartl, *Dynamics of copolymer micelles in a homopolymer melt: Influence of the matrix molecular weight.* Macromolecules, 2000. **33**(6): p. 2129-2135.

52. Yezek, L., et al., *Influence of hair density and hair length on interparticle interactions of spherical polymer brushes in a homopolymer matrix.* Macromolecules, 2003. **36**(11): p. 4226-4235.

53. Carrot, G., et al., *Polymer grafting from 10-nm individual particles: proving control by neutron scattering.* Soft Matter, 2006. **2**(12): p. 1043-1047.

54. Chevigny, C., et al., *"Wet-to-Dry" Conformational Transition of Polymer Layers Grafted to Nanoparticles in Nanocomposite.* Macromolecules. **43**(11): p. 4833-4837.

55. Bansal, A., et al., *Controlling the thermomechanical properties of polymer nanocomposites by tailoring the polymer–particle interface.* Journal of Polymer Science Part B: Polymer Physics, 2006. **44**(20): p. 2944-2950.

56. Sunday, D., J. Ilavsky, and D.L. Green, *A Phase Diagram for Polymer-Grafted Nanoparticles in Homopolymer Matrices.* Macromolecules, 2012. **45**(9): p. 4007-4011.

57. Long, D. and P. Sotta, *Stress relaxation of large amplitudes and long timescales in soft thermoplastic and filled elastomers.* Rheologica Acta, 2007. **46**(8): p. 1029-1044.

58. Vondráček, P. and M. Schätz, *Bound rubber and "crepe hardening" in silicone rubber.* Journal of Applied Polymer Science, 1977. **21**(12): p. 3211-3222.

59. Tsagaropoulos, G. and A. Eisenberg, *Dynamic Mechanical Study of the Factors Affecting the Two Glass Transition Behavior of Filled Polymers. Similarities and Differences with Random Ionomers.* Macromolecules, 1995. **28**(18): p. 6067-6077.

60. Bogoslovov, R.B., et al., *Effect of Silica Nanoparticles on the Local Segmental Dynamics in Polyvinylacetate.* AIP Conference Proceedings, 2008. **1027**(1): p. 1315-1317.

61. Sakai, V.G. and A. Arbe, *Quasielastic neutron scattering in soft matter.* Current Opinion in Colloid & Interface Science, 2009. **14**(6): p. 381-390.

62. Gagliardi, S., et al., *Restricted dynamics in polymer-filler systems.* Physica B: Condensed Matter, 2001. **301**(1–2): p. 110-114.

63. Aranguren, M.I., et al., *Effect of reinforcing fillers on the rheology of polymer melts.* Journal of Rheology, 1992. **36**(6): p. 1165-1182.

64. Maier, P.J. and D. Goritz, *Molecular Interpretation of the Payne effect.* Kautschuk Gummi Kunststoffe, 1996. **49**(1): p. 4.

65. Zhu, Z., et al., *Investigating Linear and Nonlinear Viscoelastic Behavior Using Model Silica-Particle-Filled Polybutadiene.* Macromolecules, 2005. **38**(21): p. 8816-8824.

66. Zhu, A.-J. and S.S. Sternstein, *Nonlinear viscoelasticity of nanofilled polymers: interfaces, chain statistics and properties recovery kinetics.* Composites Science and Technology, 2003. **63**(8): p. 1113-1126.

67. Leblanc, J.L., *Rubber–filler interactions and rheological properties in filled compounds.* Progress in Polymer Science, 2002. **27**(4): p. 627-687.

68. Jackson, C.L. and G.B. McKenna, *The glass transition of organic liquids confined to small pores.* Journal of Non-Crystalline Solids, 1991. **131–133, Part 1**(0): p. 221-224.

69. Jackson, C.L. and G.B. McKenna, *Vitrification and Crystallization of Organic Liquids Confined to Nanoscale Pores.* Chemistry of Materials, 1996. **8**(8): p. 2128-2137.

70. Keddie, J.L., R.A.L. Jones, and R.A. Cory, *Interface and surface effects on the glass-transition temperature in thin polymer films.* Faraday Discussions, 1994. **98**: p. 219-230.

71. Keddie, J.L., R.A.L. Jones, and R.A. Cory, *Size-Dependent Depression of the Glass Transition Temperature in Polymer Films.* EPL (Europhysics Letters), 1994. **27**(1): p. 59.

72. Tate, R.S., et al., *Extraordinary elevation of the glass transition temperature of thin polymer films grafted to silicon oxide substrates.* The Journal of Chemical Physics, 2001. **115**(21): p. 9982-9990.

73. Torres, J.A., P.F. Nealey, and J.J. de Pablo, *Molecular Simulation of Ultrathin Polymeric Films near the Glass Transition.* Physical Review Letters, 2000. **85**(15): p. 3221-3224.

74. Harton, S.E., et al., *Immobilized Polymer Layers on Spherical Nanoparticles.* Macromolecules, 2010. **43**(7): p. 3415-3421.

75. Sargsyan, A., et al., *The amount of immobilized polymer in PMMA SiO2 nanocomposites determined from calorimetric data.* European Polymer Journal, 2007. **43**(8): p. 3113-3127.

76. Lupaşcu, V., S.J. Picken, and M. Wübbenhorst, *Cooperative and non-cooperative dynamics in ultra-thin films of polystyrene studied by dielectric spectroscopy and capacitive dilatometry.* Journal of Non-Crystalline Solids, 2006. **352**(52–54): p. 5594-5600.

77. Erber, M., et al., *Glassy Dynamics and Glass Transition in Thin Polymer Layers of PMMA Deposited on Different Substrates.* Macromolecules, 2010. **43**(18): p. 7729-7733.

78. Mackay, M.E., et al., *General Strategies for Nanoparticle Dispersion.* Science, 2006. **311**(5768): p. 1740-1743.

79. Bogoslovov, R.B., et al., *Effect of Silica Nanoparticles on the Local Segmental Dynamics in Poly(vinyl acetate).* Macromolecules, 2008. **41**(4): p. 1289-1296.

80. Moll, J. and S.K. Kumar, *Glass Transitions in Highly Attractive Highly Filled Polymer Nanocomposites.* Macromolecules, 2012. **45**(2): p. 1131-1135.

81. Cohen-Addad, J.P. and R. Ebengou, *Silica—siloxane mixtures. Investigations into adsorption properties of end-methylated and end-hydroxylated chains.* Polymer, 1992. **33**(2): p. 379-383.

82. Fragiadakis, D., L. Bokobza, and P. Pissis, *Dynamics near the filler surface in natural rubber-silica nanocomposites.* Polymer, 2011. **52**(14): p. 3175-3182.

83. Fragiadakis, D., P. Pissis, and L. Bokobza, *Modified chain dynamics in poly(dimethylsiloxane)/silica nanocomposites.* Journal of Non-Crystalline Solids, 2006. **352**(42–49): p. 4969-4972.

84. Ciprari, D., K. Jacob, and R. Tannenbaum, *Characterization of Polymer Nanocomposite Interphase and Its Impact on Mechanical Properties.* Macromolecules, 2006. **39**(19): p. 6565-6573.

85. Zhu, J., et al., *Improving the Dispersion and Integration of Single-Walled Carbon Nanotubes in Epoxy Composites through Functionalization.* Nano Letters, 2003. **3**(8): p. 1107-1113.

86. Yang, Y., J. Lan, and X. Li, *Study on bulk aluminum matrix nano-composite fabricated by ultrasonic dispersion of nano-sized SiC particles in molten aluminum alloy.* Materials Science and Engineering: A, 2004. **380**(1–2): p. 378-383.

87. Staverman, A., *Properties of phantom networks and real networks*

Polymer Networks, K. Dušek, Editor. 1982, Springer Berlin / Heidelberg. p. 73-101.

88. Jouault, N., et al., *Well-Dispersed Fractal Aggregates as Filler in Polymer–Silica Nanocomposites: Long-Range Effects in Rheology.* Macromolecules, 2009. **42**(6): p. 2031-2040.

89. Sternstein, S.S. and A.-J. Zhu, *Reinforcement Mechanism of Nanofilled Polymer Melts As Elucidated by Nonlinear Viscoelastic Behavior.* Macromolecules, 2002. **35**(19): p. 7262-7273.

90. Sternstein, S.S., et al., *Reinforcement and nonlinear viscoelasticity of polymer melts containing mixtures of nanofillers.* Rubber Chemistry and Technology, 2005. **78**(2): p. 13.

91. Salaniwal, S., S.K. Kumar, and J.F. Douglas, *Amorphous Solidification in Polymer-Platelet Nanocomposites.* Physical Review Letters, 2002. **89**(25): p. 258301.

92. Rosa, M.E. and H.H. Winter, *The effect of entanglements on the rheological behavior of polybutadiene critical gels.* Rheologica Acta, 1994. **33**(3): p. 220-237.

93. Solomon, M.J., et al., *Rheology of Polypropylene/Clay Hybrid Materials.* Macromolecules, 2001. **34**(6): p. 1864-1872.

94. Chatterjee, T. and R. Krishnamoorti, *Dynamic consequences of the fractal network of nanotube-poly(ethylene oxide) nanocomposites.* Physical Review E, 2007. **75**(5): p. 050403.

95. Goel, V., et al., *Viscoelastic properties of silica-grafted poly(styrene–acrylonitrile) nanocomposites.* Journal of Polymer Science Part B: Polymer Physics, 2006. **44**(14): p. 2014-2023.

96. Treece, M.A. and J.P. Oberhauser, *Soft Glassy Dynamics in Polypropylene−Clay Nanocomposites.* Macromolecules, 2007. **40**(3): p. 571-582.

97. Ilavsky, J., et al., *Ultra-small-angle X-ray scattering at the Advanced Photon Source.* Journal of Applied Crystallography, 2009. **42**(3): p. 469-479.

98. Beaucage, G., *Small-Angle Scattering from Polymeric Mass Fractals of Arbitrary Mass-Fractal Dimension.* Journal of Applied Crystallography, 1996. **29**(2): p. 134-146.

99. Michele, J., R. Pätzold, and R. Donis, *Alignment and aggregation effects in suspensions of spheres in non-Newtonian media.* Rheologica Acta, 1977. **16**(3): p. 317-321.

100. Pasquino, R., et al., *The effect of particle size and migration on the formation of flow-induced structures in viscoelastic suspensions.* Rheologica Acta, 2010. **49**(10): p. 993-1001.

101. Scirocco, R., J. Vermant, and J. Mewis, *Effect of the viscoelasticity of the suspending fluid on structure formation in suspensions.* Journal of Non-Newtonian Fluid Mechanics, 2004. **117**(2-3): p. 183-192.

102. Won, D. and C. Kim, *Alignment and aggregation of spherical particles in viscoelastic fluid under shear flow.* Journal of Non-Newtonian Fluid Mechanics, 2004. **117**(2-3): p. 141-146.

103. Mobuchon, C., P.J. Carreau, and M.-C. Heuzey, *Anisotropy of nonaqueous layered silicate suspensions subjected to shear flow* Journal of Rheology, 2009. **53**(3): p. 22.

104. Kremer, J.R., D.N. Mastronarde, and J.R. McIntosh, *Computer Visualization of Three-Dimensional Image Data Using IMOD.* Journal of Structural Biology, 1996. **116**(1): p. 71-76.

105. Leal, L.G., *The motion of small particles in non-Newtonian fluids.* Journal of Non-Newtonian Fluid Mechanics, 1979. **5**(0): p. 33-78.

106. Hobbie, E.K., et al., *Orientation of carbon nanotubes in a sheared polymer melt.* Physics of Fluids, 2003. **15**(5): p. 1196-1202.

107. Mohraz, A. and M.J. Solomon, *Orientation and rupture of fractal colloidal gels during start-up of steady shear flow* Journal of Rheology, 2005. **49**(3): p. 25.

108. Masschaele, K. and J. Vermant, *Direct visualization of yielding in model two-dimensional colloidal gels subjected to shear flow* Journal of Rheology, 2009. **53**(6): p. 24.

109. Rajaram, B. and A. Mohraz, *Microstructural response of dilute colloidal gels to nonlinear shear deformation.* Soft Matter, 2010. **6**(10): p. 2246-2259.

110. Rajaram, B. and A. Mohraz, *Dynamics of shear-induced yielding and flow in dilute colloidal gels.* Physical Review E, 2011. **84**(1): p. 011405.

111. *Soft Matter, Volume 2: Complex Colloidal Suspensions*, ed. G. Gompper and M. Schick. Vol. 2. 2007, Weinheim, Germany: Wiley-VCH Verlag GmbH & Co. KGaA.

112. Gunes, D.Z., et al., *Flow-induced orientation of non-spherical particles: Effect of aspect ratio and medium rheology.* Journal of Non-Newtonian Fluid Mechanics, 2008. **155**(1–2): p. 39-50.

113. Pasquino, R., et al., *Directed Self-Assembly of Spheres into a Two-Dimensional Colloidal Crystal by Viscoelastic Stresses.* Langmuir, 2010. **26**(5): p. 3016-3019.

114. Vermant, J., *Large-scale structures in sheared colloidal dispersions.* Current Opinion in Colloid & Interface Science, 2001. **6**(5–6): p. 489-495.

115. Kulkarni, S.D. and J.F. Morris, *Ordering transition and structural evolution under shear in Brownian suspensions.* Journal of Rheology, 2009. **53**(2): p. 417-439.

116. Moll, J.F., et al., *Mechanical Reinforcement in Polymer Melts Filled with Polymer Grafted Nanoparticles.* Macromolecules, 2011. **44**(18): p. 7473-7477.

117. Okamoto, M., et al., *A House of Cards Structure in Polypropylene/Clay Nanocomposites under Elongational Flow.* Nano Letters, 2001. **1**(6): p. 295-298.

118. Le Meins, J.-F., P. Moldenaers, and J. Mewis, *Suspensions of monodisperse spheres in polymer melts: particle size effects in extensional flow.* Rheologica Acta, 2003. **42**(1): p. 184-190.

119. Haraguchi, K., M. Ebato, and T. Takehisa, *Polymer–Clay Nanocomposites Exhibiting Abnormal Necking Phenomena Accompanied by Extremely Large Reversible Elongations and Excellent Transparency.* Advanced Materials, 2006. **18**(17): p. 2250-2254.

120. O'Connor, K. and T. McLeish, *Entangled dynamics of healing end-grafted chains at a solid/polymer interface.* Faraday Discussions, 1994. **98**: p. 67-78.

121. Brittain, W.J. and S. Minko, *A structural definition of polymer brushes.* Journal of Polymer Science Part A: Polymer Chemistry, 2007. **45**(16): p. 3505-3512.

122. Ji, H. and P.G. De Gennes, *Adhesion via connector molecules: the many-stitch problem.* Macromolecules, 1993. **26**(3): p. 520-525.

123. Adjari, A., et al., *Slippage of an entangled polymer melt on a grafted surface.* Physica A: Statistical Mechanics and its Applications, 1994. **204**(1–4): p. 17-39.

124. Likos, C.C. and H.M. Harreis, *Star polymers: From conformations to interactions to phase diagrams.* Condensed Matter Physics, 2002. **5**(29): p. 28.

125. Doi, M. and S.F. Edwards, *The Theory of Polymer Dynamics*. 1986, New York: Oxford University Press.

126. Miros, A., et al., *Linear rheology of multiarm star polymers diluted with short linear chains.* Journal of Rheology, 2003. **47**(1): p. 163-176.

127. Ferry, J., *Viscoelastic Properties of Polymers*. 1980, New York: John Wiley and Sons.

128. Wang, S.-Q., et al., *New theoretical considerations in polymer rheology: Elastic breakdown of chain entanglement network.* The Journal of Chemical Physics, 2007. **127**(6): p. 064903-14.

129. Jones, R.L., et al., *Phase Behavior of Ultrathin Polymer Mixtures.* Macromolecules, 2004. **37**(18): p. 6676-6679.

130. Indrakanti, A., R.L. Jones, and S.K. Kumar, *Do "Nonequilibrium" Effects Control Strong Surface Segregation from Polymer Blends?* Macromolecules, 2003. **37**(1): p. 9-12.

131. Sasaki, T., et al., *Glass transition of small polystyrene spheres in aqueous suspensions.* The Journal of Chemical Physics, 2003. **119**(16): p. 8730-8735.

132. Coleman, M.M., J.F. Graf, and P.C. Painter, *Specific Interactions and the Miscibility of Polymer Blends*. 1991, Lancaster, PA: Technomic.

133. Tannenbaum, R., et al., *FTIR Characterization of the Reactive Interface of Cobalt Oxide Nanoparticles Embedded in Polymeric Matrices.* The Journal of Physical Chemistry B, 2006. **110**(5): p. 2227-2232.

134. Cohen-Addad, J.P., *Silica-siloxane mixtures. Structure of the adsorbed layer: chain length dependence.* Polymer, 1989. **30**(10): p. 1820-1823.

135. Omari, R.A., et al., *Diffusion of Nanoparticles in Semidilute and Entangled Polymer Solutions.* The Journal of Physical Chemistry B, 2009. **113**(25): p. 8449-8452.

136. Guo, H., et al., *Nanoparticle Motion within Glassy Polymer Melts.* Physical Review Letters, 2009. **102**(7): p. 075702.

137. Ndong, R.S. and W.B. Russel, *Rheology of surface-modified titania nanoparticles dispersed in PDMS melts: The significance of the power law.* Journal of Rheology, 2012. **56**(1): p. 27-43.

138. Asakura, S. and F. Oosawa, *On Interaction between Two Bodies Immersed in a Solution of Macromolecules.* The Journal of Chemical Physics, 1954. **22**(7): p. 1255-1256.

139. Lin, Y.-L., et al., *Self-Assembled Superstructures of Polymer-Grafted Nanoparticles: Effects of Particle Shape and Matrix Polymer.* The Journal of Physical Chemistry C, 2011. **115**(13): p. 5566-5577.

140. Wu, T., et al., *Fabrication of Hybrid Silica Nanoparticles Densely Grafted with Thermoresponsive Poly(N-isopropylacrylamide) Brushes of Controlled Thickness via Surface-Initiated Atom Transfer Radical Polymerization.* Chemistry of Materials, 2007. **20**(1): p. 101-109.

141. Dukes, D., et al., *Conformational Transitions of Spherical Polymer Brushes: Synthesis, Characterization, and Theory.* Macromolecules, 2010. **43**(3): p. 1564-1570.

142. Voulgaris, D., et al., *Polystyrene/poly(2-vinyl pyridine) heteroarm star copolymer micelles in toluene: morphology and thermodynamics.* Polymer, 1998. **39**(25): p. 6429-6439.

143. Fukao, M., et al., *One-Dimensional Assembly of Silica Nanospheres Mediated by Block Copolymer in Liquid Phase.* Journal of the American Chemical Society, 2009. **131**(45): p. 16344-16345.

144. Belder, G.F., G. ten Brinke, and G. Hadziioannou, *Influence of Anchor Block Size on the Thickness of Adsorbed Block Copolymer Layers.* Langmuir, 1997. **13**(15): p. 4102-4105.

145. Field, J.B., et al., *Neutron reflectivity study of end-adsorbed diblock copolymers: cross-over from mushrooms to brushes.* Journal de Physique II, 1992. **2**(12): p. 15.